Forschungszentrum Karlsruhe
in der Helmholtz-Gemeinschaft

Wissenschaftliche Berichte
FZKA 7353

Application of the SVECHA/QUENCH Code to the Simulation of the Bundle Tests QUENCH-06 and QUENCH-12

A.V. Palagin, J. Stuckert

Institut für Materialforschung
Programm Nukleare Sicherheitsforschung

Dezember 2007

Forschungszentrum Karlsruhe

in der Helmholtz-Gemeinschaft

Wissenschaftliche Berichte

FZKA 7353

Application of the SVECHA/QUENCH Code to the Simulation of the Bundle Tests QUENCH-06 and QUENCH-12

A.V. Palagin*, J. Stuckert

Institut für Materialforschung

Programm Nukleare Sicherheitsforschung

*Joint Research Centre - Institute for Transuranium Elements

Forschungszentrum Karlsruhe GmbH, Karlsruhe

2007

Forschungszentrum Karlsruhe GmbH
Postfach 3640, 76021 Karlsruhe

Mitglied der Hermann von Helmholtz-Gemeinschaft
Deutscher Forschungszentren (HGF)

ISSN 0947-8620

urn:nbn:de:0005-073539

Zusammenfassung

Anwendung des SVECHA/QUENCH-Rechenprogramms für die Modellierung der Bündelversuche QUENCH-06 und QUENCH-12

Für die Modellierung der Bündelversuche QUENCH-06 und QUENCH-12 wurde das Rechenprogramm SVECHA/QUENCH angewendet. Der Versuch QUENCH-06 (Basis für das Internationale Standardproblem ISP-45 der OECD) gilt als Referenzversuch für andere Bündeltests mit unterschiedlichen Konstruktionsmaterialen und Geometrien, wie z. B. QUENCH-12. So wurde der Versuch QUENCH-12 mit dem QUENCH-06-Szenarium durchgeführt, das Testbündel hatte aber die VVER-Geometrie und bestand aus Materialien, die für russische VVER-Reaktoren typisch sind (Hüllrohrlegierung Zr1%Nb, hexogonale Anordnung der Brennstäbe). Das Hauptziel der vorliegenden Arbeit ist der Vergleich der Versuchsergebnisse mit den rechnerischen SVECHA-Ergebnissen für die Versuche QUENCH-06 und QUENCH-12. Die Simulation wurde auf der Basis des sog. Effektiv-Kanal-Modells durchgeführt. Dieses Modell wurde bereits für die Modellierung der früheren QUENCH-Versuche verwendet. Die gemessenen Temperaturen waren geglättet und als Randbedingungen für den Zentralstab verwendet worden. Die Rechnungen geben den Temperatur-Zeit-Verlauf des Zentralstabs bei unterschiedlichen Bündelhöhen während der jeweiligen gesamten Versuchsdauer inklusive Abschreckphase für beide Versuche angemessen wieder. Die berechnete axiale Oxidschichtverteilung entspricht ganz gut den experimentellen Daten für den Versuch QUENCH-06. Für den Fall des Versuches QUENCH-12 waren die gemessenen Oxidschichtdicken deutlich höher wegen der Abplatzungen der Oxidschicht während des Versuches (sog. Breakaway-Effekt). Die berechnete Produktionsrate des Wasserstoffes während der Voroxidation und in den Übergangsphasen stimmt mit den gemessenen Werten für beide Versuche überein. Am Ende der transienten Aufheizphase und beim Abschrecken wird die gerechnete Produktionsrate des Wasserstoffes allerdings unterschätzt.

Abstract

SVECHA/QUENCH code was applied to the simulation of the bundle tests QUENCH-06 and QUENCH-12. Test QUENCH-06 (OECD International Standard Problem, ISP-45) is considered as a reference test for the other QUENCH bundle tests with different materials or geometry. So, the QUENCH-12 test was performed with scenario similar to QUENCH-6, but different materials and bundle geometry (VVER Zr1%Nb cladding, hexagonal lattice). The main aim of the present work is to compare the results of the QUENCH-06 and QUENCH-12 tests with those obtained by the S/Q code calculations. The simulation was performed within the framework of the 'effective channel approach', which has been developed and applied to a number of QUENCH bundle tests performed earlier. The experimentally measured temperatures of the heated rods were processed, smoothed and then used as boundary conditions for the central rod. The calculations of both tests adequately reproduce the temperature evolution of the central rod at different elevations for the whole test duration including the quenching phase. The calculated axial oxide profile agrees quite well with the experimental data in the case of QUENCH-06. In the case of the QUENCH-12 test the experimentally measured oxide thickness was significantly higher than the calculated one due to breakaway effect. The calculated hydrogen production rate as a function of time is well reproduced in comparison with the experimentally measured one during the preoxidation and transient phase of both tests. At the end of transient and quenching phases, however, calculations underestimate hydrogen production rate.

Contents

List of Tables

List of Figures

1 Introduction

In the present work the bundle tests QUENCH-06 [1] and QUENCH-12 [2] were simulated by the SVECHA/QUENCH (S/Q) code [3-5]. Test QUENCH-06 is used as an OECD International Standard Problem (ISP-45) for blind and open calculations for the assessment of severe accident codes. Therefore, QUENCH-06 is considered as a reference test for the other bundle tests with distinguishing materials or geometry. One of such tests is QUENCH-12, which was performed with scenario similar to QUENCH-6, but different materials and bundle geometry (VVER Zr1%Nb cladding, hexagonal lattice). The main aim of the present work is to compare the results of QUENCH-06 and QUENCH-12 tests simulation by the S/Q code.

The S/Q code was elaborated in IBRAE[1] on the basis of the FZK single rod quenching tests in close cooperation with the FZK QUENCH team and was intensively verified against these tests. Within the framework of the S/Q code the main physical phenomena occurring during quenching of fuel rods:

- zirconium oxidation,
- hydrogen absorption by Zircaloy,
- mechanical behaviour of the Zircaloy cladding,
- heat exchange

are considered and their profound mutual influence is accounted for. The description of the S/Q code models is given in [3-5] and in a recent report [6].

The present simulation of the QUENCH bundle tests by the S/Q code was performed using the ‘effective channel’ approach [6-11].

Since the central rod of the bundle is not heated, its temperature evolution in the course of reflooding experiment is completely determined by thermal-hydraulic boundary conditions: temperatures of the surrounding heated rods and shroud and characteristics of the coolant flow (gas phase velocity and composition, boiling regime, flooding rate, etc.). In the case of full-scale simulation of the bundle test the temperatures of the heated rods and shroud are calculated by specifying the electric power time evolution and thus, the boundary conditions for the central rod are determined by the code. At the same time, there exists another possibility to determine the boundary conditions for the central rod: instead of calculation, the temperatures of the heated rods and shroud may be taken from the experiment.

From the viewpoint of the solution of the heat conduction problem inside the central rod both ways are equivalent. Specification of the boundary conditions on the basis of the experimentally measured temperatures even has certain advantages as it describes thermal regime around the central rod very close to that in the experiment.

[1] Nuclear Safety Institute of the Russian Academy of Sciences, Moscow, Russia

Within the framework of the S/Q code the thermal boundary conditions for the central rod may be predetermined by specifying the temperatures of the “effective channel” inner wall on the basis of experimentally measured temperatures. The inner surface of the effective channel represents the surfaces of the heated rods surrounding the central rod.

The heat exchange between the central rod and the effective channel is affected via radiation and heat transfer through the water-gas media filling the channel. The thermal-hydraulic characteristics of the effective channel (cross-section, hydraulic diameter) are determined on the basis of geometrical parameters of the bundle (total cross-section, number of rods and their diameters).

The correct reproduction of the rod temperature evolution in its turn allows a detailed description of cladding mechanical deformation, oxidation and hydrogen absorption processes during reflooding, which were treated by the S/Q in the most advanced mechanistic approach. In the present work all the stages of the QUENCH-6 and QUENCH-12 tests [1, 2] (heatup, preoxidation, transient, water quenching) were properly analysed by the S/Q code. A number of important parameters (rod temperature variation, oxide layer thickness, hydrogen production rate) were calculated and compared with the experimentally measured ones.

Within the framework of the effective channel approach the experimentally measured temperatures at all the elevations (TFS and TSH thermocouples data) were analyzed and smoothed.

The calculated ‘averaged temperature field’ describing temperature evolution around central rod was used in the S/Q code input files for the simulation of the quench bundle tests QUENCH-6 and QUENCH-12 tests. The calculated oxide thickness axial profile was compared with the experimentally measured one at the time moments corresponding to the withdrawn of the corner rods and at the end of the test. The calculated hydrogen production rate was compared with the experimental data. The results of the calculations were compared with each other.

2 QUENCH-06 test simulation

2.1 Processing of the QUENCH-06 bundle test temperature data

During the QUENCH-06 test [1] the temperature was continuously measured at different locations of the bundle. 33 thermocouples were attached to the cladding of the heated rods at 17 different elevations between -250 mm and 1350 mm; 3 thermocouples were attached to the cladding of the central rod at 350, 550 and 950 mm elevations; 3 thermocouples were inserted in the centres of three corner rods at 750, 850 and 950 mm elevations; 2 thermocouples were located between cladding and pellets inside central rod at 350 and 550 mm; 3 thermocouples were located in the centre of the central rod at 350, 550 and 950 mm. The TCs data were processed by the FZK experimental team, incorrect data were deleted and now these data are available in the electronic format. Tables 1 and 2 present the TCs designations, corresponding rod numbers and elevations.

	Channel	TC	Elevation
1	KAN: 04	TFS 2/17 F	1350 mm
2	KAN: 49	TFS 5/17	1350 mm
3	KAN: 37	TFS 3/16	1250 mm
4	KAN: 48	TFS 5/16	1250 mm
5	KAN: 03	TFS 2/15	1150 mm
6	KAN: 47	TFS 5/15	1150 mm
7	KAN: 09	TFS 3/14	1050 mm
8	KAN: 02	TFS 2/13	950 mm
9	KAN: 08	TFS 3/13	950 mm
10	KAN: 11	TFS 4/13	950 mm
11	KAN: 15	TFS 5/13	950 mm
12	KAN: 34	TFS 2/12	850 mm
13	KAN: 50	TFS 3/12	850 mm
14	KAN: 51	TFS 5/12	850 mm
15	KAN: 01	TFS 2/11	750 mm
16	KAN: 10	TFS 4/11	750 mm
17	KAN: 13	TFS 5/11	750 mm
18	KAN: 06	TFS 3/10	650 mm
19	KAN: 39	TFS 2/9	550 mm
20	KAN: 38	TFS 5/9	550 mm
21	KAN: 43	TFS 3/8	450 mm
22	KAN: 42	TFS 5/8	450 mm
23	KAN: 23	TFS 2/7	350 mm
24	KAN: 82	TFS 5/7	350 mm
25	KAN: 76	TFS 2/6	250 mm
26	KAN: 81	TFS 5/6	250 mm
27	KAN: 22	TFS 2/5	150 mm
28	KAN: 80	TFS 5/5	150 mm
29	KAN: 78	TFS 5/4/0	50 mm
30	KAN: 79	TFS 5/4/180	50 mm
31	KAN: 74	TFS 2/3	-50 mm
32	KAN: 73	TFS 2/2	-150 mm
33	KAN: 72	TFS 2/1	-250 mm

Table 1. Locations of the TCs used for the Heated Fuel Rod Simulators temperature measurement in the QUENCH-06 bundle test.

	Channel	TC	Elevation
34	KAN: 32	TIT A/13	950 mm
35	KAN: 41	TCR 13	950 mm
36	KAN: 33	TCRC 13	950 mm
37	KAN: 40	TIT D/12	850 mm
38	KAN: 46	TIT C/9	550 mm
39	KAN: 103	TCR 9	550 mm
40	KAN: 58	TCRC 9	550 mm
41	KAN: 77	TCRI 9	550 mm
42	KAN: 95	TCR 7	350 mm
43	KAN: 116	TCRC 7	350 mm
44	KAN: 75	TCRI 7	350 mm
45	KAN: 20	TSH 11/0	750 mm
46	KAN: 54	TSH 11/180	750 mm

Table 2. Locations of the TCs used for the Central, Corner Rods and shroud temperature measurement in the QUENCH-06 bundle test.

The above TCs data were used for the simulation of the effective channel internal surface. The numerical procedure of the rod TCs data recalculation includes smoothening, averaging and interpolation.

It should be noted that because of the temperature regime of the QUENCH-06 test (relatively low temperatures during practically the main part of the test) practically all the thermocouples survived (the only important exclusion is the elevation 950 mm). That is why the determination of the averaged temperature field around the central rod was rather simple in the case of QUENCH-06 test (in contrast to other bundle tests, for example QUENCH-08 [11] or QUENCH-10 [6]).

1. In Fig. 1 the original TC readings of TFS2/17 and TFS5/17 thermocouples as well as the calculated averaged temperature (**TFS_17**) at the elevation 1350 mm are presented. The averaged temperature was calculated as arithmetic mean of the smoothed TFS2/17 and TFS5/17 data sets.

2. In Fig. 2 the original TC readings of TFS3/16 and TFS5/16 thermocouples as well as the calculated averaged temperature (**TFS_16**) at the elevation 1250 mm are presented. The averaged temperature was calculated as arithmetic mean of the smoothed TFS3/16 and TFS5/16 data sets.

3. In Fig. 3 the original TC readings of TFS2/15 and TFS5/15 thermocouples as well as the calculated averaged temperature (**TFS_15**) at the elevation 1150 mm are presented. The averaged temperature was calculated as arithmetic mean of the smoothed TFS2/15 and TFS5/15 data sets.

4. In Fig. 4 the original TC reading of TFS3/14 thermocouple is presented (the only one bundle TC used at the elevation 1050 mm). Its smoothed data was used as the average temperature at this elevation.

5. In Fig. 5 the original TC readings of TFS2/13, TFS3/13, TFS4/13, TFS5/13 bundle thermocouples, corner rod thermocouple TIT A/13, central rod thermocouples TCR 13 and TCRC 13 at the elevation 950 mm are presented. At this elevation only thermocouples TIT A/13 and TCRC 13 protected from direct contact with steam survived till the end of the test. The averaged temperature was calculated as arithmetic mean of the smoothed data sets of these last TCs (Fig. 6).

6. In Fig. 7 the original TC reading of TIT D/12 thermocouple at the elevation 850 mm is presented. Its smoothed data was used as the average temperature at this elevation.

7. In Fig. 8 the original TC readings of **shroud** thermocouples TSH11/0 and TSH11/180 as well as the calculated averaged temperature (**TSH_11**) at the elevation 750 mm are presented. It should be noted here that at this elevation the shroud TCs instead of rod ones were used as the basis for the average temperature because of the fact that the rod TCs TFS2/11, TFS 4/11 and TFS5/11 were qualified by the QUENCH team as being 'questionable'. A special instrumentation of the bundle in the QUENCH-09 test confirmed the supposition that thermocouples which are lead through the hot zone of the bundle may give wrong readings at high temperatures in the hot zone [12]. In the case of the elevation of 750 mm the rod thermocouples really gave wrong readings starting from 6600 s, as it was independently shown by the S/Q code calculations (see below). Up to 6600 s the readings of rod and shroud TCs practically coincide. That is why the averaged temperature at the elevation 750 mm was calculated as arithmetic mean of the smoothed TSH11/0 and TSH11/180 data sets for the whole duration of the test.

8. In Fig. 9 the original TC reading of TFS3/10 thermocouple is presented (the only one bundle TC used at the elevation 650 mm). Its smoothed data was used as the average temperature at this elevation.

9. In Fig. 10 the original TC readings of TFS2/9 and TFS5/9 thermocouples as well as the calculated averaged temperature (**TFS_9**) at the elevation 550 mm are presented. The averaged temperature was calculated as arithmetic mean of the smoothed TFS2/9 and TFS5/9 data sets.

10. In Fig. 11 the original TC readings of TFS3/8 and TFS5/8 thermocouples as well as the calculated averaged temperature (**TFS_8**) at the elevation 450 mm are presented. The averaged temperature was calculated as arithmetic mean of the smoothed TFS3/8 and TFS5/8 data sets.

At the elevations from 350 mm to -250 mm all the TFS thermocouples survived throughout the test. That is why the average temperatures at these elevations were determined as arithmetic mean of the corresponding smoothed TFS curves.

The calculated average temperature curves representing temperature evolution of the bundle at 17 elevations from 1350 mm to -250 mm from the beginning of the test up to the moment of flooding initiation are given in Fig. 12. These curves were used as the boundary conditions for the effective channel walls in the S/Q code simulation of the QUENCH-06 test at the preoxidation and transient phases.

2.2 Effective channel parameters determination

The parameters of the effective channel in the present calculation were determined in the same way as for the previous QUENCH bundle tests simulation [6-11].

The following bundle parameters were used for the channel determination:

Shroud inner radius	R_{shroud} = 40.0 mm;
Rod outside radius	R_{rod} = 5.375 mm;
Corner rod radius	R_{corner} = 3.0 mm;
Number of rods	N_{rod} = 21;
Number of corner rods	N_{corner} = 4.

The total bundle cross-section is given by the expression:

$$A_{tot} = \pi R_{shroud}^2 - N_{rod} \cdot \pi R_{rod}^2 - N_{corner} \cdot \pi R_{corner}^2 . \quad (1)$$

The value of A_{tot} is equal to 30.07 cm^2.

The value of the channel cross-section per one rod is equal to

$$A_{eff} = \frac{A_{tot}}{N_{rod} + N_{corner}} = 1.203 \text{ cm}^2. \quad (2)$$

The effective channel inner radius is connected with the value of A_{eff} by:

$$\pi R_{eff}^2 - \pi R_{rod}^2 = A_{eff} \Rightarrow R_{eff} = \sqrt{\frac{A_{eff}}{\pi} + R_{rod}^2} = 8.197 \text{ mm}. \quad (3)$$

2.3 Test simulation specifications

The calculated average temperature curves representing temperature evolution of the bundle at 17 elevations from 1350 mm to -250 mm up to the moment of reflooding initiation are given in Fig. 12. These curves were used as the boundary conditions for the effective channel walls in the S/Q code simulation during preoxidation and transient phases of the QUENCH-06. The quenching phase of the test was simulated with the assumption of thermal

equilibrium at each elevation, when the rods cooling down takes place due to interaction with the water-steam mixture.

On the basis of the effective channel parameters specified in the Subsection 2.2, the argon and steam mass flows at all the test phases were determined. By definition, inlet gas flow in the effective channel is connected with the total inlet gas flow by:

$$J_{eff} = J_{tot} \frac{A_{eff}}{A_{tot}} . \quad (4)$$

The value of argon and steam total inlet flow rate was specified to be constant and equal to 3.0 g/s.

At 7178 sec. the argon/steam flow was stopped and water flooding began with flow rate of J_{flood} = 42 g/s. The estimated kinematical velocity of water level motion (without accounting for evaporation and two-phase water-steam regions formation) is given by

$$U_{flood} = \frac{J_{flood}}{A_{tot}} = \text{ 1.4 cm/s.} \quad (5)$$

Time step throughout the test values were:

1.0 s up to 6000 s,

0.1 s up to 7400 s (end of the calculation)

The bundle nodalization is characterised by the following values:

Heat conduction module

- The total nodes number in the radial direction: 35
- Pellet nodes number in the radial direction: 21
- External layer (oxide) nodes number: 7
- Total nodes number in the vertical direction: 197

The vertical grid used in the heat conduction module is adaptive one, with maximum density in the region of the maximum temperature axial gradients.

Total number of meshes used by oxidation, mechanical deformation and hydrogen absorption modules was 98. The total central rod length considered was 1975 mm – from the upper point 1500 mm (adjacent to the Al_2O_3 plate thermal shield) to the lower point -475 mm (adjacent to the lower SS plate).

2.4 Calculated temperatures

In this subsection the calculated temperature evolution curves at the different elevations of the central rod are presented.

In Fig. 13 the experimentally measured temperatures at the elevation 1350 mm by TFS2/17 and TFS5/17 thermocouples as well as the calculated temperature evolution of the central rod outer surface at this elevation are presented.

In Fig. 14-15 the analogous comparison between the experimentally measured temperatures at the elevations 1250 and 1150 mm and the calculated temperature evolution of the central rod outer surface at these elevations is given.

In Fig. 16 the experimentally measured temperatures at the elevation 950 mm by outer surface thermocouples TFS2/13, TFS3/13, TFS4/13 and TFS5/13 and by inner thermocouples TIT A/13, TCR13 and TCRC13 as well as the calculated temperature evolution of the central rod outer surface at this elevation are presented.

In Fig. 17-22 the analogous comparison between the experimentally measured temperatures at the elevations 850, 750, 650, 550, 450 and 350 mm and the calculated temperature evolution of the central rod outer surface at these elevations is given.

As one can see, calculated temperature evolution curves at the above elevations generally show good correlation with the experimentally measured ones during preoxidation and transient phases of the test. All the characteristic bends of these test phases were very closely reproduced by the calculations.

In Fig. 23-25 the experimentally measured temperatures of the rod outer surface at the elevations 1350, 1250 and 1150 mm and calculated temperature evolutions at these elevations at the quenching phase of the test (7000-7400 sec.) are presented. Calculated curves show higher cooling rates and do not reproduce the ‘gap’ of the experimental ones: sharp drop of the temperature with following increase. Such temperature behaviour may be partially explained by a local thermocouple effect (interaction with the increased steam flow due to fast water injection at the onset of quenching). The difference in cooling rates is due to complex motion of the water-steam mixture along the coolant channel under confined geometry conditions.

In Fig. 26 the calculated curve of the central rod outer surface temperature evolution at the elevation of 950 mm is compared with the data of the only one survived outer surface thermocouple TFS4/13 (time period 6500 – 7400 sec.). In Fig. 27 two experimental curves of the TIT A/13 and TCRC13 data sets together with the calculated curve of the central rod pellet’s centre are shown. One can see rather satisfactory agreement between the experimental data and calculation results.

In Fig. 28 the calculated curve of the central rod outer surface temperature evolution at the elevation of 850 mm is compared with the data of the outer surface thermocouples TFS3/12 and TFS5/12 (time period 7000 – 7500 sec.). In Fig. 29 the calculated curve of the central

rod pellet's centre at this elevation together with the experimental curve TIT D/12 are presented.

In Fig. 30-37 the similar experimental and calculated temperature evolution curves for the elevations 750, 650, 550, 450, 350 and 250 mm are presented. Sharp drop of the calculated curve in above Figures corresponds to the rewetting of the rod surface by water.

Generally, calculated temperature evolution curves demonstrate rather good correlation with the experimental ones in oxidation, transient and quenching phases of the test.

2.5 Oxide layer thickness

Similarly to the Q-07 [8-9], Q-08 [10-11] and Q-10 [6] tests simulation, in the present work at first the main attention was paid to the comparison of the calculated oxide layer axial profile with the measured one. The experimental information about the oxide layer thickness is available at 6620 s when the corner rod **B** was withdrawn and at the end of the experiment. The obtained simulation results show that at 6620 s the calculated oxide thickness is in good agreement with the experimental data (Fig. 38).

In Fig. 39 the averaged oxide layer thickness profiles of all the rods, corner rods and shroud, measured at the end of the test are compared with the calculated oxide layer thickness profile of the central rod (final status). As one can see, the calculated oxide profile well reproduces the measured one.

As it was mentioned above, the thermocouples located at the elevation 750 mm inside the bundle, on the outer surfaces of the heated rods, were led through the hot zone of the bundle and thus gave wrong readings at high temperatures in the hot zone. That is why the averaged temperature at the elevation 750 mm was calculated as arithmetic mean of the smoothed shroud TSH11/0 and TSH11/180 data sets.

An interesting question arises: what results will give the calculation using rod thermocouples TFS2/11, TFS 4/11 and TFS5/11 data sets as the basis for the average temperature at the considered elevation. Fig. 40 illustrates the difference between two groups of thermocouples: rod and shroud ones in the time period of interest (6000 – 7500 s). As one can see, this difference gradually increased starting from 6600 s reaching more than 250 K just before quenching.

Additional calculation (simulation of the Q-06 test using the TFS2/11, TFS 4/11 and TFS5/11 data sets as the basis for the average temperature at the elevation of 750 mm) gives the results presented in Fig. 41. One can see two-peak oxide axial profile curve with the oxide thickness of more than 400 µm at the elevation of 750 mm instead of 100-130 µm (experimental result). Such big overestimation of the calculated oxide thickness at this elevation confirms the fact that the above rod-based thermocouples really gave wrong readings after 6600 s. On the other hand, difference between two calculations, being well in line with the conclusion of the QUENCH team, about the erroneous of TFS2/11, TFS 4/11 and TFS5/11 data sets additionally validates the adequacy of the S/Q code.

For the illustration of the oxide layer development during the test the axial profiles at 6620 s, 7100 s (beginning of temperature escalation) and at the end of the test are presented in Fig.42.

2.6 Hydrogen release analysis

Due to uniformity of the radial temperature distribution inside the bundle in the QUENCH-06 test one can say that the central rod behaviour generally represents the average behaviour of the 20 heated rods and shroud. Using this consideration one can extrapolate the hydrogen production results calculated for the central rod to the whole bundle [6-11]. The total hydrogen production rate of the whole bundle $\dot{m}_{bundle}$ is connected with calculated central rod production rate $\dot{m}_{rod}$ by the following relation:

$$\dot{m}_{bundle} = A \cdot \dot{m}_{rod}, \quad A = N_{rod} + N_{corner} \frac{R_{corner}}{R_{rod}} + \frac{R_{shroud}}{R_{rod}} = 30.67. \tag{6}$$

Here $N_{rod} =$ 21 is the number of rods (including central rod), $N_{corner} =$ 4 is the number of corner rods, R_{corner}, R_{rod} and R_{shroud} are heated rod, corner rod and shroud radii correspondingly.

In Fig. 43 the hydrogen production rate calculated according to relation (6) on the basis of S/Q code simulation and the experimental data are presented. As one can see, the calculated curve is in good agreement with the experimental one during the preoxidation and temperature escalation phases of the test. Small underestimation of the hydrogen production rate may be explained by the fact that not all the structures exposed to oxidation (spacer grids, thermocouple wires) were accounted for while applying relation (6).

Fig. 44 shows experimentally measured and calculated hydrogen production rate during second part of the temperature escalation phase and quenching phase. Calculated curve is located lower than the experimental one, but generally repeats it form, including the peak at the onset of quenching.

According to the calculation results, the total amount of generated hydrogen is 29.6 g (experimental value is 36 g [1]). Amount of calculated hydrogen released during quenching phase of the test is 4.4 g, while experimental value is 4 g.

2.7 Summary of the QUENCH-06 test simulation

- SVECHA/QUENCH code was applied to the simulation of the QUENCH bundle test QUENCH-06. The simulation was performed within the framework of the 'effective channel approach'.

- The experimentally measured temperatures of the heated rods were processed, smoothed and then used as boundary conditions (average temperature field) for the central rod.

- The simulation of the QUENCH-06 test using averaged temperature field was performed. All the stages of the test (heatup, preoxidation, temperature escalation, water quenching) were considered.

- The calculations adequately reproduce temperature evolution of the central rod at different elevations during the whole test duration with some discrepancies at the quenching phase.

- The calculated oxide axial profile agrees quite well with the experimental data at the time moment 6620 s when the corner rod B was withdrawn from the bundle and at the end of the test.

- Oxide thickness at the elevation 750 mm calculated on the basis of 'questionable TCs' is overestimated; usage of protected shroud TCs data results in correct value of the oxide thickness. This fact confirmed the correctness of the supposition that thermocouples which are lead through the hot zone of the bundle may give wrong readings at high temperatures in the hot zone and additionally validates the adequacy of the S/Q code.

- The details of the experimentally measured time dependence of the hydrogen production rate as well as the total amount of the released hydrogen are well reproduced by the calculations.

3 QUENCH-12 test simulation

3.1 Processing of the QUENCH-12 bundle test temperature data

During the QUENCH-12 test [2] the temperature was continuously measured at different locations of the bundle. 42 thermocouples were attached to the cladding of the rods at 17 different elevations between -250 mm and 1350 mm. The designations are: “TFSH” for the heated rods (total number of heated rods was 18), “TFSU” for the unheated rods including central rod (total number of unheated rods was 13). 13 thermocouples were installed in the centre of the unheated rod including central rod, their designation was “TFC”. The thermocouples that were installed inside the Zr1%Nb instrumentation rods at three corner positions of the bundle were designated “TIT”.

Tables 3 and 4 presents the TCs designations, corresponding rod numbers and elevations.

	Channel	TC	Elevation
1	KAN: 00	TFSH 31/5/17	1350 mm
2	KAN: 02	TFSU 11/3/17	1350 mm
3	KAN: 03	TFSH 30/5/16	1250 mm
4	KAN: 04	TFSU 15/3/16	1250 mm
5	KAN: 06	TFSH 21/5/15	1150 mm
6	KAN: 09	TFSU 9/3/15	1150 mm
7	KAN: 10	TFSH 5/2/15	1150 mm
8	KAN: 11	TFSH 27/5/14	1050 mm
9	KAN: 12	TFSU 19/3/14	1050 mm
10	KAN: 15	TFSU 12/4/14	1050 mm
11	KAN: 18	TFSH 6/2/14	1050 mm
12	KAN: 19	TFSH 29/5/13	950 mm
13	KAN: 20	TFSU 17/3/13	950 mm
14	KAN: 28	TFSU 10/4/13	950 mm
15	KAN: 30	TFSH 2/2/13	950 mm
16	KAN: 31	TFSU 1/1/13	950 mm
17	KAN: 33	TFSH 26/5/12	850 mm
18	KAN: 34	TFSU 18/4/12	850 mm
19	KAN: 37	TFSH 3/2/12	850 mm
20	KAN: 40	TFSH 23/5/11	750 mm
21	KAN: 41	TFSH 7/2/11	750 mm
22	KAN: 47	TFSH 20/5/10	650 mm
23	KAN: 48	TFSU 16/4/10	650 mm

	Channel	TC	Elevation
24	KAN: 22	TFSH 30/5/9	550 mm
25	KAN: 23	TFSH 25/5/9	550 mm
26	KAN: 35	TFSU 17/3/9	550 mm
27	KAN: 36	TFSU 9/3/9	550 mm
28	KAN: 38	TFSH 4/2/9	550 mm
29	KAN: 42	TFSU 1/9	550 mm
30	KAN: 43	TFSU 19/3/8	450 mm
31	KAN: 44	TFSU 12/4/8	450 mm
32	KAN: 45	TFSH 28/5/7	350 mm
33	KAN: 46	TFSH 5/2/7	350 mm
34	KAN: 39	TFSU 1/7	350 mm
35	KAN: 72	TFSU 15/3/6	250 mm
36	KAN: 73	TFSU 11/3/6	250 mm
37	KAN: 74	TFSU 13/3/5	150 mm
38	KAN: 75	TFSH 2/2/5	150 mm
39	KAN: 76	TFSH 30/5/4	50 mm
40	KAN: 77	TFSH 24/5/4	50 mm
41	KAN: 108	TFSH 6/2/2	-150 mm
42	KAN: 119	TFSH 4/2/1	-250 mm

Table 3. Locations of the TCs used for the temperature measurements at the outer surface of heated and unheated rods in the QUENCH-12 bundle test

The TCs data were used for the simulation of the effective channel internal surface. The numerical procedure of the rod TCs data recalculation includes smoothening, averaging and interpolation. Because of the temperature regime of the QUENCH-12 test (even lower temperatures during practically the main part of the test than in the QUENCH-06) practically all the thermocouples survived. That is why the determination of the averaged temperature field around the central rod was rather simple.

1. In Fig. 45 the original TC readings of TFC18/4/17 and TFSU11/3/17 thermocouples as well as the calculated averaged temperature (**TFS_17**) at the elevation 1350 mm are presented. The averaged temperature was calculated as arithmetic mean of the smoothed TFC18/4/17 and TFSU11/3/17 data sets.

2. In Fig. 46 the original TC readings of TFSH30/5/16 and TFC13/3/16 thermocouples as well as the calculated averaged temperature (**TFS_16**) at the elevation 1250 mm are presented. The averaged temperature was calculated as arithmetic mean of the smoothed TFSH30/5/16 and TFC13/3/16 data sets.

	Channel	TC	Elevation
43	KAN: 01	TFC 18/4/17	1350 mm
44	KAN: 05	TFC 13/3/16	1250 mm
45	KAN: 07	TFC 16/4/15	1150 mm
46	KAN: 08	TFC 10/4/15	1150 mm
47	KAN: 14	TFC 15/3/14	1050 mm
48	KAN: 16	TFC 12/4/14	1050 mm
49	KAN: 17	TFC 9/3/14	1050 mm
50	KAN: 21	TFC 17/3/13	950 mm
51	KAN: 26	TFC 14/4/13	950 mm
52	KAN: 27	TFC 11/3/13	950 mm
53	KAN: 29	TFC 8/4/13	950 mm
54	KAN: 32	TFC 1/13	950 mm
55	KAN: 49	TIT A/13	950 mm
56	KAN: 50	TIT C/12	850 mm
57	KAN: 51	TFC 1/12	850 mm
58	KAN: 52	TIT E/11	750 mm

Table 4. Locations of the TCs used for the temperature measurements inside the centre of unheated rods and corner rods in the QUENCH-12 bundle test.

3. In the two previous cases the temperature readings of TCs located at the same elevation were rather close to each other. This fact testifies to the uniform temperature distribution in the radial directions at these elevations. However, difference between TC readings at the elevation 1150, 1050 and 950 mm during preoxidation and transient phases of the test was more than 150 K (see Figs. 47, 49, 51). Such high temperature non-uniformity (non-typical for the QUENCH-06 test) was due to the fact that in QUENCH-12 test only 18 heated rods were used from the total number of 31 because of technical reasons (in QUNCH-06 test 20 rods from total number of 21 were heated). Another probable reason was partially inadequate data of the TFSU and TFSH type thermocouples located at the outer surface of the rods and exposed to direct contact with steam and oxidation. Taking into account the above considerations it was decided to use mainly the TFC and TIT type thermocouples as the basis for the average temperature since they were ere installed in the centre of the unheated and corner rods and thus were protected from direct contact with steam and oxidation. At the elevation 1150 mm the TFC16/4/15 and TFC10/4/15 thermocouples were used as such basis (Fig. 48).

4. In Fig. 50 the original TC readings of TFC9/3/14 and TFC15/3/14 thermocouples as well as the calculated averaged temperature (**TFS_14**) at the elevation 1050 mm are

presented. The averaged temperature was calculated as arithmetic mean of the smoothed TFC9/3/14 and TFC15/3/14 data sets.

5. In Fig. 52 the original TC readings of TFC1/13 and TIT A/13 thermocouples as well as the calculated averaged temperature (**TFS_13**) at the elevation 950 mm are presented. The averaged temperature was calculated as arithmetic mean of the smoothed TFC1/13 and TIT A/13 data sets.

6. At the elevation 850 mm the TC readings of internal TFC1/12 and TIT C/12 thermocouples were chosen from the 5 available data sets (see Fig. 53) as the basis for the averaged temperature (**TFS_12** curve, Fig. 54).

7. At the elevation 750 mm the TC readings of internal TIT E/11 thermocouple (lower temperature values) and TFSH2/7/11 thermocouple (higher temperature values) were chosen from the 3 available data sets (see Fig. 55) as the basis for the averaged temperature (**TFS_11** curve, Fig. 56).

8. In Fig. 57 the original TC readings of TFSH20/5/10 and TFSU16/4/10 thermocouples as well as the calculated averaged temperature (**TFS_10**) at the elevation 650 mm are presented. The averaged temperature was calculated as arithmetic mean of the smoothed TFSH20/5/10 and TFSU16/4/10 data sets.

9. At the elevation 550 mm the TC readings of TFSU 9/3/9 thermocouple (lower temperature values) and TFSH4/2/9 thermocouple (higher temperature values) were chosen from the 6 available data sets (see Fig. 58) as the basis for the averaged temperature (**TFS_9** curve, Fig. 59).

At the elevations from 450 mm to -250 mm all the TFS thermocouples survived throughout the test. The average temperatures at these elevations were determined as arithmetic mean of the corresponding smoothed TFSU/TFSH curves.

The calculated average temperature curves representing temperature evolution of the bundle at 17 elevations from 1350 mm to -250 mm from the beginning of the test up to the moment of flooding initiation are given in Fig. 60. These curves were used as the boundary conditions for the effective channel walls in the S/Q code simulation of the QUENCH-12 test at the preoxidation and transient phases.

3.2 Effective channel parameters determination

The parameters of the effective channel in the present calculation were determined similarly the previous QUENCH bundle tests simulation [6-11]. However, because of the differences in geometrical sizes and in number of rods the effective channel parameters were also different here.

The following bundle parameters were used for the channel determination:

Shroud inner radius R_{shroud} = 41.75 mm;

Rod outside radius	R_{rod} = 4.565 mm;
Corner rod radius	R_{corner} = 3.0 mm;
Number of rods	N_r = 31;
Number of corner rods	N_t = 6.

The total bundle cross-section is given by the expression:

$$A_{tot} = \pi R_{shroud}^2 - N_{rod} \cdot \pi R_{rod}^2 - N_{corner} \cdot \pi R_{corner}^2 . \quad (7)$$

The value of A_{tot} is equal to 32.77 cm^2.

The value of the channel cross-section per one rod is equal to

$$A_{eff} = \frac{A_{tot}}{N_{rod} + N_{corner}} = 0.8856 \text{ cm}^2. \quad (8)$$

The effective channel inner radius is connected with the value of A_{eff} by:

$$\pi R_{eff}^2 - \pi R_{rod}^2 = A_{eff} \Rightarrow R_{eff} = \sqrt{\frac{A_{eff}}{\pi} + R_{rod}^2} = 7.002 \text{ mm} \quad (9)$$

3.3 Test simulation specifications

The calculated average temperature curves representing temperature evolution of the bundle at 17 elevations from 1350 mm to -250 mm up to the moment of reflooding initiation are given in Fig. 60. Just like in QUENCH-12 test simulation, these curves were used as the boundary conditions for the effective channel walls in the S/Q code simulation during preoxidation and transient phases of the QUENCH-12. The quenching phase of the test was simulated with the assumption of thermal equilibrium at each elevation, when the rods cooling down takes place due to interaction with the water-steam mixture.

On the basis of the effective channel parameters specified in the Subsection 3.2, the argon and steam mass flows at all the test phases were determined. By definition, inlet gas flow in the effective channel is connected with the total inlet gas flow by:

$$J_{eff} = J_{tot} \frac{A_{eff}}{A_{tot}} . \quad (10)$$

The value of argon and steam total inlet flow rate was specified to be constant and equal to 3.3 g/s.

At 7270 sec. the argon/steam flow was stopped and water flooding began with flow rate of J_{flood} = 48 g/s. The estimated kinematical velocity of water level motion (without accounting for evaporation and two-phase water-steam regions formation) is given by

$$U_{flood} = \frac{J_{flood}}{A_{tot}} = 1.46 \text{ cm/s.} \quad (11)$$

Time step throughout the test values were:

1.0 s up to 6000 s,

0.1 s up to 7550 s (end of the calculation)

The bundle nodalization is characterised by the following values:

Heat conduction module

- The total nodes number in the radial direction: 35
- Pellet nodes number in the radial direction: 21
- External layer (oxide) nodes number: 7
- Total nodes number in the vertical direction: 197

The vertical grid used in the heat conduction module is adaptive one, with maximum density in the region of the maximum temperature axial gradients.

Total number of meshes used by oxidation, mechanical deformation and hydrogen absorption modules was 98. The total central rod length considered was 1975 mm – from the upper point 1500 mm (adjacent to the Al_2O_3 plate thermal shield) to the lower point -475 mm (adjacent to the lower SS plate).

3.4 Calculated temperatures

In this subsection the calculated temperature evolution curves at the different elevations of the central rod are presented.

In Fig. 61 the experimentally measured temperatures at the elevation 1350 mm by TFC18/4/17 and TFSU11/3/17 thermocouples as well as the calculated temperature evolution of the central rod outer surface at this elevation are presented.

In Fig. 62-64 the analogous comparison between the experimentally measured temperatures at the elevations 1250, 1150 and 1050 mm and the calculated temperature evolution of the central rod outer surface at these elevations is given.

In Fig. 65-68 the comparison between the experimentally measured temperatures at the elevations 950, 850, 750 and 650 mm and the calculated temperature evolution of the central rod outer surface at these elevations is given.

As one can see, calculated temperature evolution curves generally show good correlation with the experimentally measured ones during preoxidation and transient phases of the test. All the characteristic bends of these test phases were very closely reproduced by the calculations.

In Fig. 69-72 the experimentally measured temperatures of the rod outer surface at the elevations 1050, 950, 750 and 650 mm and calculated temperature evolutions at these elevations at the quenching phase of the test (7200-7600 sec.) are presented. Quite similar to QUENCH-06 test simulation the calculated curves show higher cooling rates and do not reproduce the 'gap' of some of the experimental ones: sharp drop of the temperature with following increase of it. Such temperature behaviour may be here also explained by some local thermocouple effect due to fast water injection at the onset of quenching and following heat exchange with the water-steam mixture under confined geometry conditions.

Generally, calculated temperature evolution curves demonstrate rather good correlation with the experimental ones in oxidation, transient and quenching phases of the test.

3.5 Oxide layer thickness

At first the main attention was paid to the comparison of the calculated oxide layer axial profile with the measured one. The experimental information about the oxide layer thickness is available at 5972 s when the corner rod **D** was withdrawn from the bundle, at 7158 s when the corner rod **F** was withdrawn and at the end of the experiment.

The obtained simulation results show that at 5972 s the calculated oxide thickness is in good agreement with the experimental data of rod **D** (Fig. 73). Calculations show good agreement with the experimentally measured oxide thickness at the elevation 940 mm of rod **F**, however, at 700 mm and at 1120 mm the calculated oxide thickness was seriously underestimated (Fig. 74, blue line).

As it was mentioned above, rather high temperature radial non-uniformity took place in QUENCH-12 test due to the fact that in this test only 18 heated rods were used from the total number of 31. That is why one may think that while being determined as an 'average of the available reliable temperature data' the temperature of the effective channel walls was underestimated. That could lead to the underestimation of the calculated oxide thickness at certain elevations since oxidation kinetics is extremely temperature-dependent: the higher the temperature, the higher is the oxidation rate. To clarify this point the additional simulation of the QUENCH-12 test with the temperature of the effective channel walls based on *the highest values of temperature* at each elevation was performed. The result of such calculation is presented in Fig. 74 by black line. As one can see, underestimation of the oxide thickness at 700 mm and at 1120 mm takes place in this calculation using highest possible temperatures as well.

In Fig. 75 the measured oxide layer thickness (estimated on the basis of residual metal layer thickness, see the following paragraph) of corner rod B, central rod, and averaged value for 31 rods at the end of the test are compared to the calculated oxide layer profile of the central rod (final state). The calculation was performed using average temperatures (blue line) and highest temperatures (black line) at each elevation as the basis for the effective channel wall temperature. Here we also have substantial underestimation of the calculated oxide thickness in both calculations, especially at the elevation 950 mm, where cladding was completely oxidized.

The possible explanation of such underestimation of the oxide thickness by the S/Q code may consist in the fact that, as the central rod was presumably kept at about 1200ºC (at 950 mm elevation) during preoxidation, a part of the bundle had rather lower temperatures (by 100-150 K, as it was discussed above, in subsection 3.1). At such temperatures so-called 'break-away' effect takes place with kinetics of oxidation different from ordinary parabolic law. Massive spallation of the oxide scales observed in the course of posttest examinations [2] indicates that break-away oxidation took place in a considerable part of the bundle. Thus, oxidation kinetics in QUENCH-12 test was quite different from that of QUENCH-06. At the transient phase of the test when the temperatures in the hottest part of the bundle increased up to 2100 K, more intense oxidation (through friable cracked oxide structure formed due to break-away effect) took place. This process led to complete oxidation of cladding at the elevation 950 mm.

The model for the break-away oxidation has not been yet developed and installed in the S/Q code. That is why calculations give substantial underestimation of the oxide thickness. In Fig. 76 the comparison of the calculated oxide layer thickness axial profiles in QUENCH-06 (where the calculations agree with experimental data, see Fig. 39) and QUENCH-12 tests is presented. We note here that in both calculations the identical set of models for oxidation and other physical-chemical phenomena were used. The calculated oxide layer in QUENCH-12 simulation is lower than that in QUENCH-06, this generally agrees with lower temperatures in the QUENCH-12 test. The fact that the experimentally measured oxide thickness in QUENCH-12 test is much higher than the calculated ones definitely points to the fact that in this last test the kinetics of oxidation was quite different.

3.6 Hydrogen release analysis

In spite of the discussed above non-uniformity of the radial temperature distribution inside the bundle in the QUENCH-12 test we will estimate the total hydrogen production rate of the whole bundle $\dot{m}_{bundle}$ in a way similar to the QUENCH-06 simulation (see subsection 2.6). The value of $\dot{m}_{bundle}$ is assumed to be connected with calculated central rod production rate $\dot{m}_{rod}$ by the relation:

$$\dot{m}_{bundle} = A \cdot \dot{m}_{rod}, \quad A = N_{rod} + N_{corner} \frac{R_{corner}}{R_{rod}} + \frac{R_{shroud}}{R_{rod}} = 44.09 \tag{12}$$

Here $N_{rod} = 31$ is the number of heated and unheated rods (including central rod), $N_{corner} = 6$ is the number of corner rods, R_{corner}, R_{rod} and R_{shroud} are heated rod, corner rod and shroud radii correspondingly, specified for the case of VVER bundle in subsection 3.2.

In Fig. 77 hydrogen production rate calculated according to relation (12) on the basis of S/Q code simulation and the experimental data are presented. As one can see, the calculated curve is in rather good agreement with the experimental one during the preoxidation and temperature escalation phases of the test.

Fig. 78 shows experimentally measured and calculated hydrogen production rate during second part of the temperature escalation phase and quenching phase. Calculated curve is located lower than the experimental one starting from 7100-7150 s. The experimentally measured peak at the onset of quenching is much higher than the calculated one.

According to the calculation results, the total amount of generated hydrogen is 32.5 g (experimental value is 58 g [2]). Amount of calculated hydrogen released during quenching phase of the test is 9.9 g, while experimental value is 24 g. Considerable underestimation of the hydrogen production rate at the latest phases of the test can be explained by the fact that more intense oxidation through friable cracked oxide structure (formed due to break-away effect) took place during transient and flooding. As it was discussed above, S/Q code is not able to describe this phenomenon since the model for the break-away oxidation has not been yet installed.

In Fig. 79-80 the comparison of the calculated hydrogen production rates in Q-06 and Q-12 tests simulation is presented. Noticeable is practically identical behavior of the two curves during preoxidation and transient phases of the test up to 7075 s. The ratio of the square of the surfaces exposed to oxidation in QUENCH-06 and QUENCH-12 tests is given by

$$r = \frac{\left(A \cdot R_{rod}\right)_{Q-06}}{\left(A \cdot R_{rod}\right)_{Q-12}} = 0.82 \qquad (13)$$

with the values of A and R_{rod} from relations (6) and (12). The fact that hydrogen production rates in Fig. 79 almost coincide, together with the above ratio point to the fact that during preoxidation and transient phases the temperatures in QUENCH-12 test were generally lower than in QUENCH-06 one, as it was mentioned above. The shape of the peaks in Fig. 80 is similar, and their shift from each other is due to different moments of the flooding onset in the two tests.

3.7 Summary of the QUENCH-12 test simulation

- SVECHA/QUENCH code was applied to the simulation of the QUENCH bundle test Q-12. The calculations adequately reproduce temperature evolution of the central rod at different elevations during the whole test duration with some discrepancies at the quenching phase.

- The calculated oxide axial profile agrees quite well with the experimental data at the time moment 5972 s when the corner rod D was withdrawn from the bundle.

- The calculated oxide thickness agrees quite well with the experimental data at 940 mm but is significantly lower at 700 and 1120 mm at the time moment 7158 s when the corner rod F was withdrawn from the bundle. This fact may be explained by 'break-away' oxidation at relatively low temperatures.

- The calculated oxide thickness at the end of the test was significantly underestimated, especially at 950 mm. This fact may be explained by more intensive oxidation during transient and quenching phases through friable cracked oxide structure formed due to break-away oxidation at the previous phases of the test.

- The details of the experimentally measured time dependence of the hydrogen production rate are well reproduced by the calculations at the preoxidation and transient phases. Calculations underestimate hydrogen production rate at the end of transient and quenching phase of the test.

4 General Summary and conclusions

- SVECHA/QUENCH code was applied to the simulation of the bundle tests QUENCH-06 and QUENCH-12.

- Performed calculations adequately reproduce temperature evolution of the central rod at different elevations during the whole test duration with some discrepancies at the quenching phase. Calculations show adequate work of the code with respect to oxide axial profile and hydrogen production rate.

- The difference between experimental data and calculation results in QUENCH-12 test is due to break-away oxidation of the bundle. Model for break-away oxidation has not been yet developed and implemented in the SVECHA/QUENCH code.

- Comparison of the calculated oxide axial profile and hydrogen production rate of the QUENCH-06 and QUENCH-12 tests shows that two tests are quite similar to each other in terms of bundle temperature evolution: similarity in temperatures leads to similarity in oxide axial profiles and hydrogen production rates.

Acknowledgements

The authors are grateful to Mr. L. Sepold for his interest to this work, important comments and fruitful discussions.

References

1. *L.Sepold, W.Hering, C.Homann, A.Miassoedov, G.Schanz, U.Stegmaier, M.Steinbrueck, H.Steiner, J.Stuckert,* Experimental and Computational Results of the QUENCH-06 Test (OECD ISP-45), FZKA 6664, 2004;

2. *J.Stuckert, M.Heck, A.Goryachev, M.Große, L.Sepold, U.Stegmaier, M.Steinbrück*, Results of the QUENCH-12 Experiment with a Russian VVER-type Bundle, FZKA 7307, 2007;

3. *P.Hofmann, V.Noack, M.S.Veshchunov, A.V.Berdyshev, A.V.Boldyrev, L.V.Matweev, A.V.Palagin, V.E.Shestak,* Physico-Chemical Behavior of Zircaloy Fuel Rod Cladding Tubes During LWR Severe Accident Reflood, FZKA 5846, 1997;

4. *P.Hofmann, A.Miassoedov, L.Steinbock, M.Steinbrueck, M.S.Veshchunov, A.V.Berdyshev, A.V.Boldyrev, A.V.Palagin, V.E.Shestak*, Quench Bechaviour of Zircaloy Fuel Rod Cladding Tubes. Small-Scale Experiments and Modeling of the Quench Phenomena, FZKA 6208, 1998;

5. *A.V.Berdyshev, A.V.Boldyrev, A.V.Palagin, V.E.Shestak, M.S.Veshchunov*, SVECHA/QUENCH Code for The Modeling of Reflooding Phenomena in Severe Accidents Conditions. Proceedings of the Ninth International Topical Meeting on Nuclear Reactor Thermal Hydraulics (NURETH-9), paper Log_19 (CD-ROM edition), San Francisco, California, USA, October 1999;

6. *A.V.Palagin,* Application of the SVECHA/QUENCH Code to the Simulation of the Bundle Test QUENCH-10, FZKA 7268, 2007;

7. *L.Sepold, P.Hofmann, C.Homann, W.Leiling, A.Miassoedov, D.Piel, G.Schanz, L.Schmidt, U.Stegmaier, M.Steinbrueck, H.Steiner, A.V.Palagin, A.V.Boldyrev, M.S.Veshchunov, A.V.Berdyshev, V.E.Shestak*, Investigation of an Overheated PWR-Type Fuel Rod Simulator Bundle, FZKA 6412, 2001;

8. *M.S.Veshchunov, A.V.Boldyrev, A.V.Palagin, V.E.Shestak*. Application of the SVECHA/QUENCH code to the simulation of the QUENCH bundle test Q-07. IBRAE Report NSI-SARR-184-04, Moscow, December 2004;

9. *M.S.Veshchunov, A.V.Berdyshev, A.V.Boldyrev, A.V.Palagin, V.E.Shestak, M.Steinbrück, J.Stuckert*. Modelling of B_4C oxidation by steam at high temperatures based on separate-effects tests and its application to the bundle experiment QUENCH-07, FZKA 7118, 2005;

10. *M.S.Veshchunov, A.V.Boldyrev, A.V.Palagin, V.E.Shestak*. Application of the SVECHA/QUENCH code to the simulation of the QUENCH bundle test Q-08. IBRAE Report NSI-SARR-189-05, Moscow, June 2005;

11. *J.Stuckert, A.V.Boldyrev, A.Miassoedov, A.V.Palagin, G.Schanz, L.Sepold, V.E.Shestak, U.Stegmaier, L.Steinbock, M.Steinbrück, H.Steiner, M.S.Veshchunov*, Experimental and Computational Results of the QUENCH-08 Experiment (Reference to QUENCH-07) FZKA 6970, 2005;

12. *M.Steinbrück, A.Miassoedov, G.Schanz, L.Sepold, U.Stegmaier, H.Steiner, J.Stuckert*, Results of the QUENCH-09 experiment with a B4C control rod, FZKA 6829, 2004.

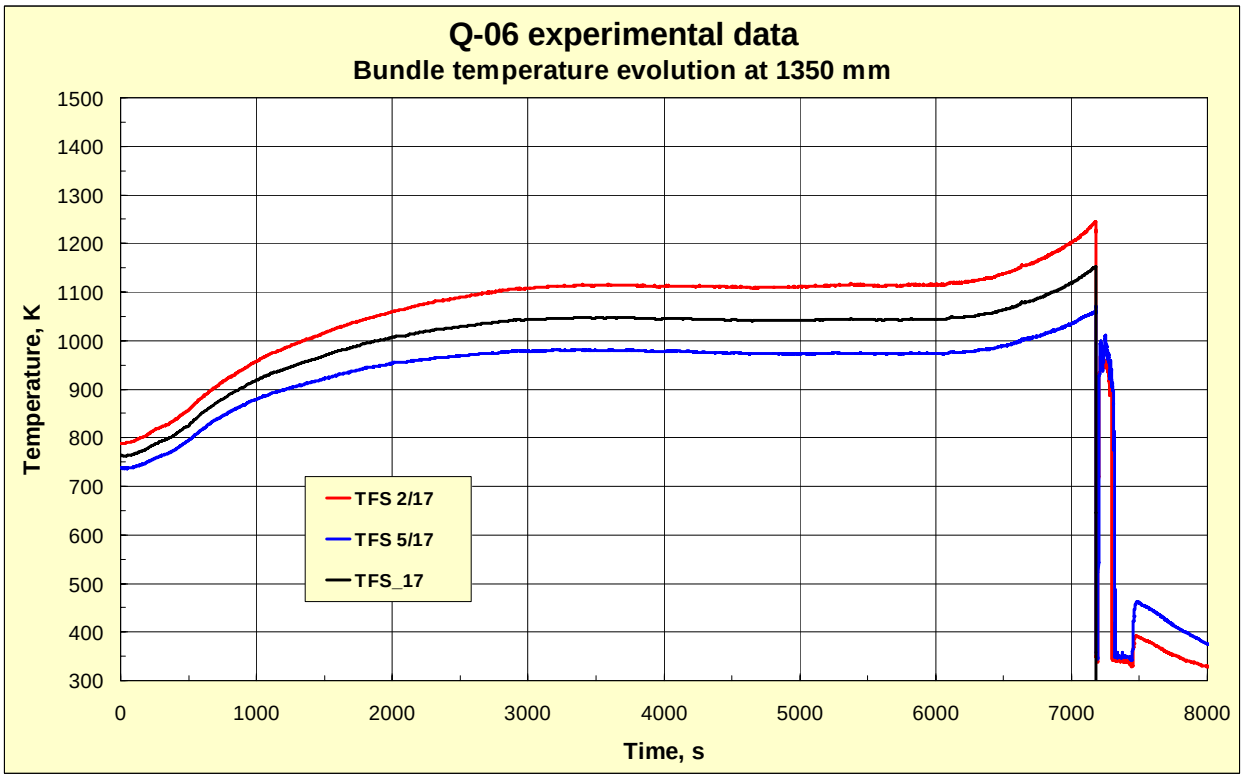

Fig 1. Bundle temperature evolution at the elevation 1350 mm measured by thermocouples TFS 2/17 (red line), TFS 5/17 (blue line) and averaged temperature used in the calculations (black line)

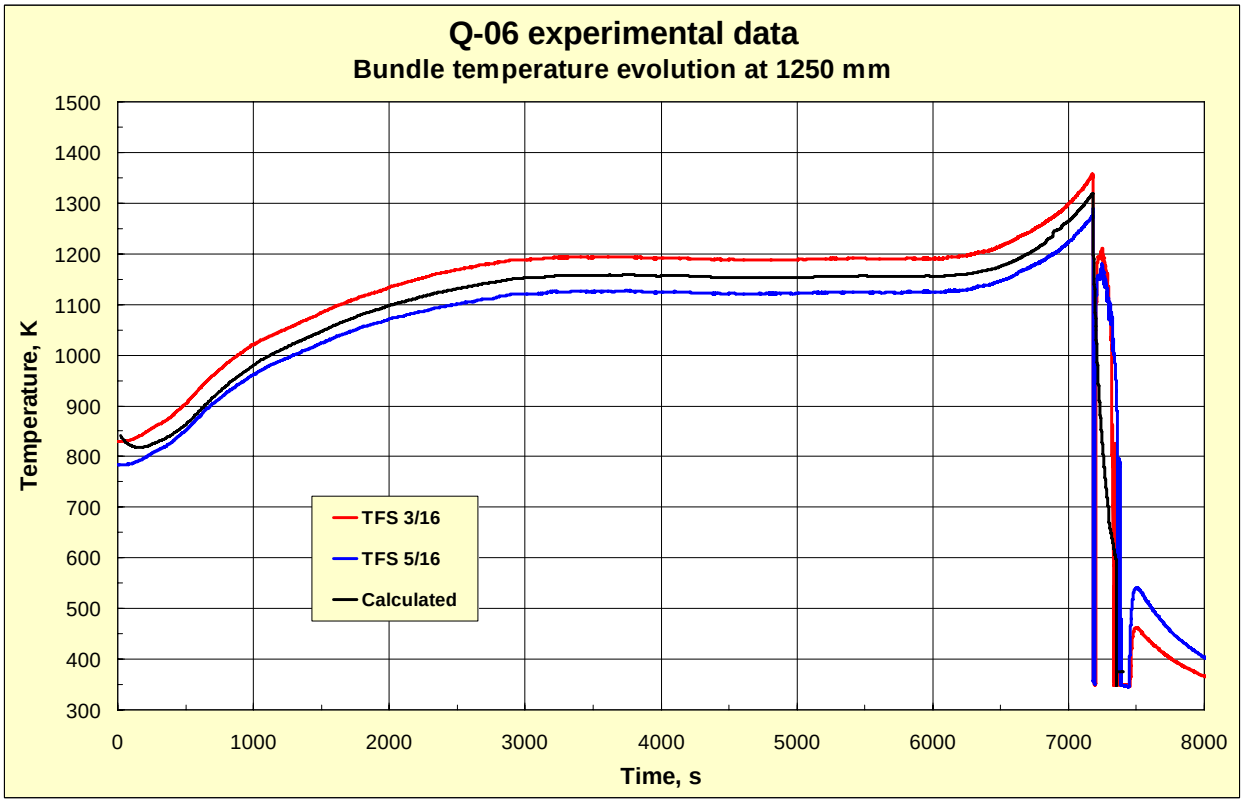

Fig 2. Bundle temperature evolution at the elevation 1250 mm measured by thermocouples TFS 3/16 (red line), TFS 5/16 (blue line) and averaged temperature used in the calculations (black line)

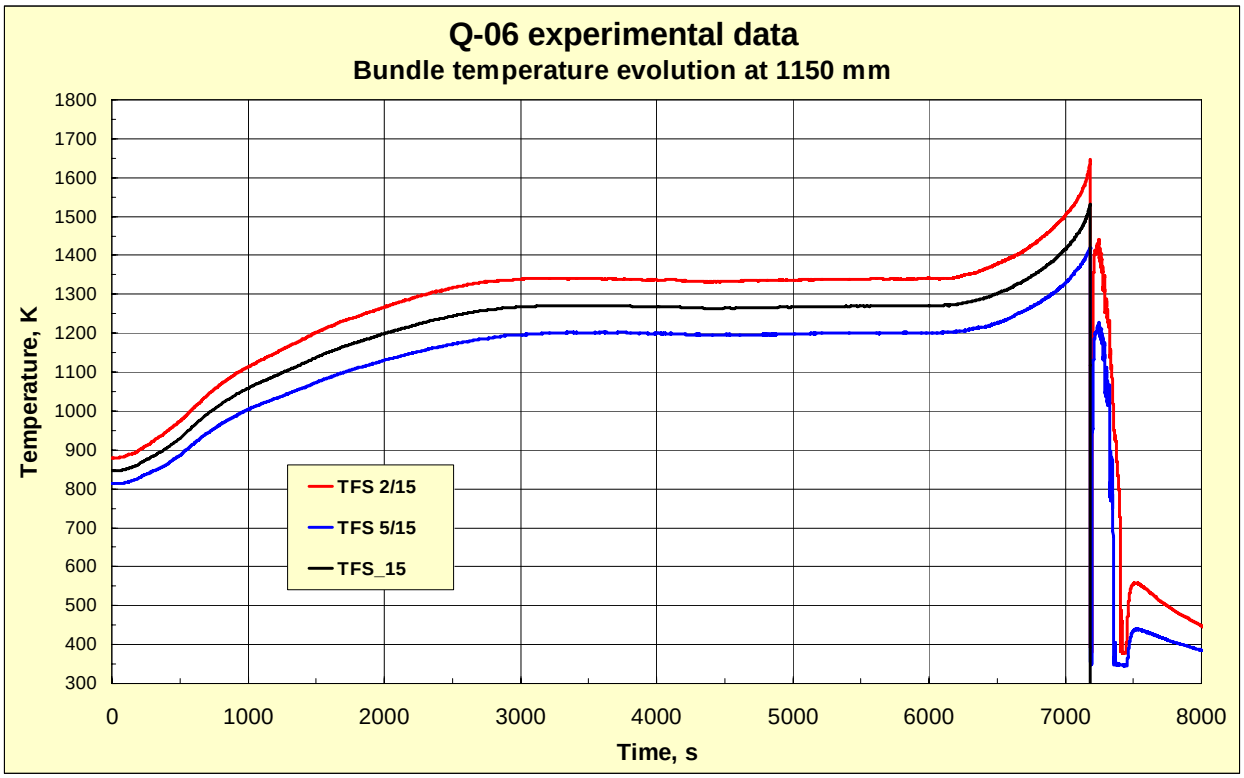

Fig 3. Bundle temperature evolution at the elevation 1150 mm measured by thermocouples TFS 2/15 (red line), TFS 5/15 (blue line) and averaged temperature used in the calculations (black line)

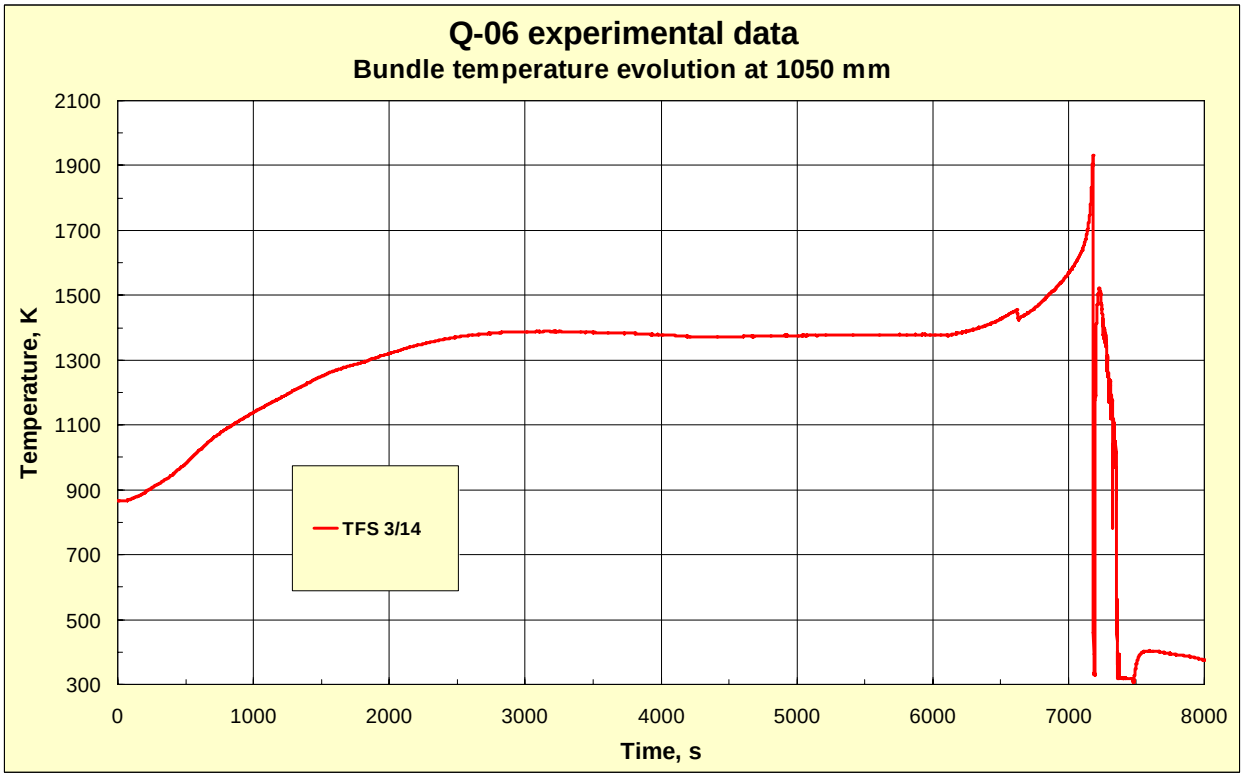

Fig 4. Bundle temperature evolution at the elevation 1050 mm measured by thermocouple TFS 3/14 used in the calculations

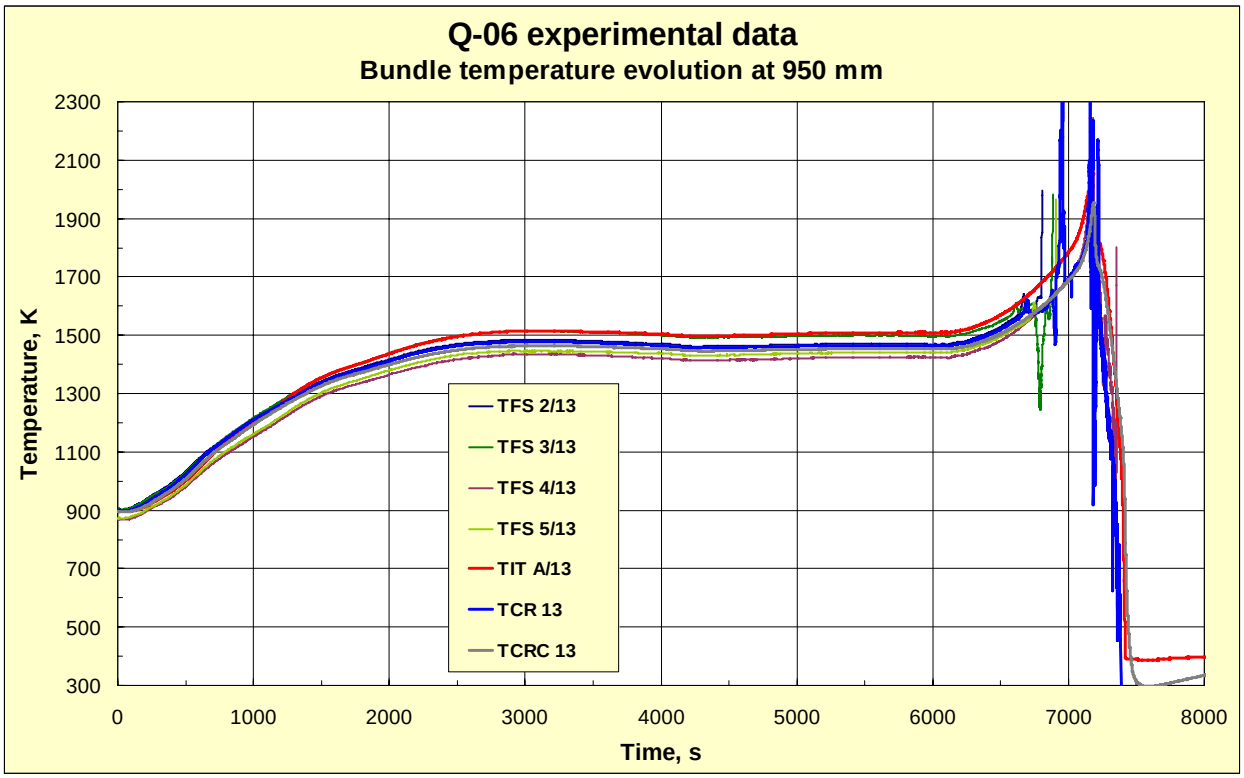

Fig 5. Bundle temperature evolution at the elevation 950 mm measured by thermocouples TFS 2/13 (dark blue line), TFS 3/13 (green line), TFS 4/13 (plum line), TFS 5/13 (goldgreen line), corner rod thermocouple TIT A/13 (red line), central rod thermocouples TCR 13 (blue line) and TCRC 13 (grey line)

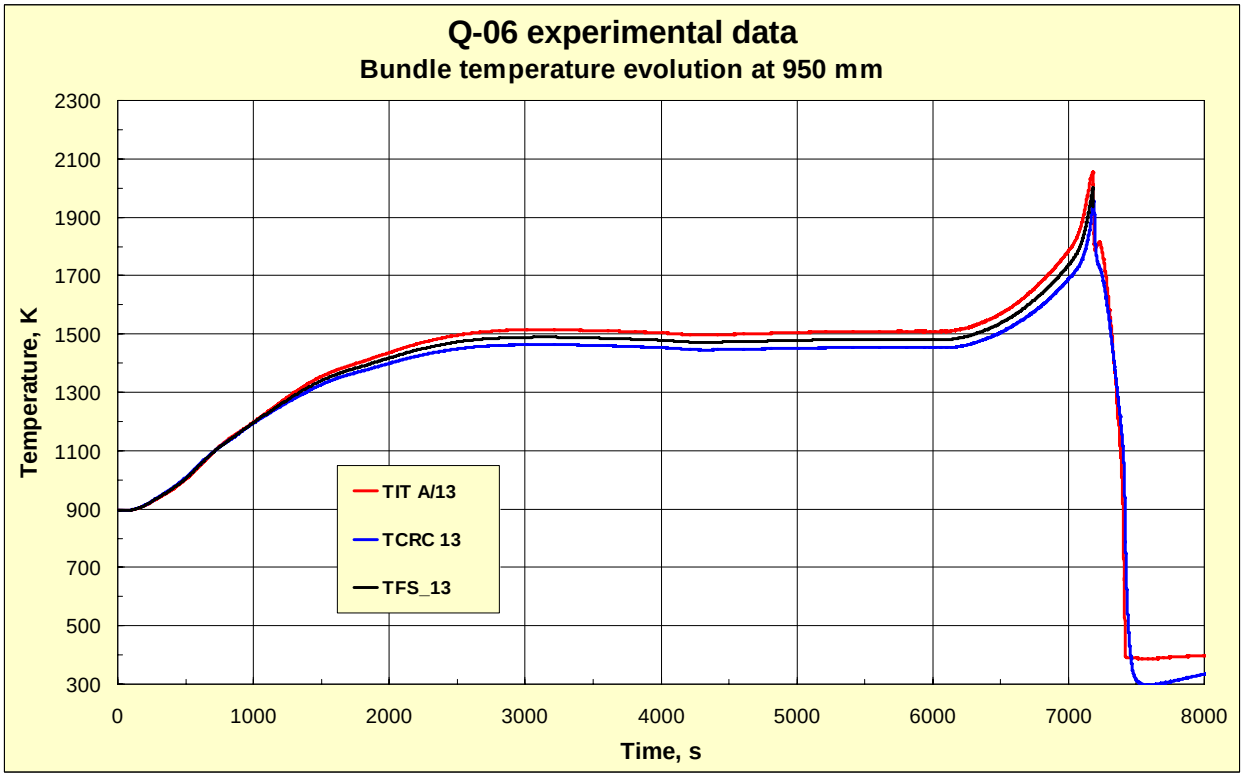

Fig 6. Bundle temperature evolution at the elevation 950 mm measured by corner rod thermocouple TIT A/13 (red line), central rod thermocouple TCRC 13 (blue line), and averaged temperature used in the calculations (black line)

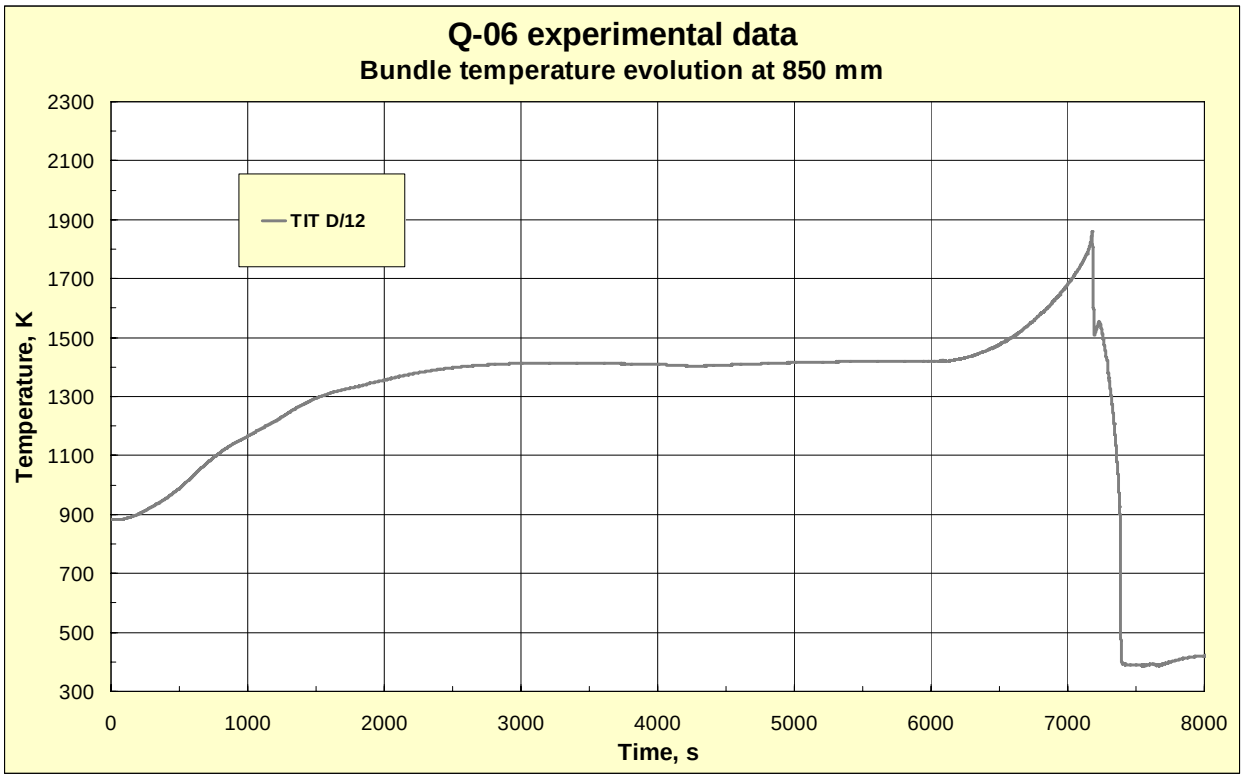

Fig 7. Bundle temperature evolution at the elevation 850 mm measured by thermocouple TIT D/12 used in the calculations

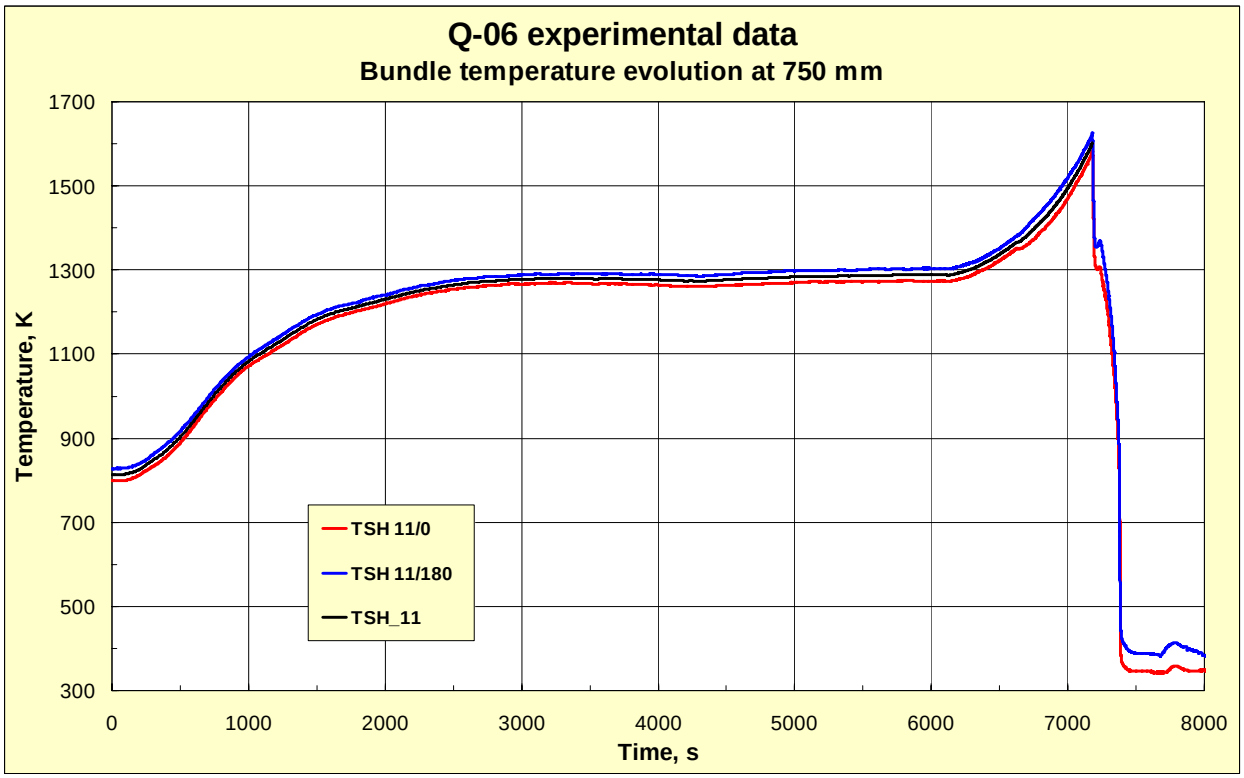

Fig 8. Bundle temperature evolution at the elevation 750 mm measured by thermocouples TSH 11/0 (red line), TSH 11/180 (blue line) and averaged temperature used in the calculations (black line)

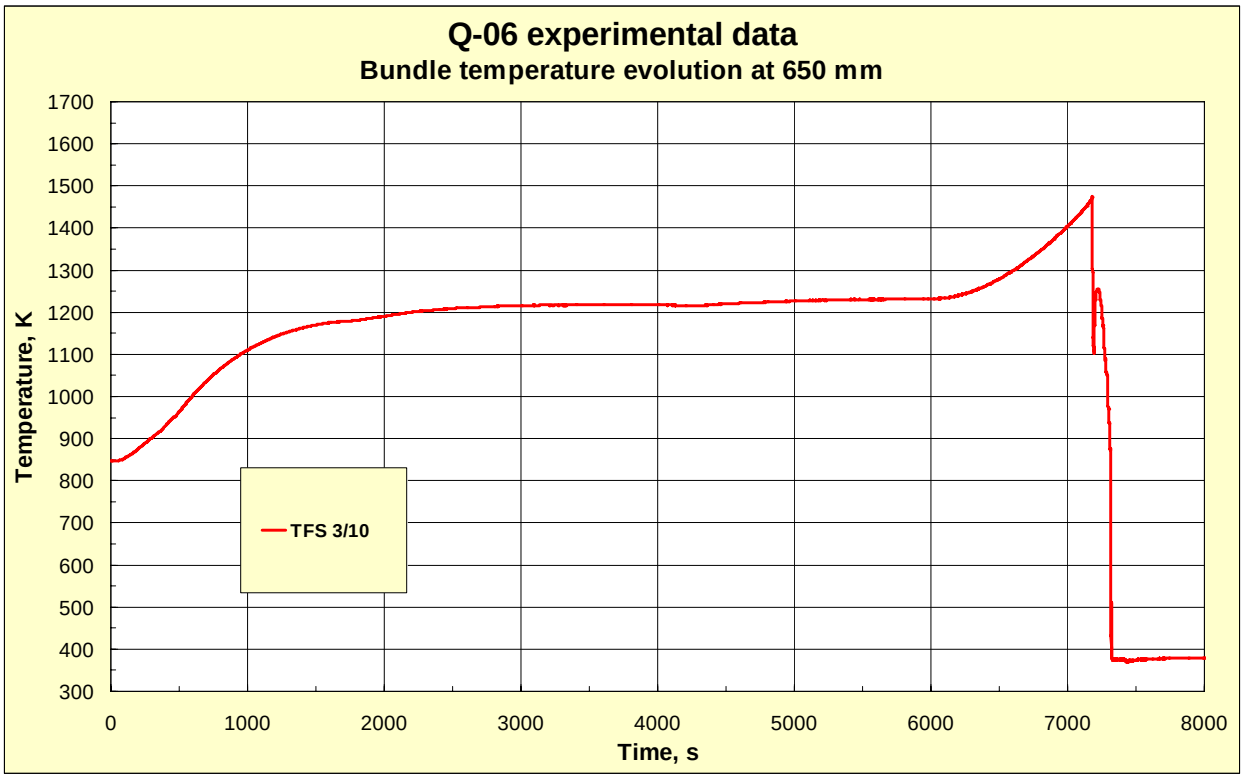

Fig 9. Bundle temperature evolution at the elevation 650 mm measured by thermocouple TFS 3/10 used in the calculations

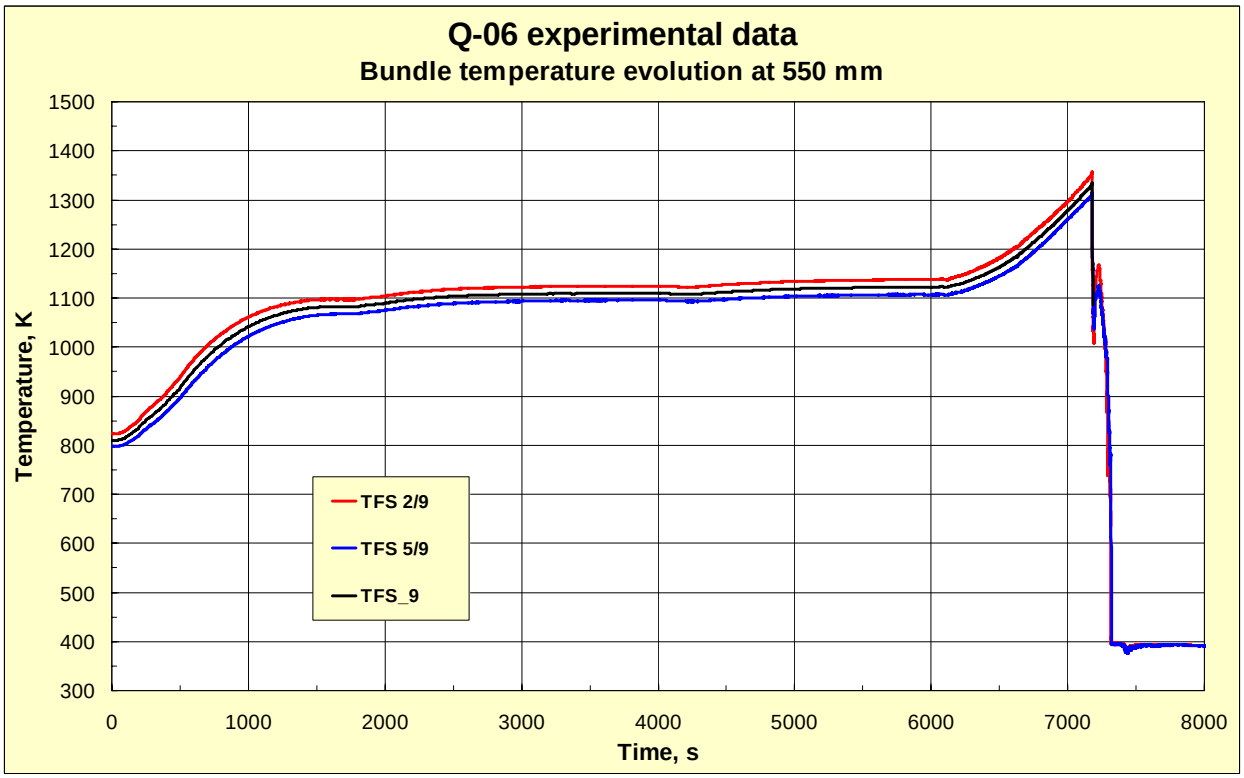

Fig 10. Bundle temperature evolution at the elevation 550 mm measured by thermocouples TFS 2/9 (red line), TFS 5/9 (blue line), and averaged temperature used in the calculations (black line)

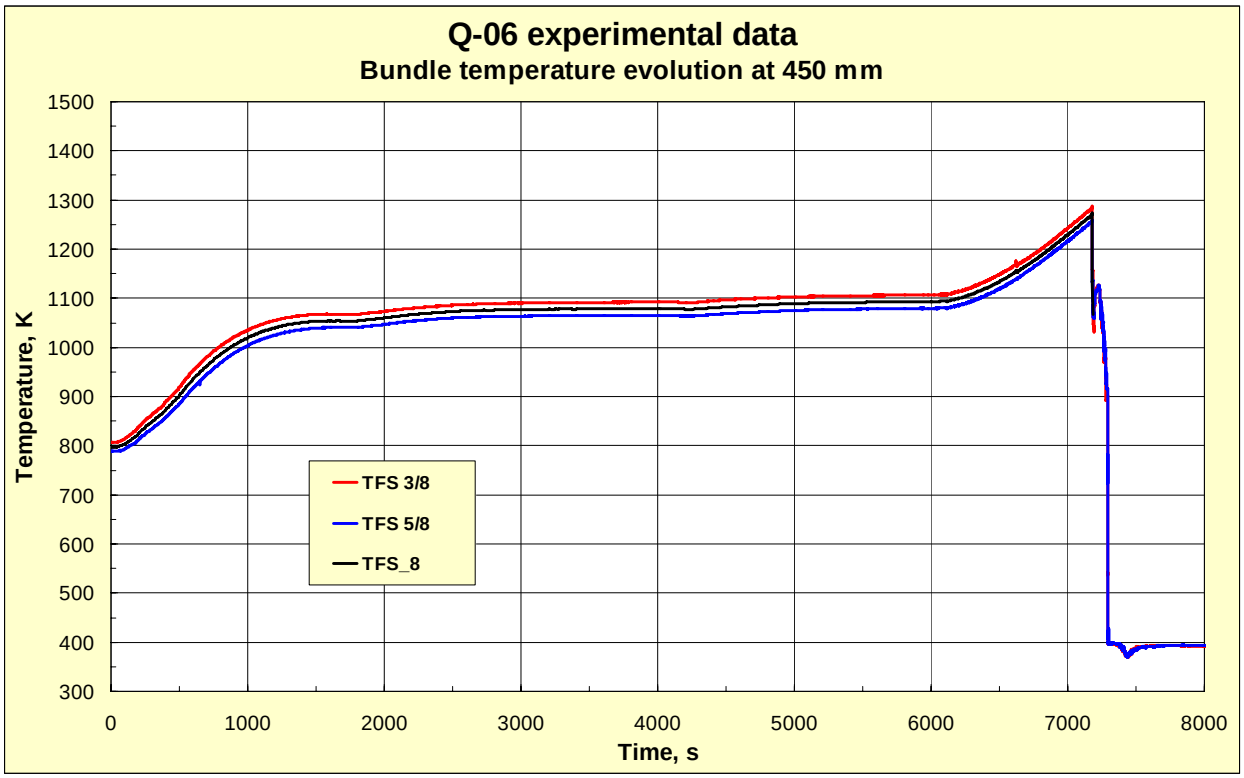

Fig 11. Bundle temperature evolution at the elevation 450 mm measured by thermocouples TFS 3/8 (red line), TFS 5/8 (blue line), and averaged temperature used in the calculations (black line)

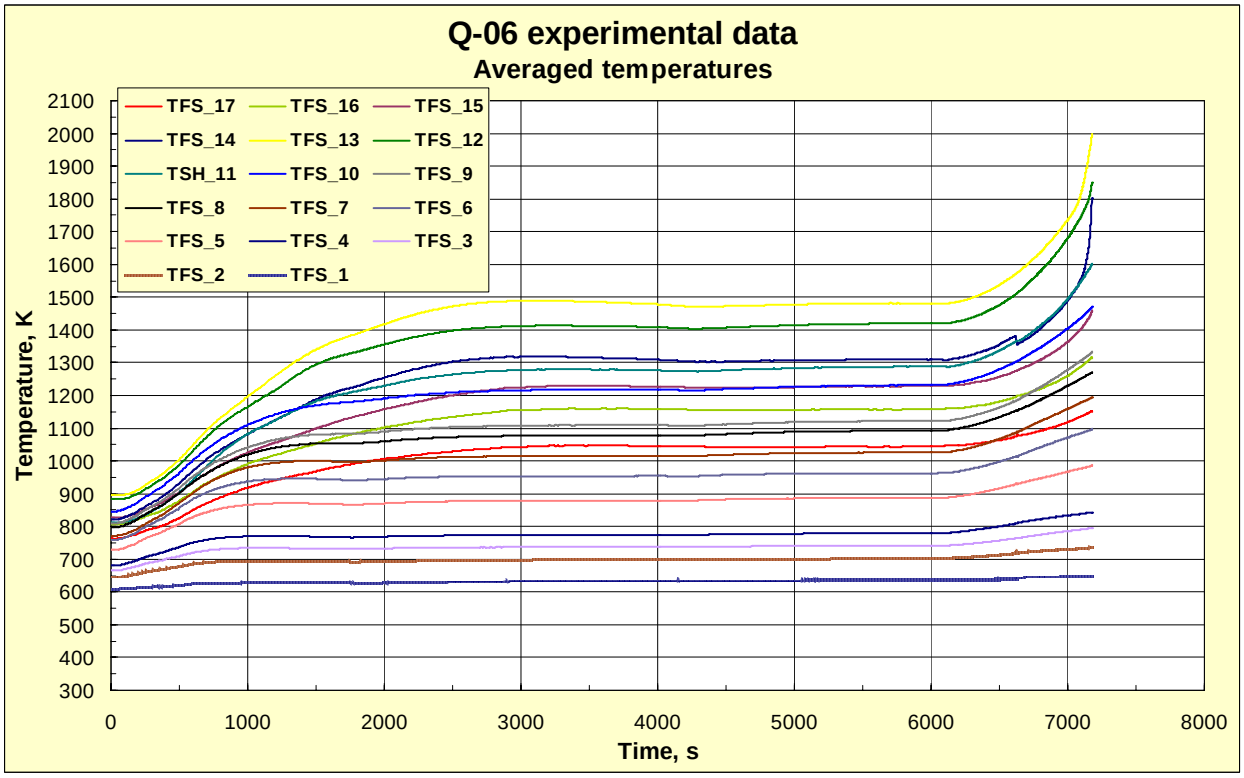

Fig 12. Averaged and smoothed curves representing temperature evolution of the QUENCH-06 bundle at the elevations from 1350 to -250 mm

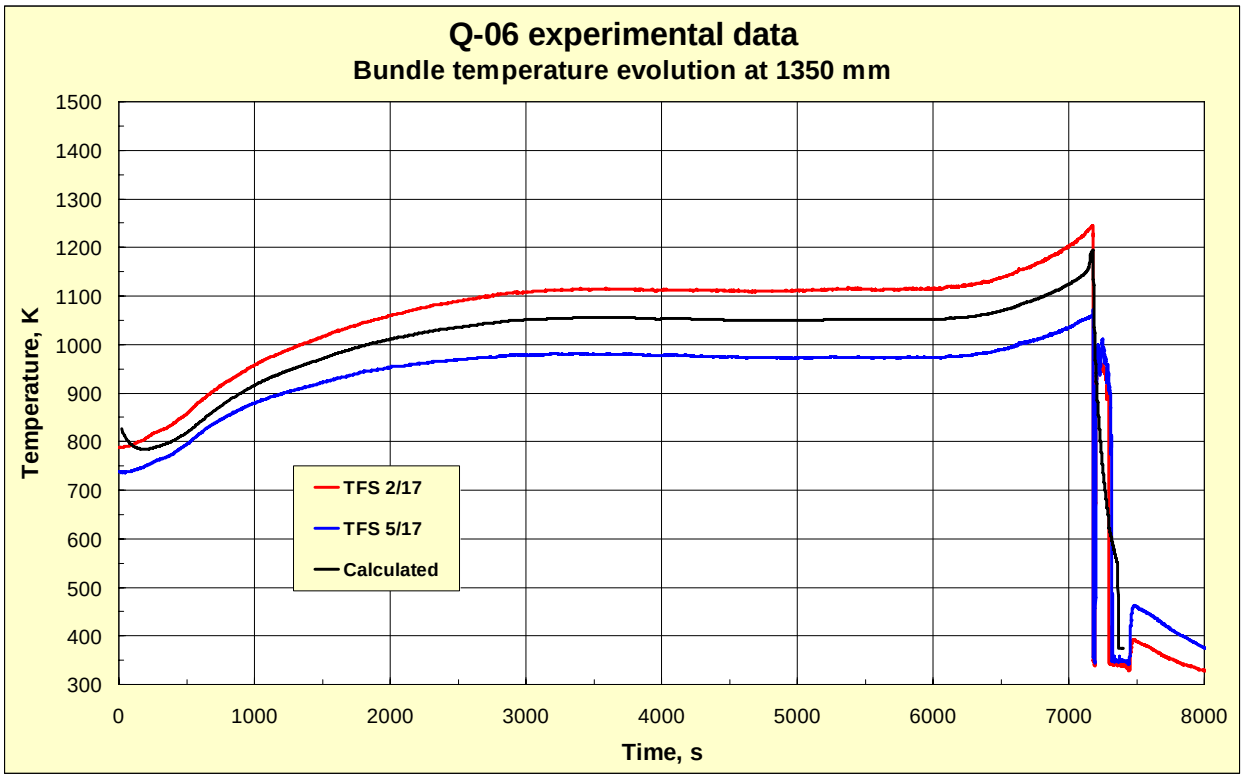

Fig 13. The experimentally measured temperatures at the elevation 1350 mm: TFS2/17 data (red line) and TFS5/17 data (blue line) and calculated temperature evolution of the central rod outer surface (black line)

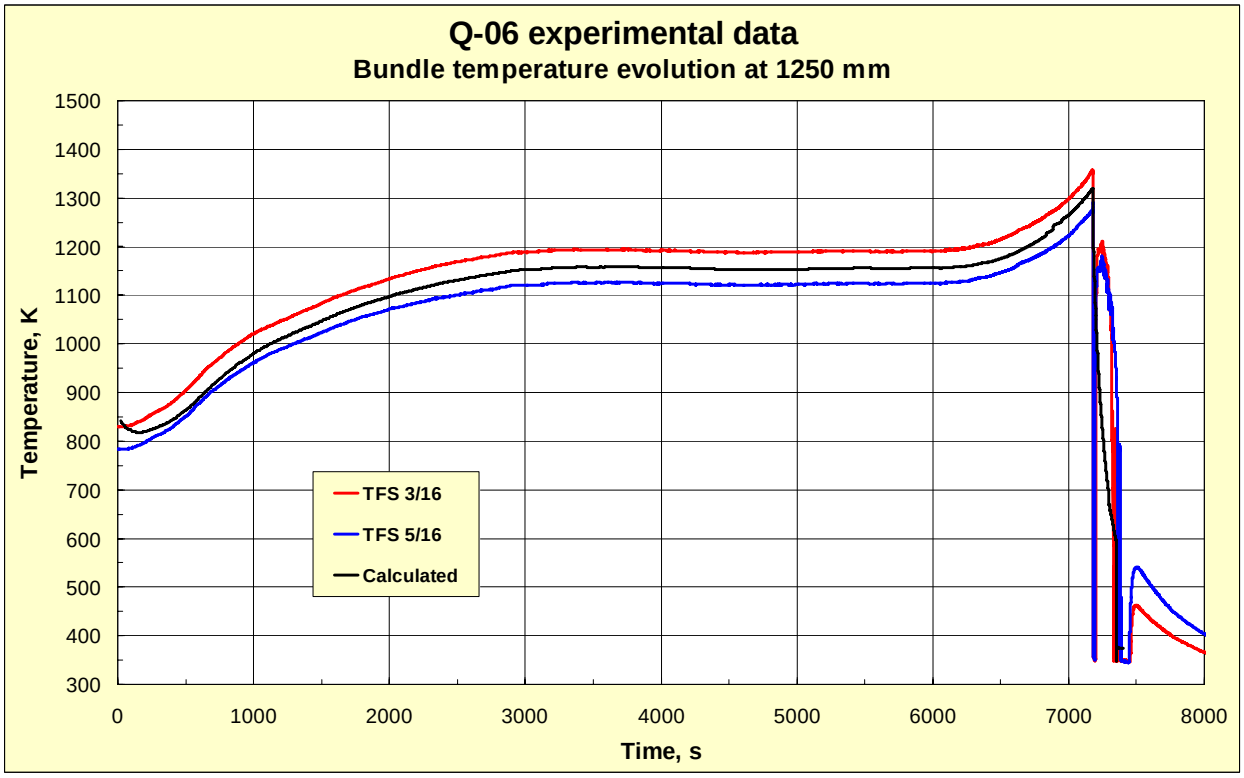

Fig 14. The experimentally measured temperatures at the elevation 1250 mm: TFS3/16 data (red line) and TFS5/16 data (blue line) and calculated temperature evolution of the central rod outer surface (black line)

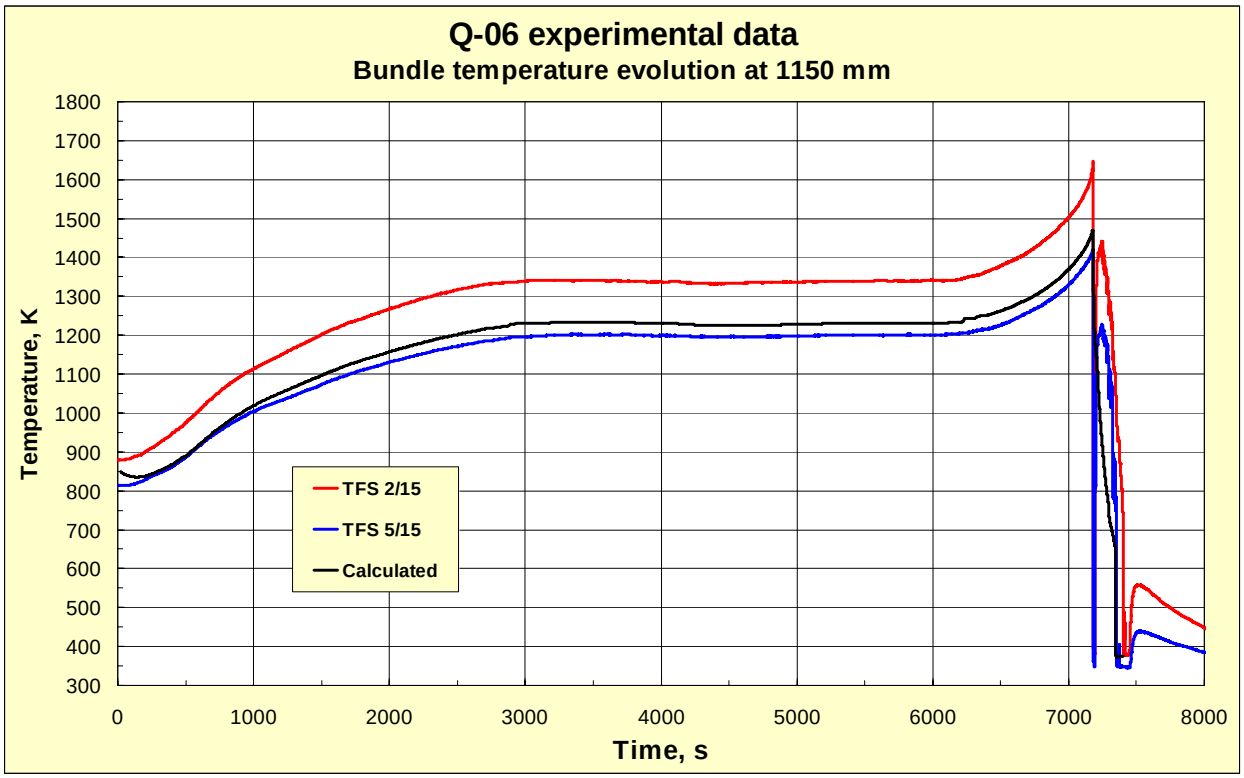

Fig 15. The experimentally measured temperatures at the elevation 1150 mm: TFS2/15 data (red line) and TFS5/15 data (blue line) and calculated temperature evolution of the central rod outer surface (black line)

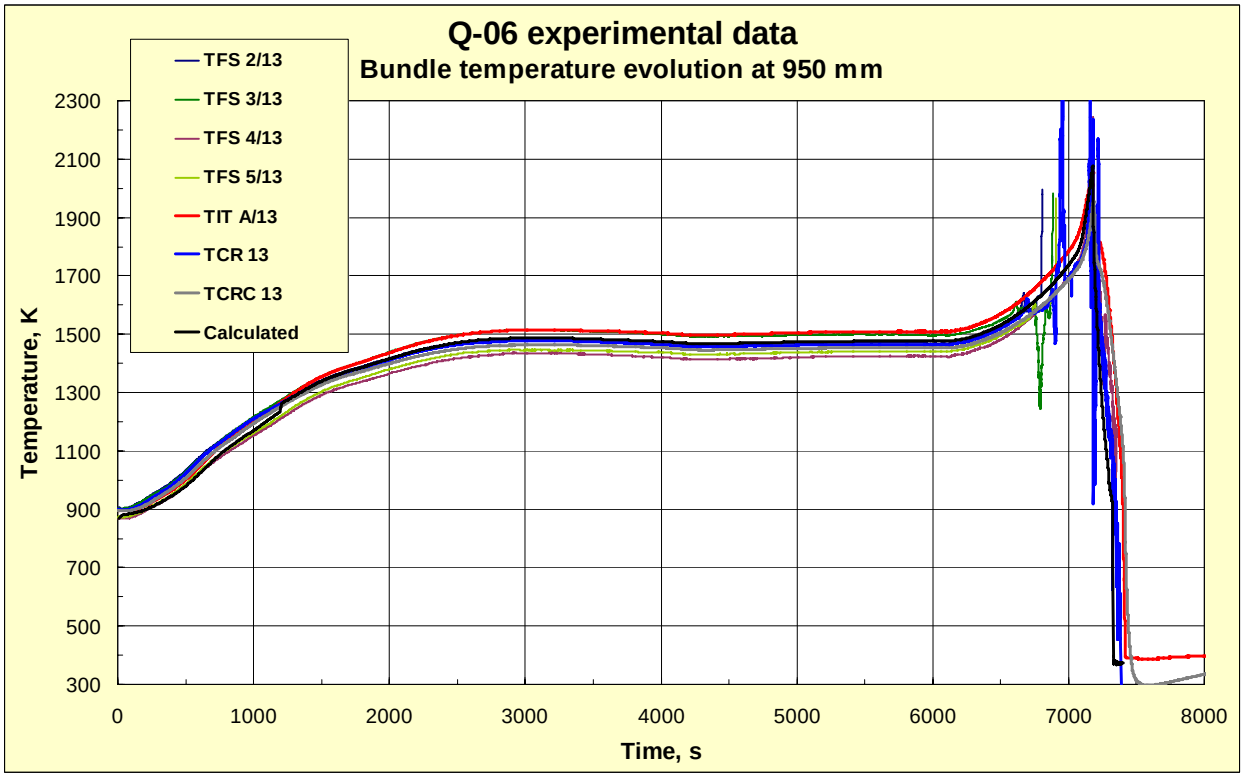

Fig 16. The experimentally measured temperatures at the elevation 950 mm: TFS2/13 data (dark blue line), TFS3/13 (green line), TFS 4/13 (plum line), TFS 5/13 (goldgreen line), TIT A/13 (red line), TCR 13 (blue line) and TCRC 13 (grey line) and calculated temperature evolution of the central rod outer surface (black line)

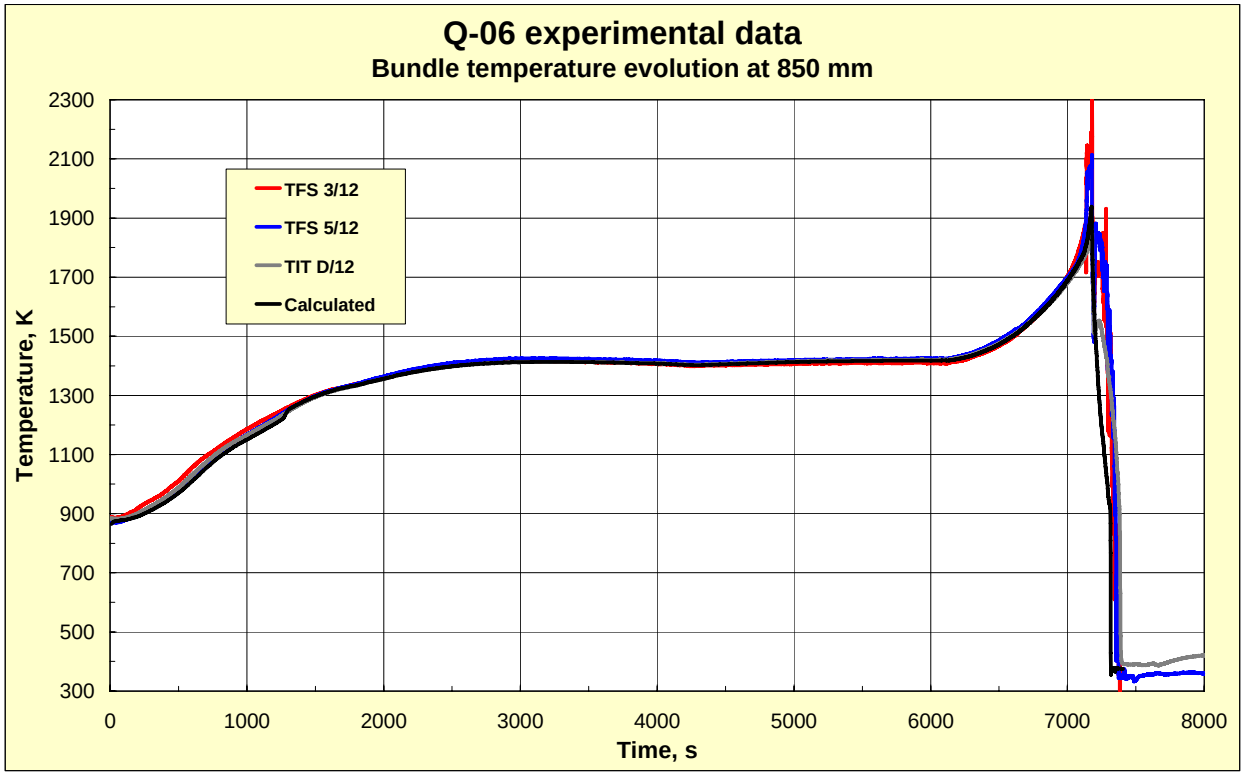

Fig 17. The experimentally measured temperatures at the elevation 850 mm: TFS 3/12 (red line), TFS 5/12 (blue line), TIT C/12 data (grey line) and calculated temperature evolution of the central rod outer surface (black line)

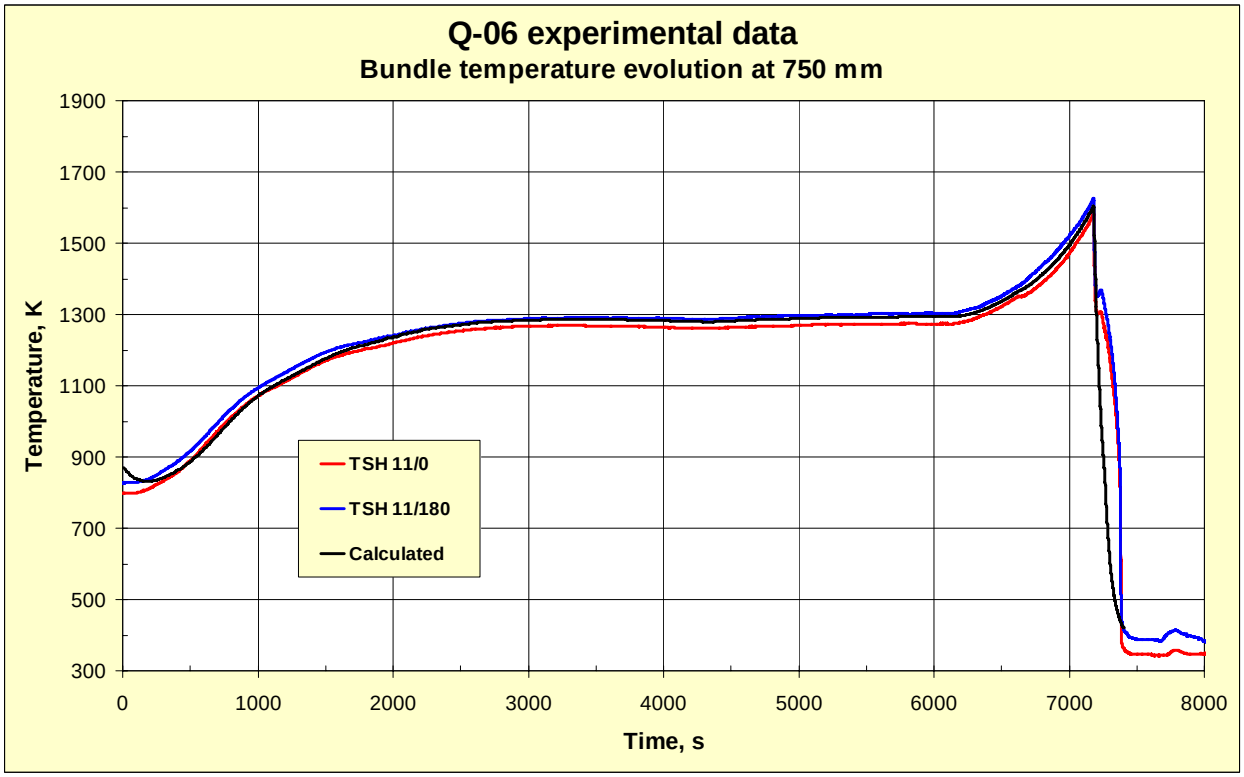

Fig 18. The experimentally measured temperatures at the elevation 750 mm: TSH 11/0 data (red line), TSH 11/180 data (blue line) and calculated temperature evolution of the central rod pellet's centre (black line)

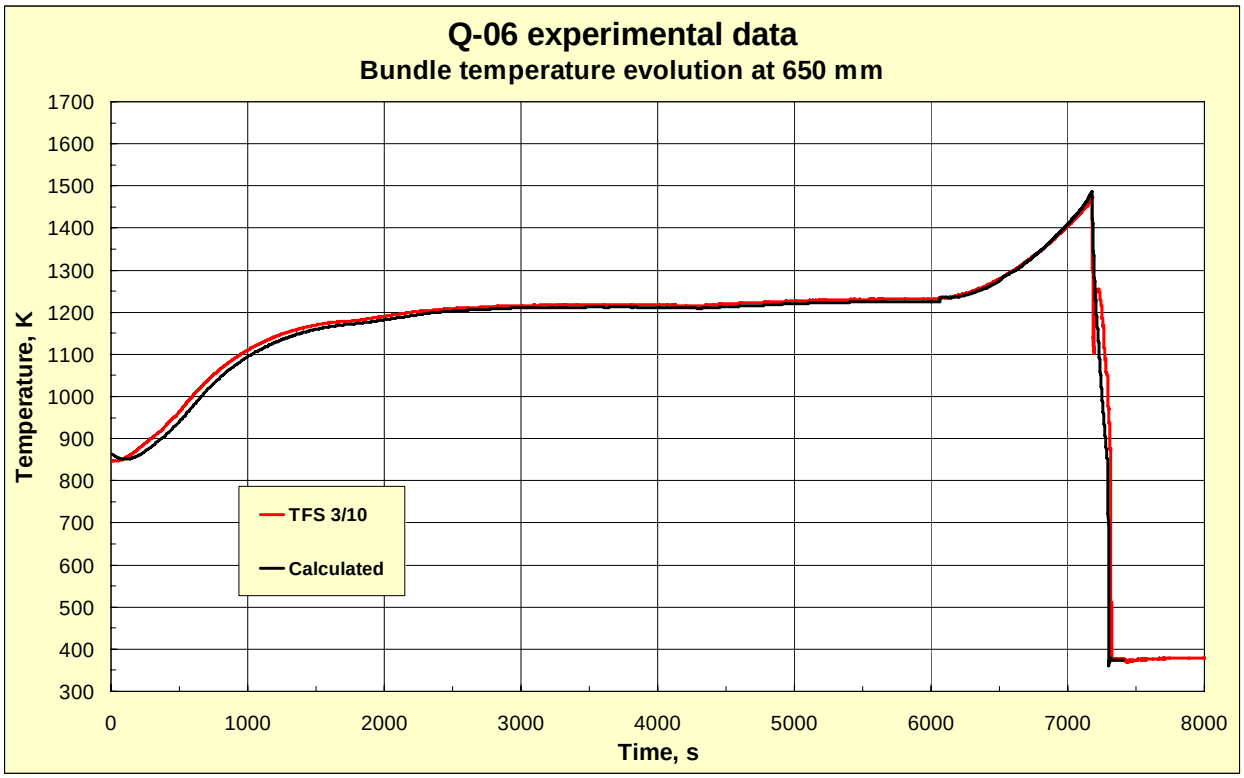

Fig 19. The experimentally measured temperatures at the elevation 650 mm: TFS 3/10 data (red line) and calculated temperature evolution of the central rod outer surface (black line)

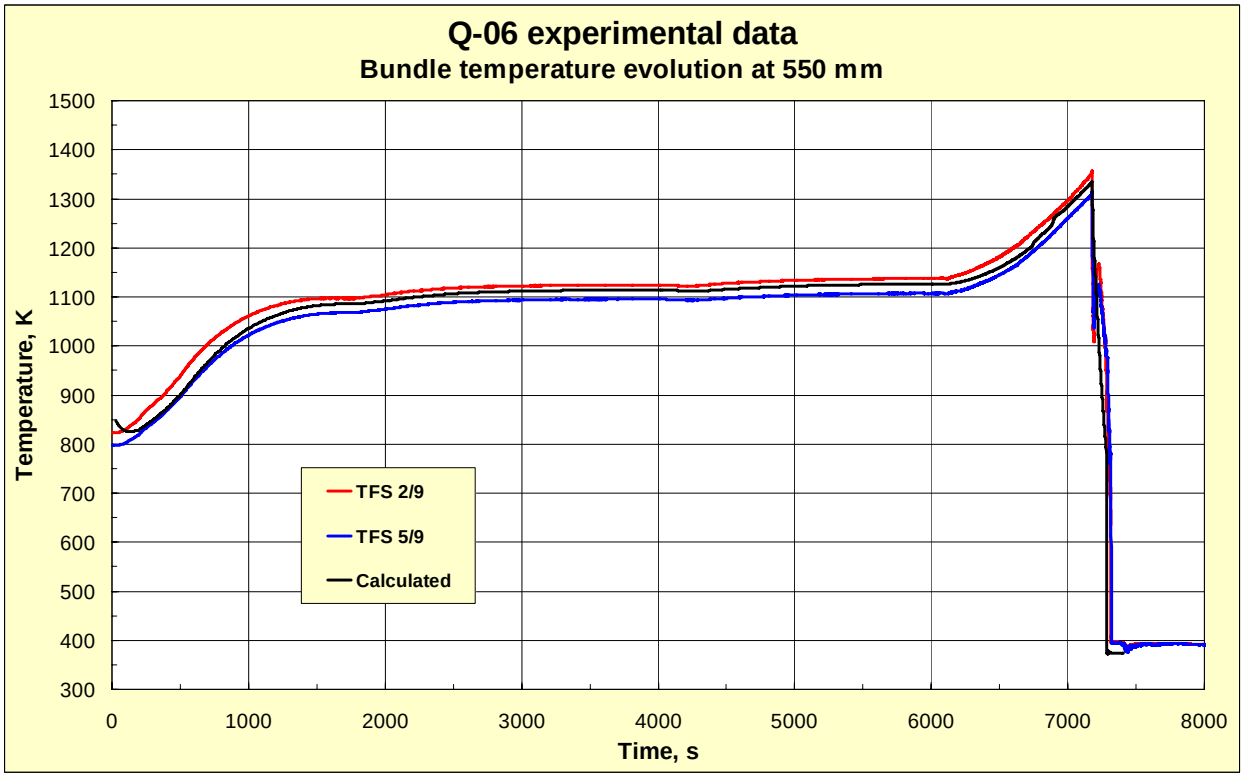

Fig 20. The experimentally measured temperatures at the elevation 550 mm: TFS2/9 data (red line) and TFS5/9 data (blue line) and calculated temperature evolution of the central rod outer surface (black line)

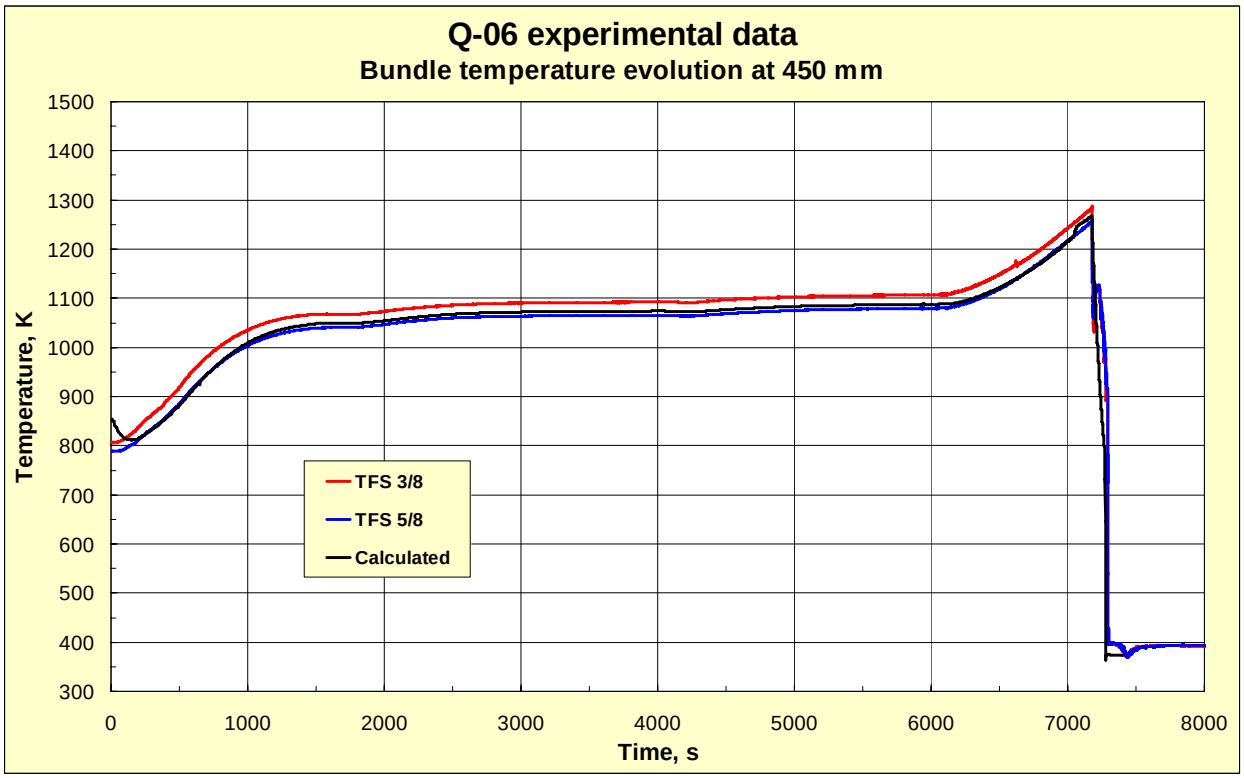

Fig 21. The experimentally measured temperatures at the elevation 450 mm: TFS3/8 data (red line) and TFS5/8 data (blue line) and calculated temperature evolution of the central rod outer surface (black line)

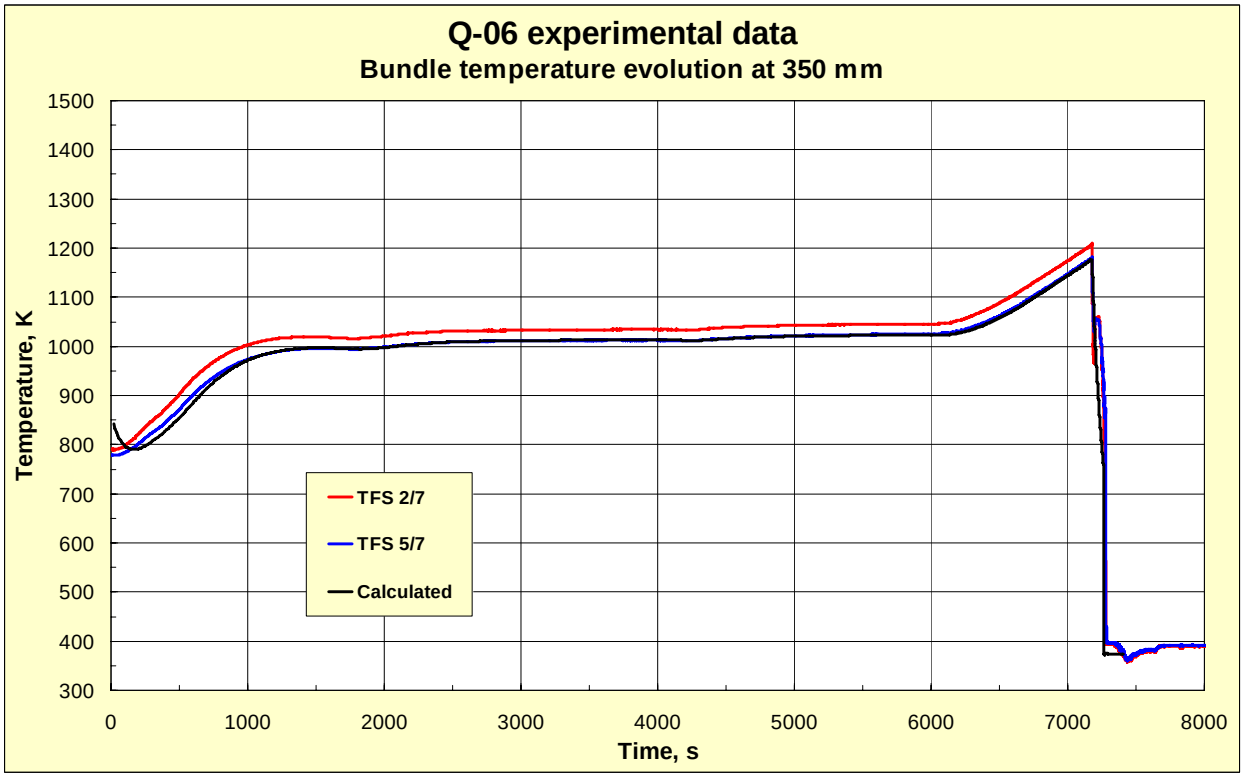

Fig 22. The experimentally measured temperatures at the elevation 350 mm: TFS2/7 data (red line) and TFS5/7 data (blue line) and calculated temperature evolution of the central rod outer surface (black line)

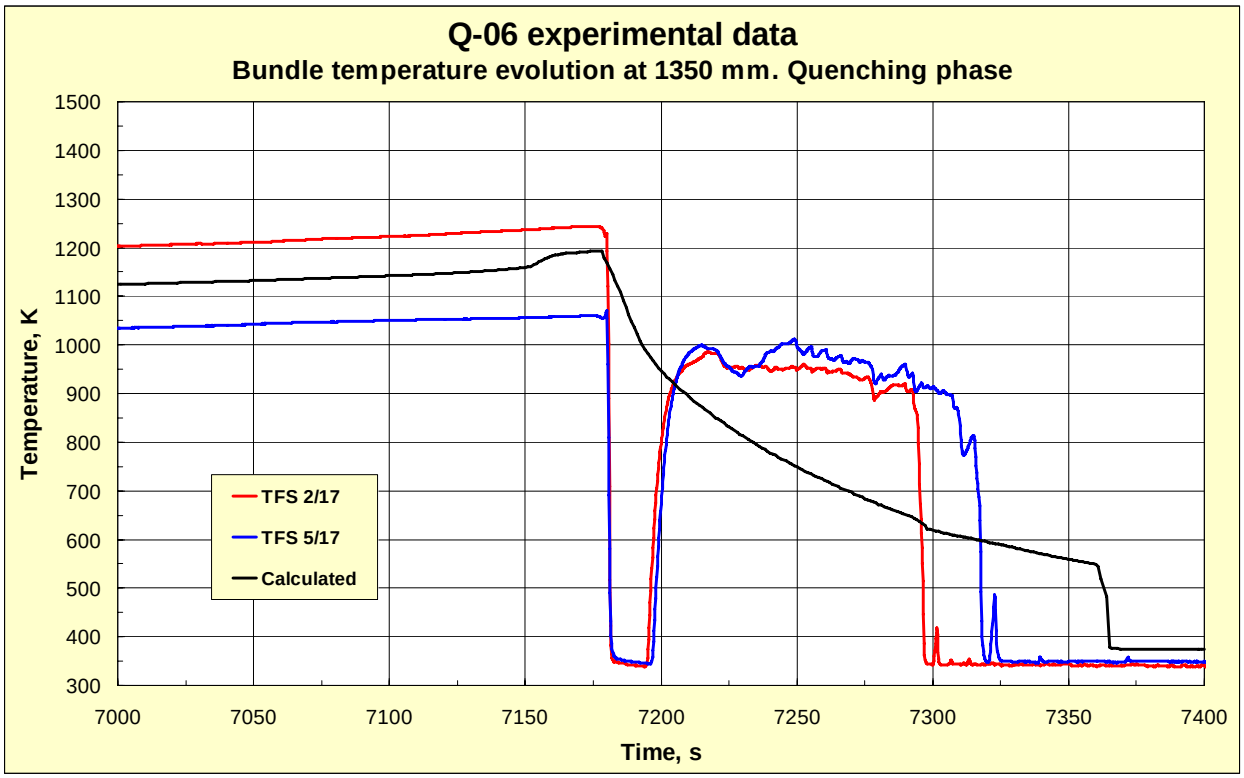

Fig 23. The experimentally measured temperatures at the elevation 1350 mm: TFS2/17 data (red line) and TFS5/17 data (blue line) and calculated temperature evolution of the central rod outer surface (black line). Quenching phase (time period 7000 – 7400 s)

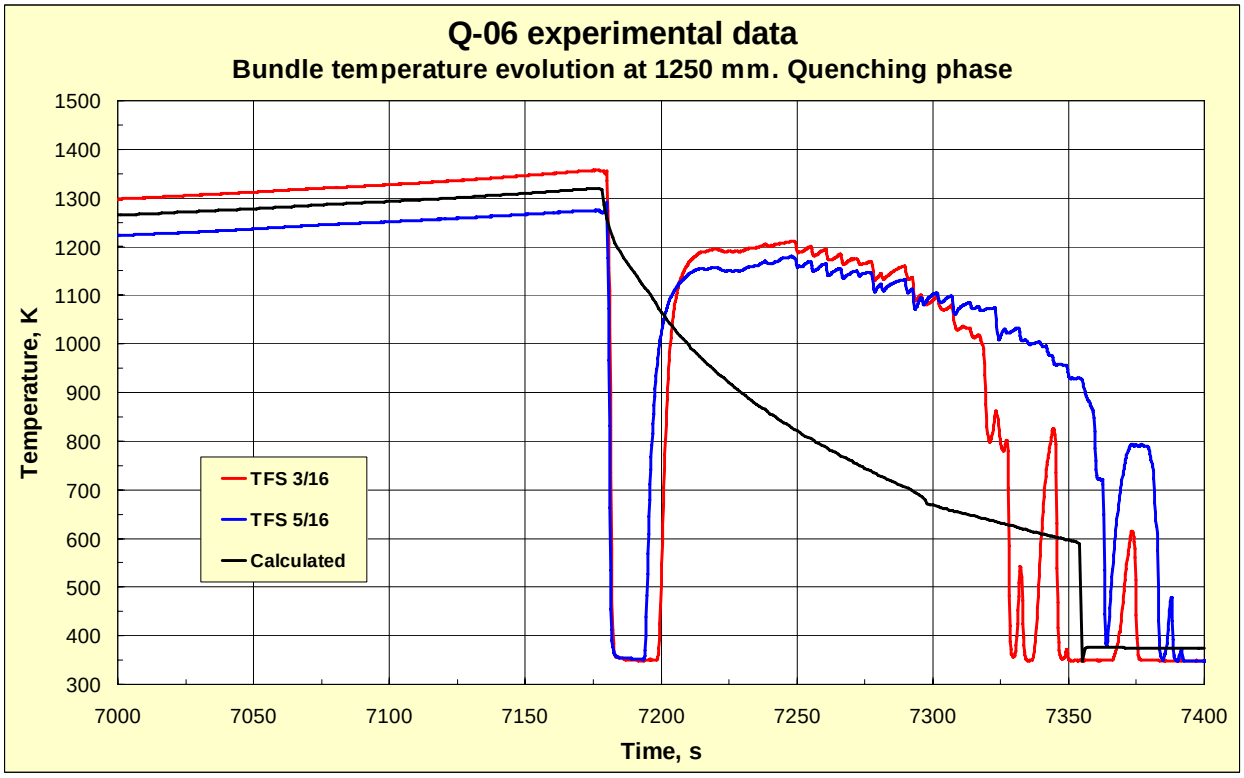

Fig 24. The experimentally measured temperatures at the elevation 1250 mm: TFS3/16 data (red line) and TFS5/16 data (blue line) and calculated temperature evolution of the central rod outer surface (black line). Quenching phase (time period 7000 – 7400 s)

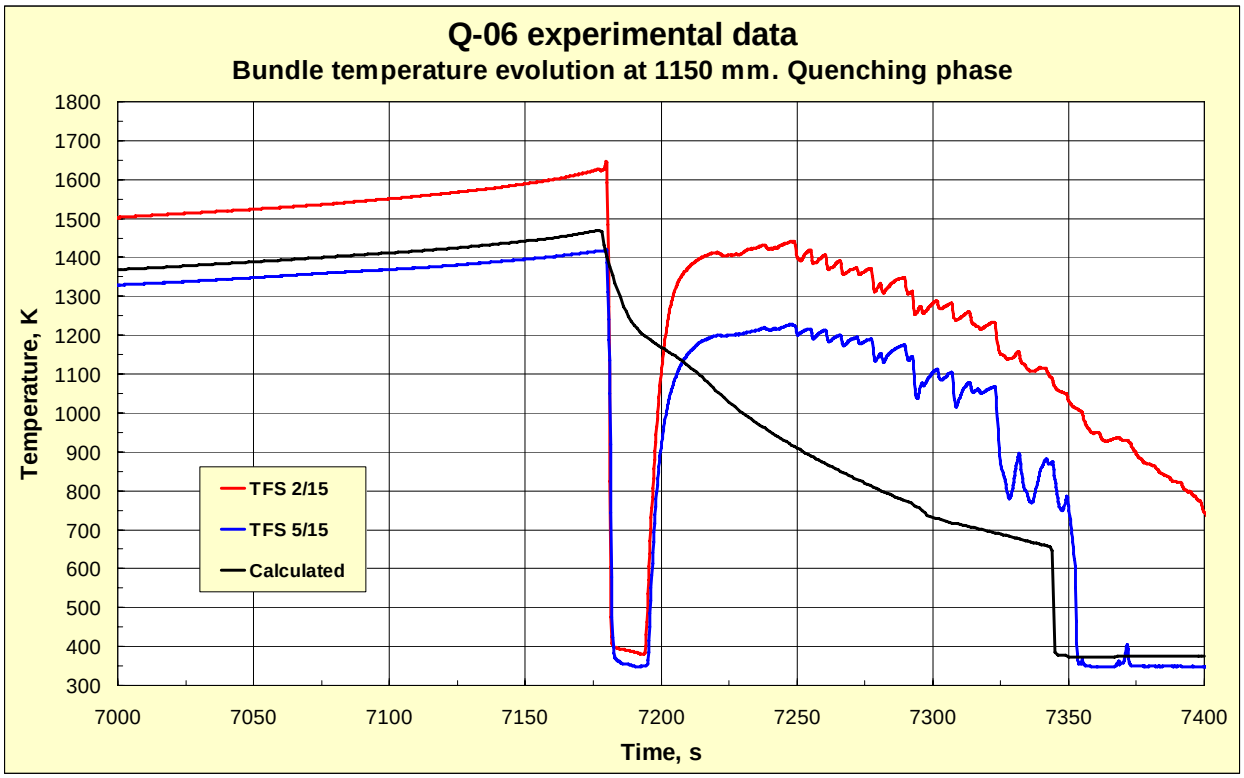

Fig 25. The experimentally measured temperatures at the elevation 1150 mm: TFS 2/15 data (red line) and TFS 5/15 data (blue line) and calculated temperature evolution of the central rod outer surface (black line). Quenching phase (time period 7000 – 7400 s)

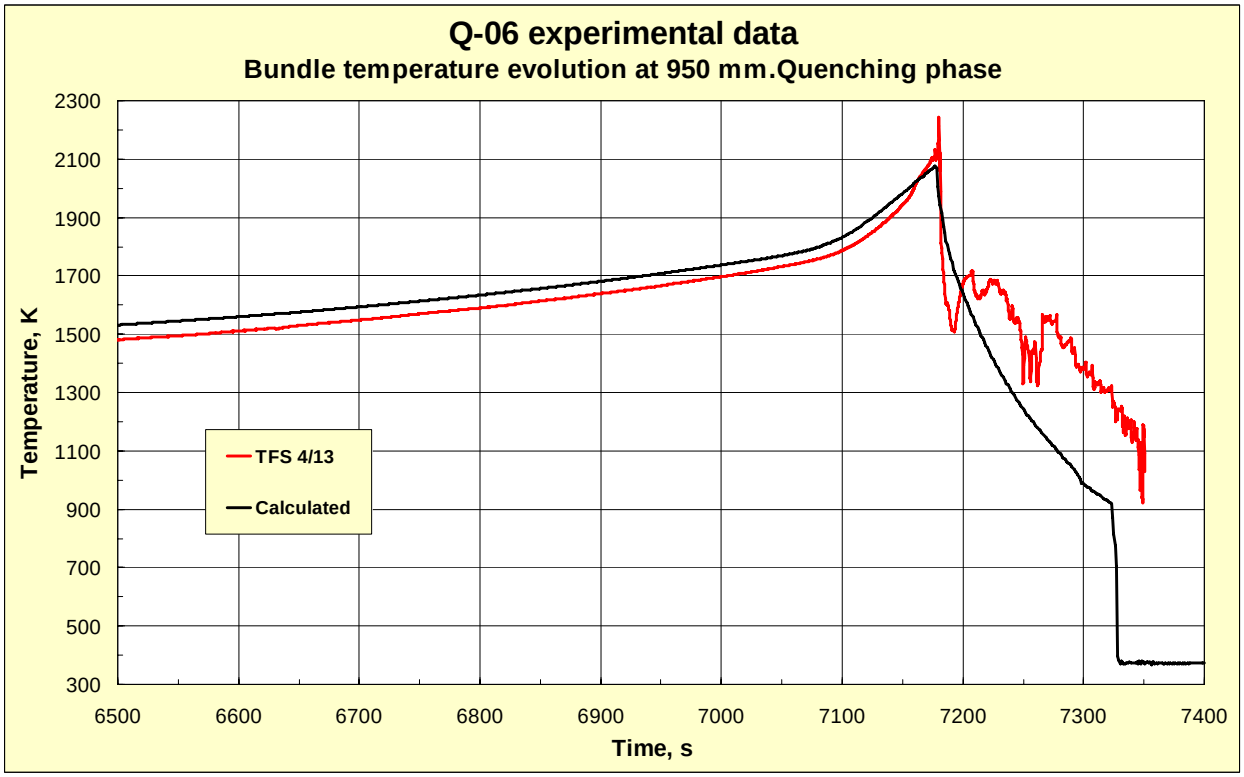

Fig 26. The experimentally measured temperatures at the elevation 950 mm: TFS 4/13 data (red line) and calculated temperature evolution of the central rod outer surface (black line). Transient and quenching phase (time period 6500 – 7400 s)

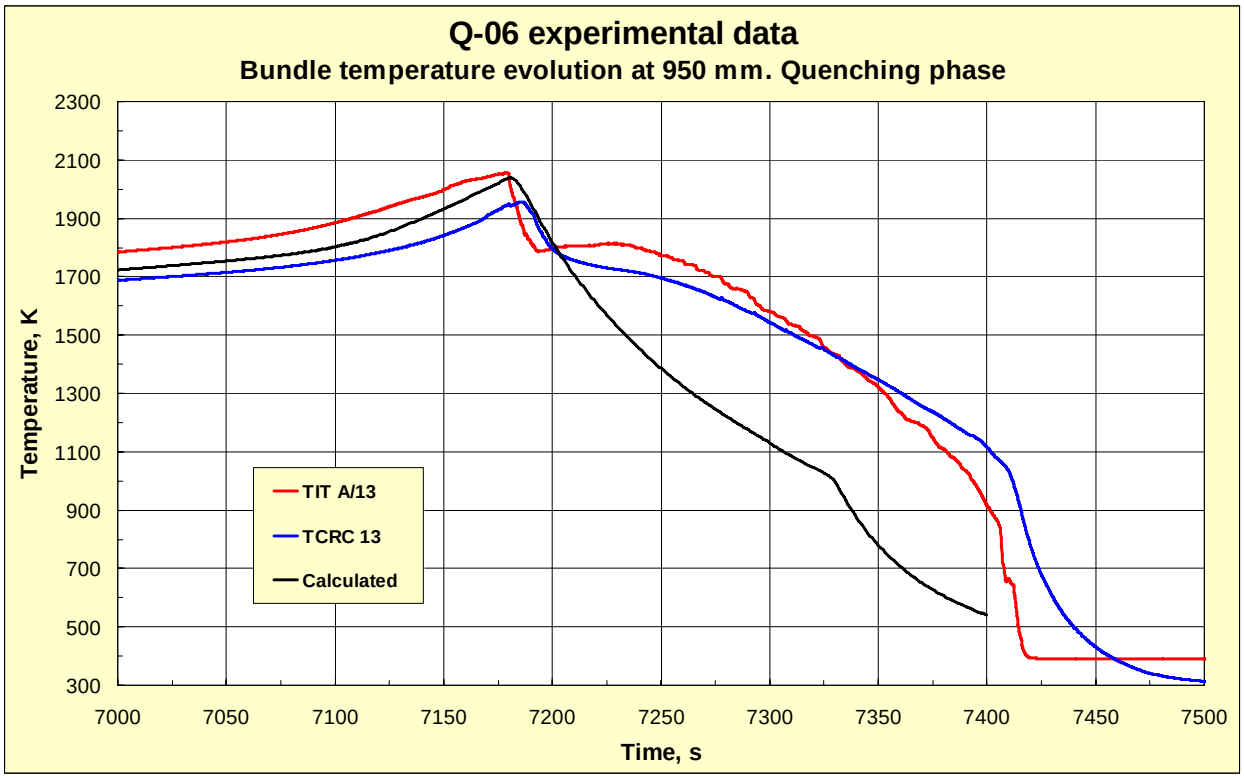

Fig 27. The experimentally measured temperatures at the elevation 950 mm: TIT A/13 data (red line), TCRC 13 data (blue line) and calculated temperature evolution central rod pellet's centre (black line). Transient and quenching phase (time period 7000 – 7500 s)

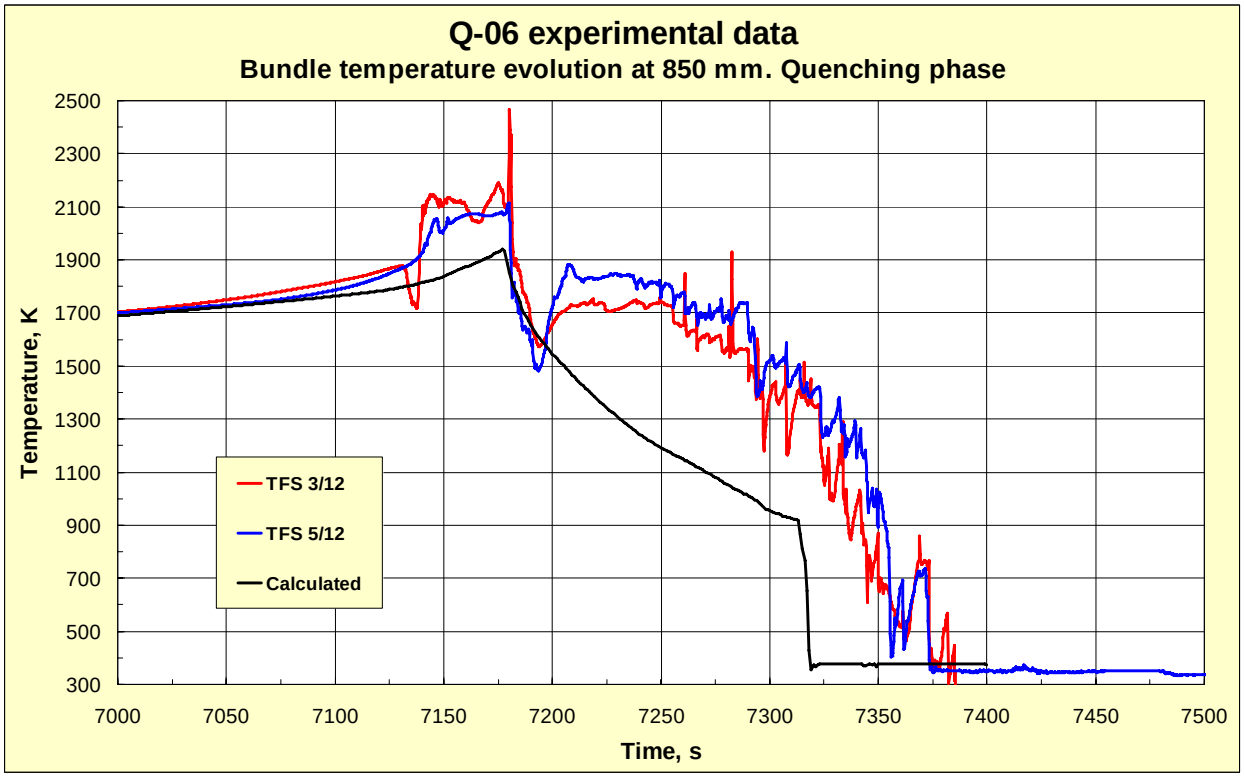

Fig 28. The experimentally measured temperatures at the elevation 850 mm: TFS 3/12 data (red line), TFS 5/12 data (blue line) and calculated temperature evolution of the central rod outer surface (black line). Transient and quenching phase (time period 7000 – 7500 s)

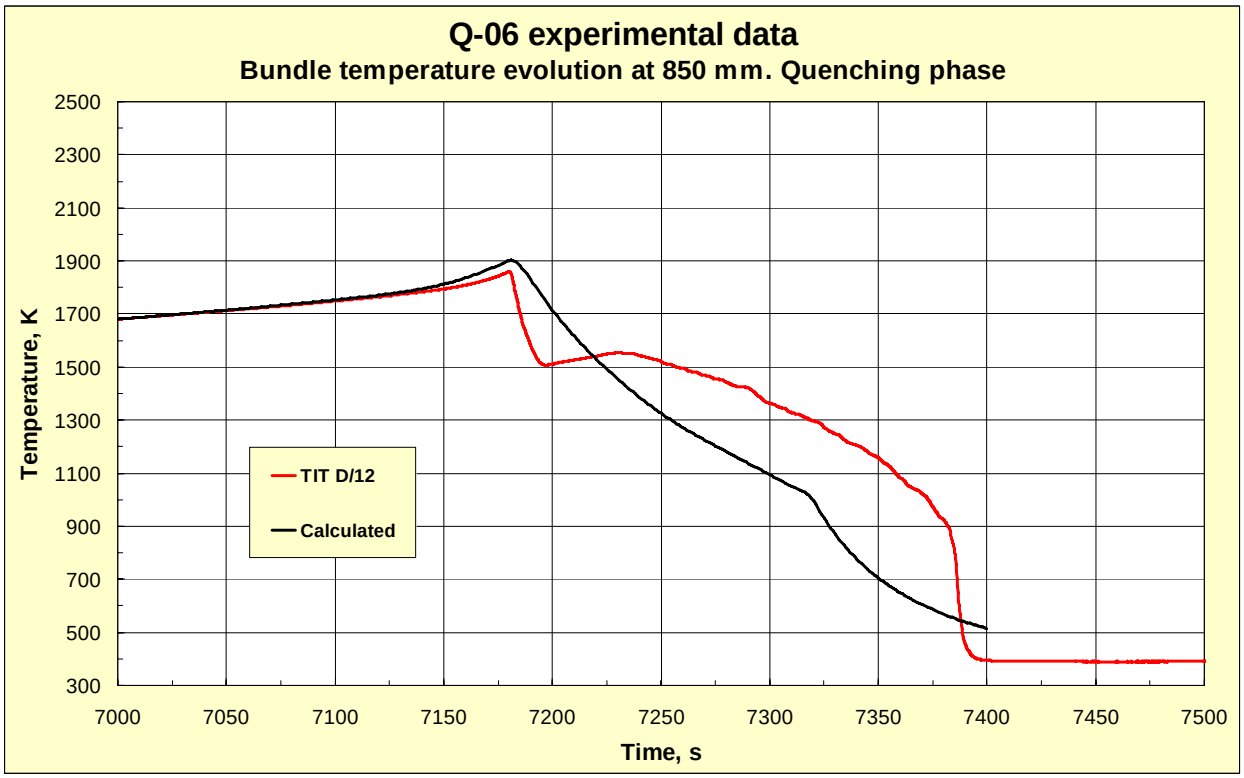

Fig 29. The experimentally measured temperature at the elevation 850 mm: TIT D/12 data (red line) and calculated temperature evolution of the central rod pellet's centre (black line). Transient and quenching phase (time period 7000 – 7500 s)

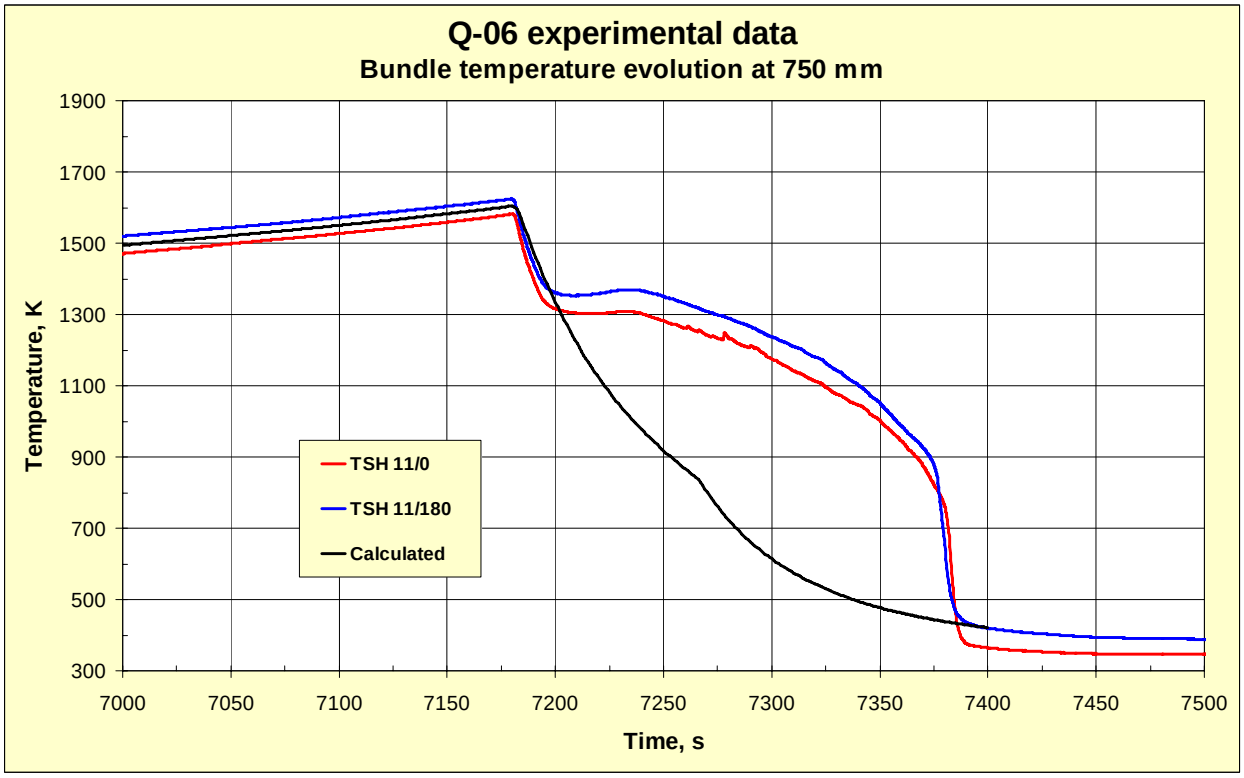

Fig 30. The experimentally measured temperatures at the elevation 750 mm: TSH 11/0 data (red line), TSH 11/180 data (blue line) and calculated temperature evolution of the central rod pellet's centre (black line). Transient and quenching phase (time period 7000 – 7500 s)

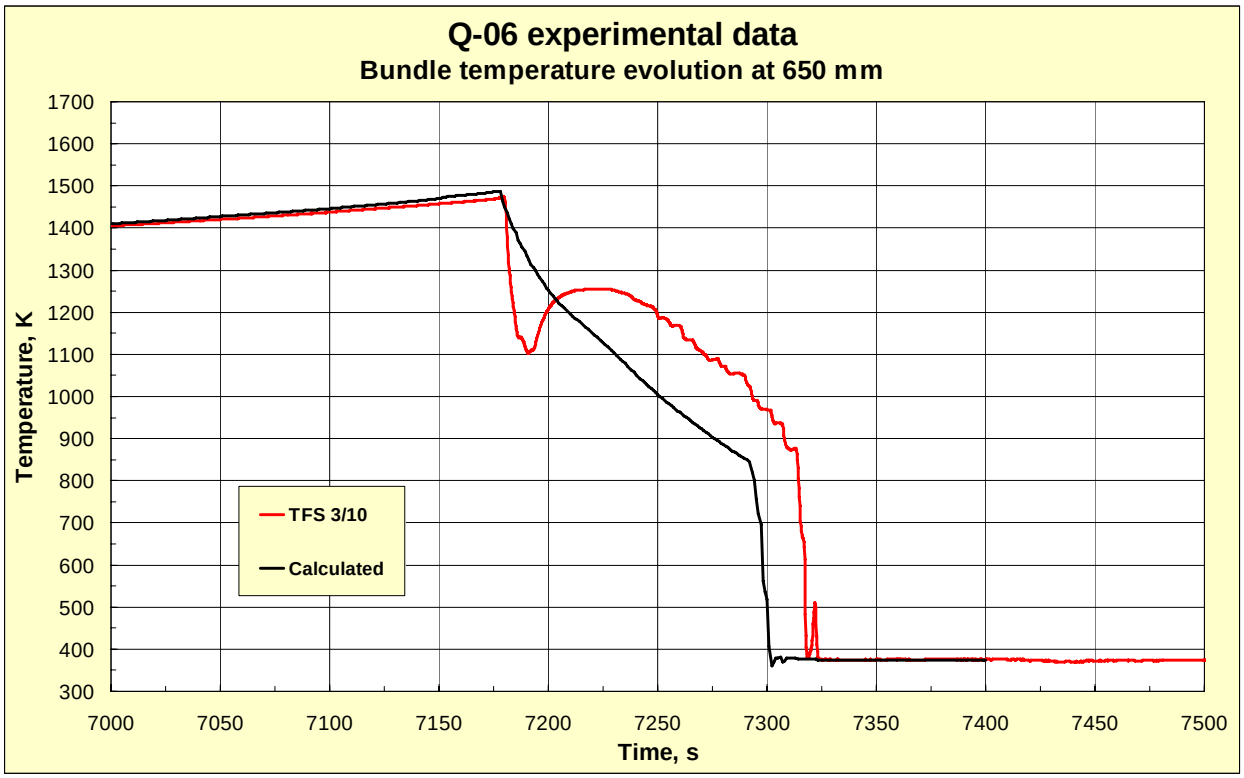

Fig 31. The experimentally measured temperature at the elevation 650 mm: TFS 3/10 data (red line) and calculated temperature evolution of the central rod outer surface (black line). Transient and quenching phase (time period 7000 – 7500 s)

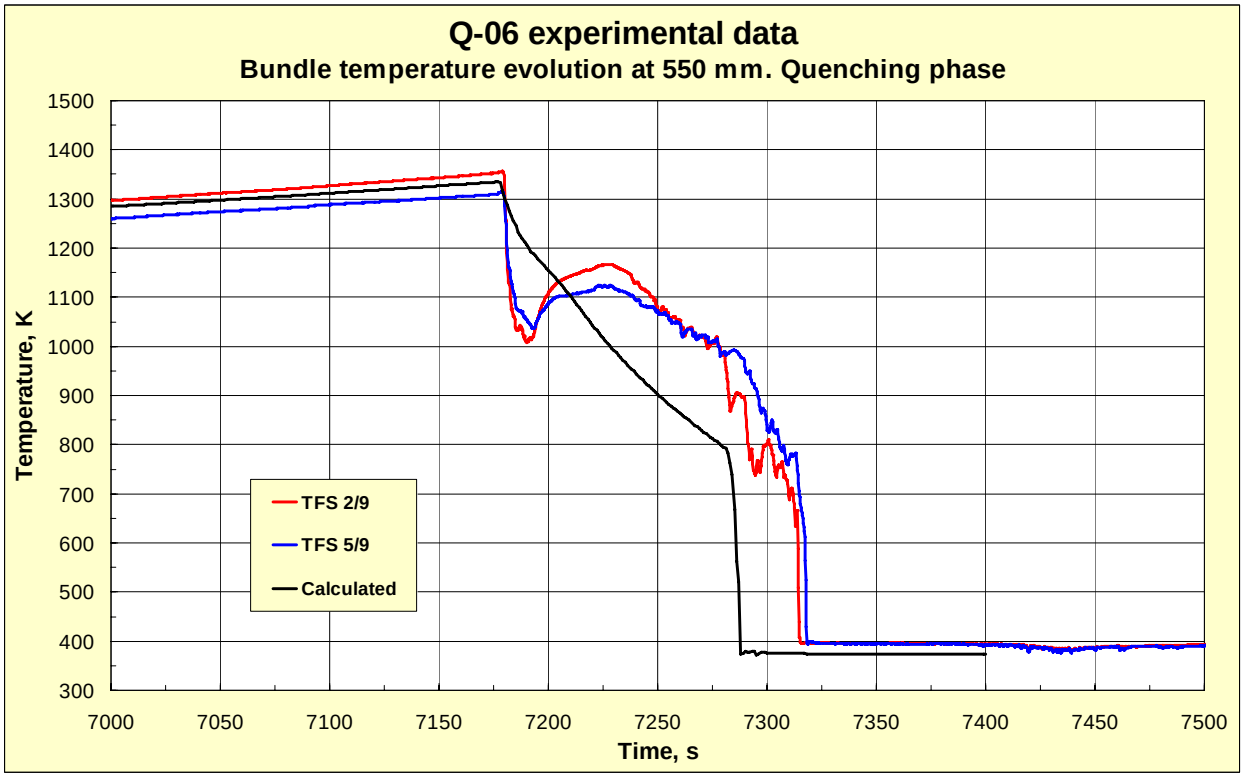

Fig 32. The experimentally measured temperatures at the elevation 550 mm: TFS 2/9 data (red line), TFS 5/9 data (blue line) and calculated temperature evolution of the central rod outer surface (black line). Transient and quenching phase (time period 7000 – 7500 s)

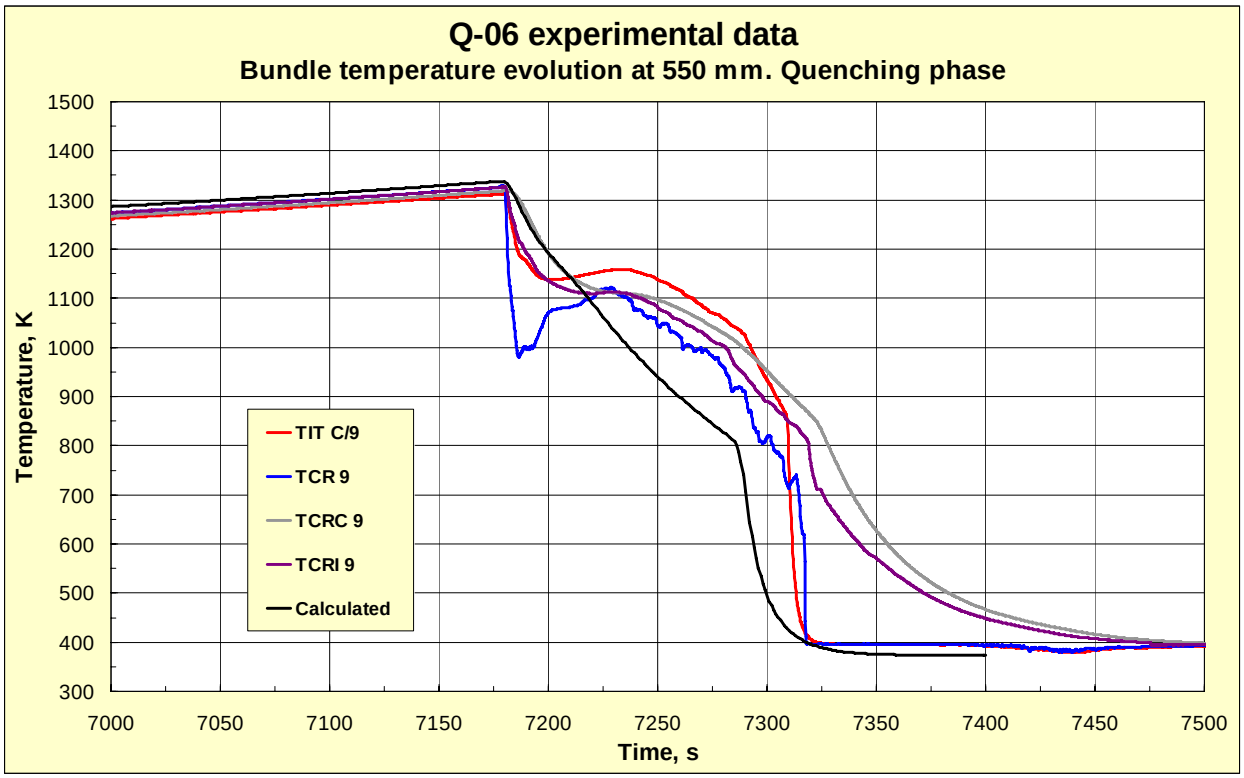

Fig 33. The experimentally measured temperature at the elevation 550 mm: TIT C/9 data (red line), TCR 9 data (blue line), TCRC 9 data (grey line), TCRI 9 data (violet line) and calculated temperature evolution of the central rod pellet's centre (black line). Transient and quenching phase (time period 7000 – 7500 s)

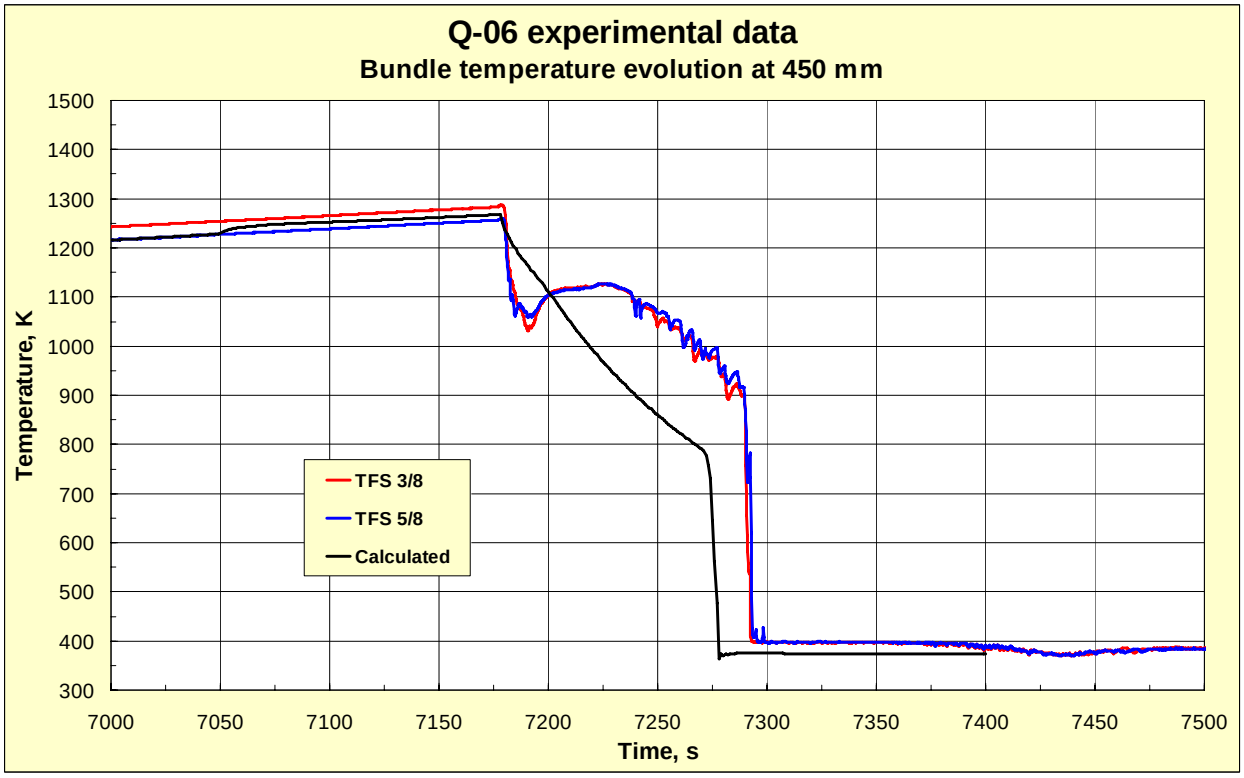

Fig 34. The experimentally measured temperatures at the elevation 450 mm: TFS 3/8 data (red line), TFS 5/8 data (blue line) and calculated temperature evolution of the central rod outer surface (black line). Transient and quenching phase (time period 7000 – 7500 s)

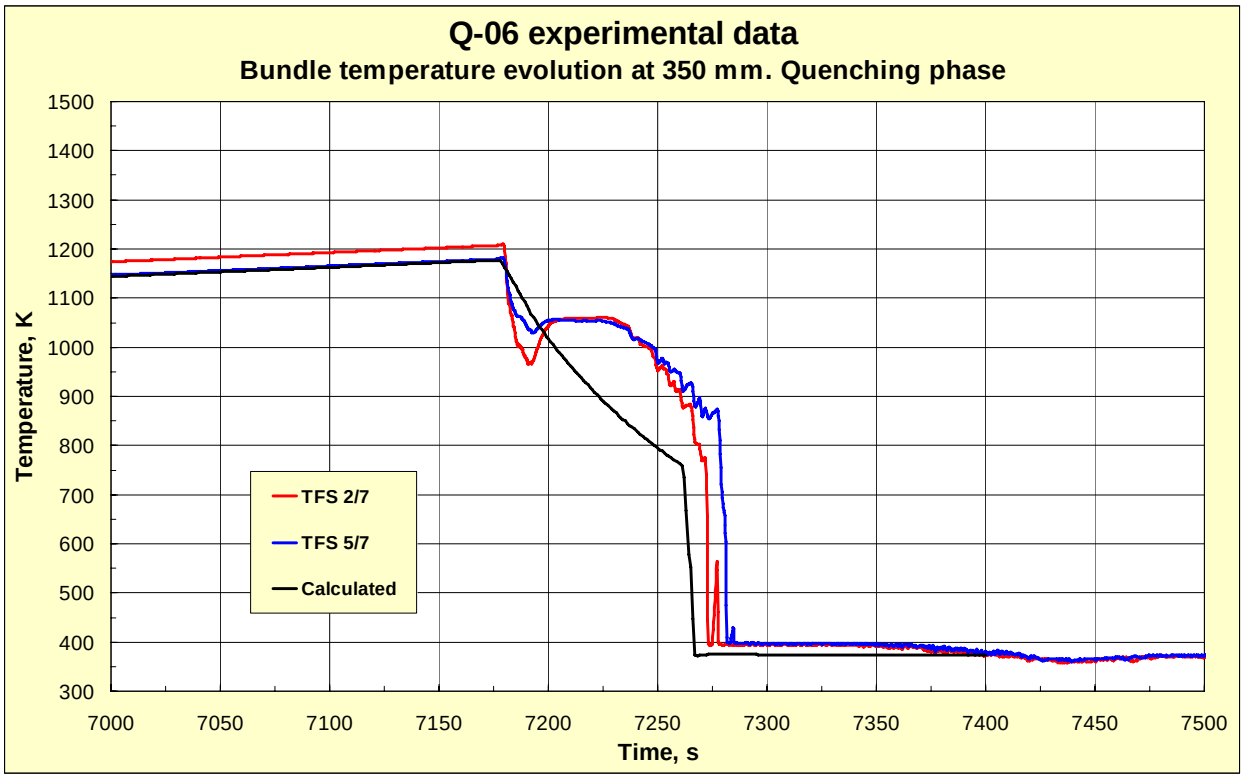

Fig 35. The experimentally measured temperatures at the elevation 350 mm: TFS 2/7 data (red line), TFS 5/7 data (blue line) and calculated temperature evolution of the central rod outer surface (black line). Transient and quenching phase (time period 7000 – 7500 s)

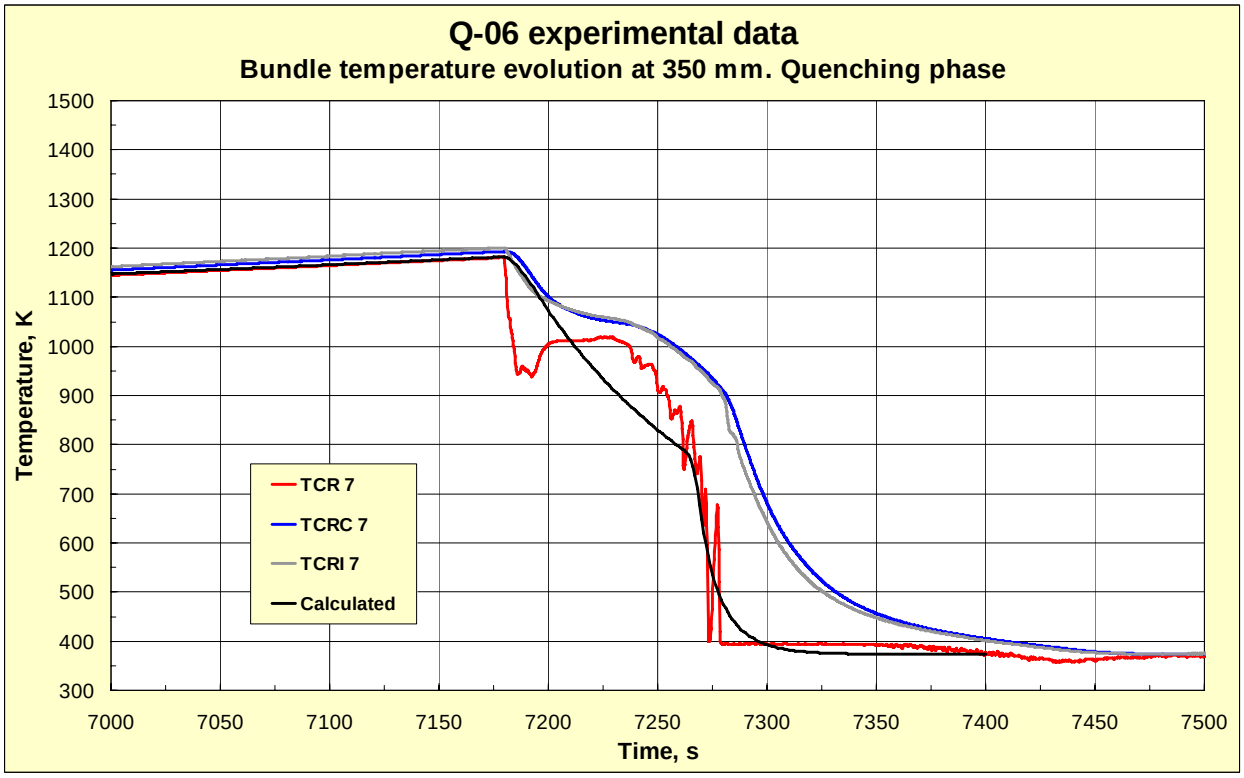

Fig 36. The experimentally measured temperature at the elevation 350 mm: TCR 7 data (red line), TCRC 7 data (blue line), TCRI 7 data (grey line) and calculated temperature evolution of the central rod pellet's centre (black line). Transient and quenching phase (time period 7000 – 7500 s)

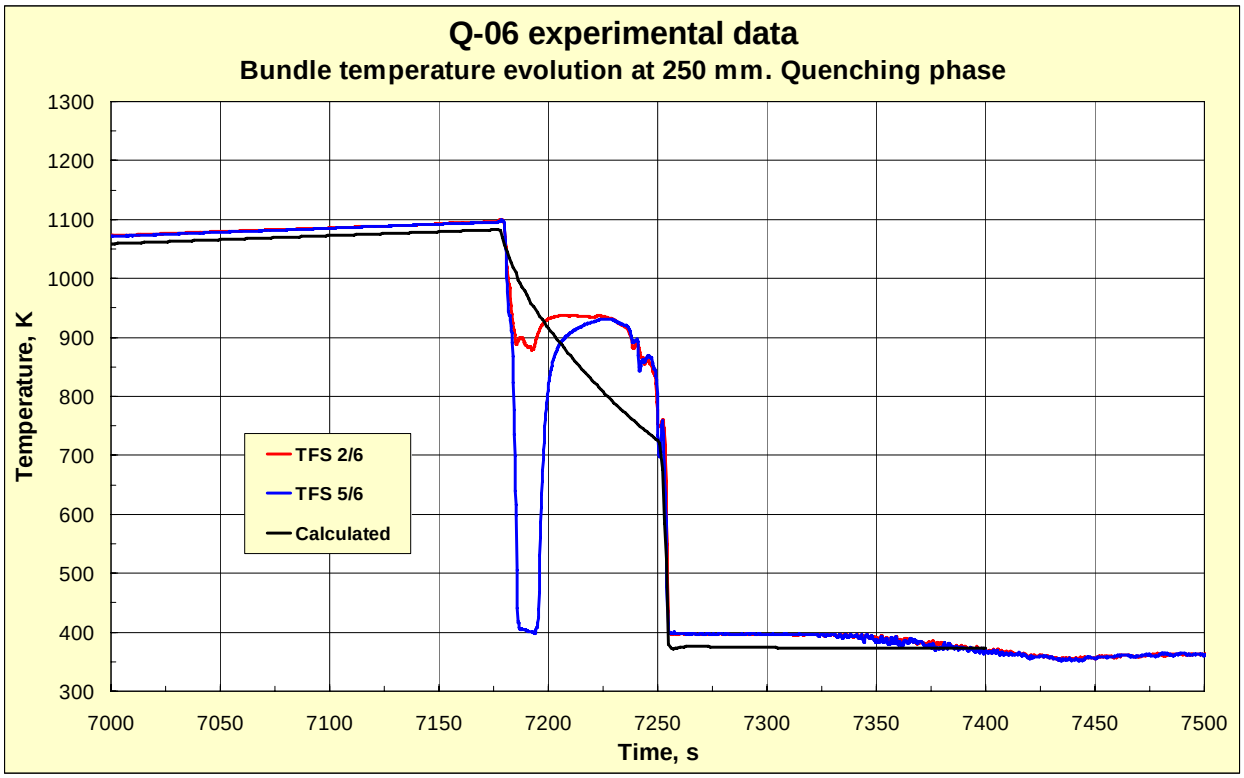

Fig 37. The experimentally measured temperatures at the elevation 250 mm: TFS 2/6 data (red line), TFS 5/6 data (blue line) and calculated temperature evolution of the central rod outer surface (black line). Transient and quenching phase (time period 7000 – 7500 s)

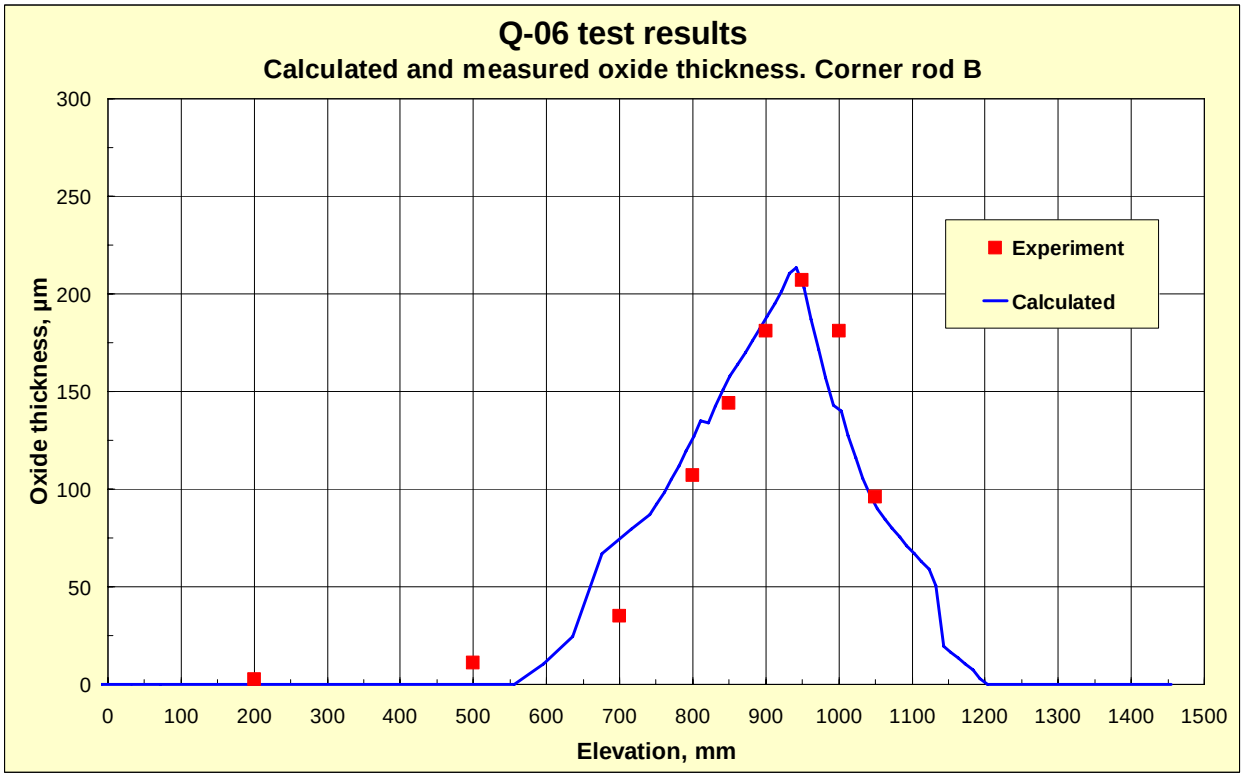

Fig 38. Oxide layer thickness axial profile of corner rod B (withdrawn from the test bundle at 6620 s) compared to the calculated one of the central rod for the same time

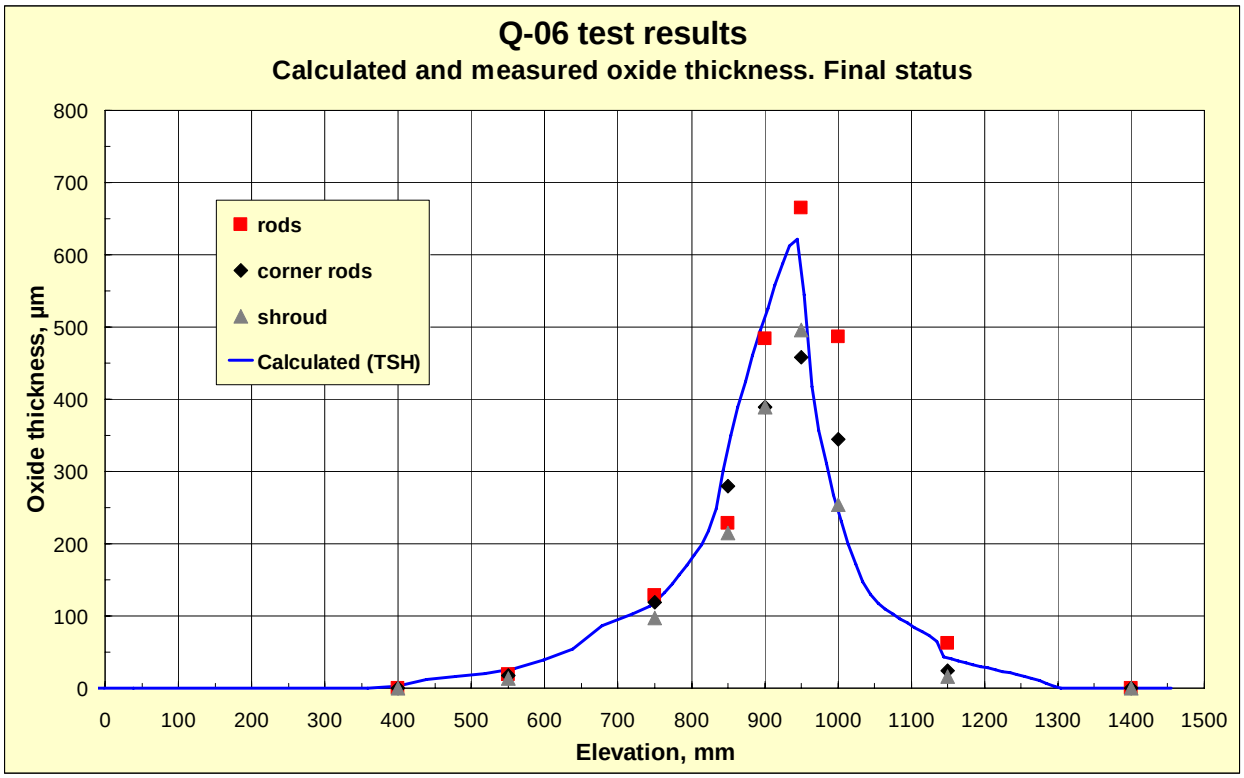

Fig 39. Measured oxide layer thickness axial profiles of heated rods (average), corner rods and shroud at the end of the test compared to the calculated oxide layer profile of the central rod (final state). The shroud thermocouples at 750 mm were used as the basis for the average channel temperature

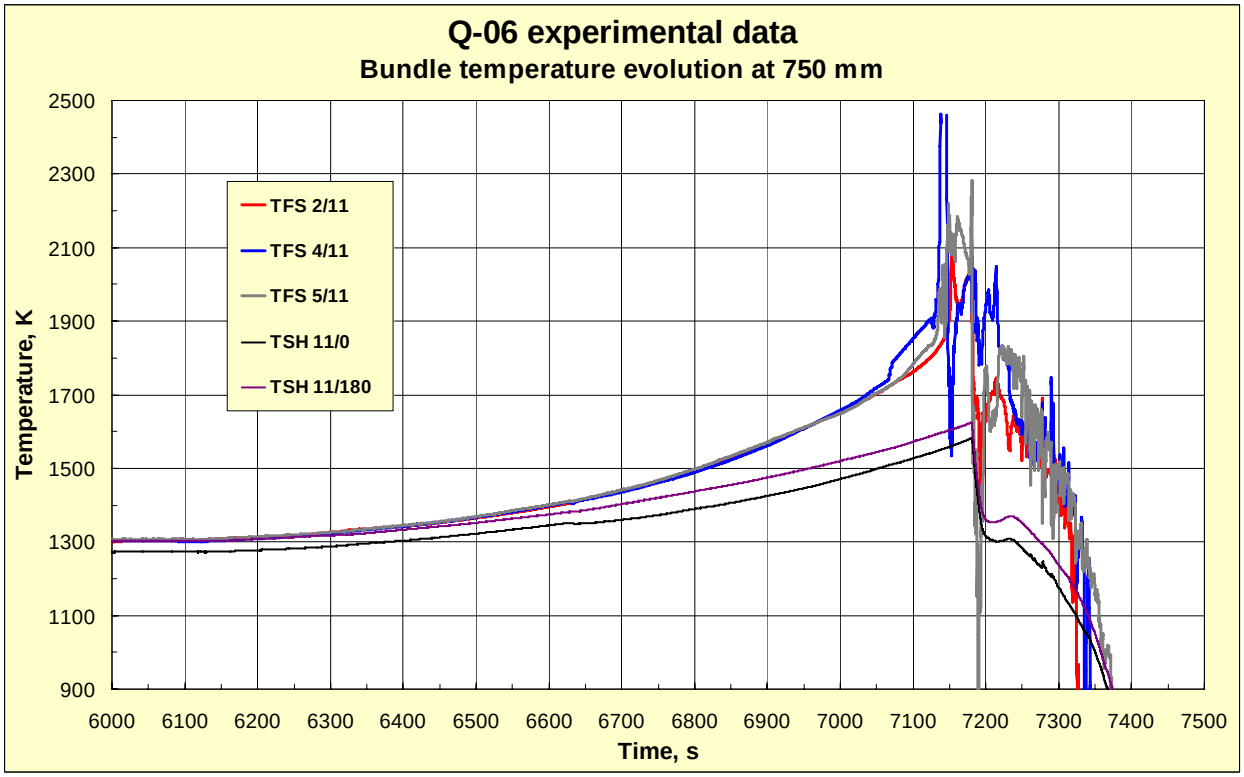

Fig 40. Measured temperature evolution at 750 mm. Readings of rod thermocouples TFS 2/11, TFS 4/11 and TFS 5/11 and shroud thermocouples TSH 11/0 and TSH 11/180

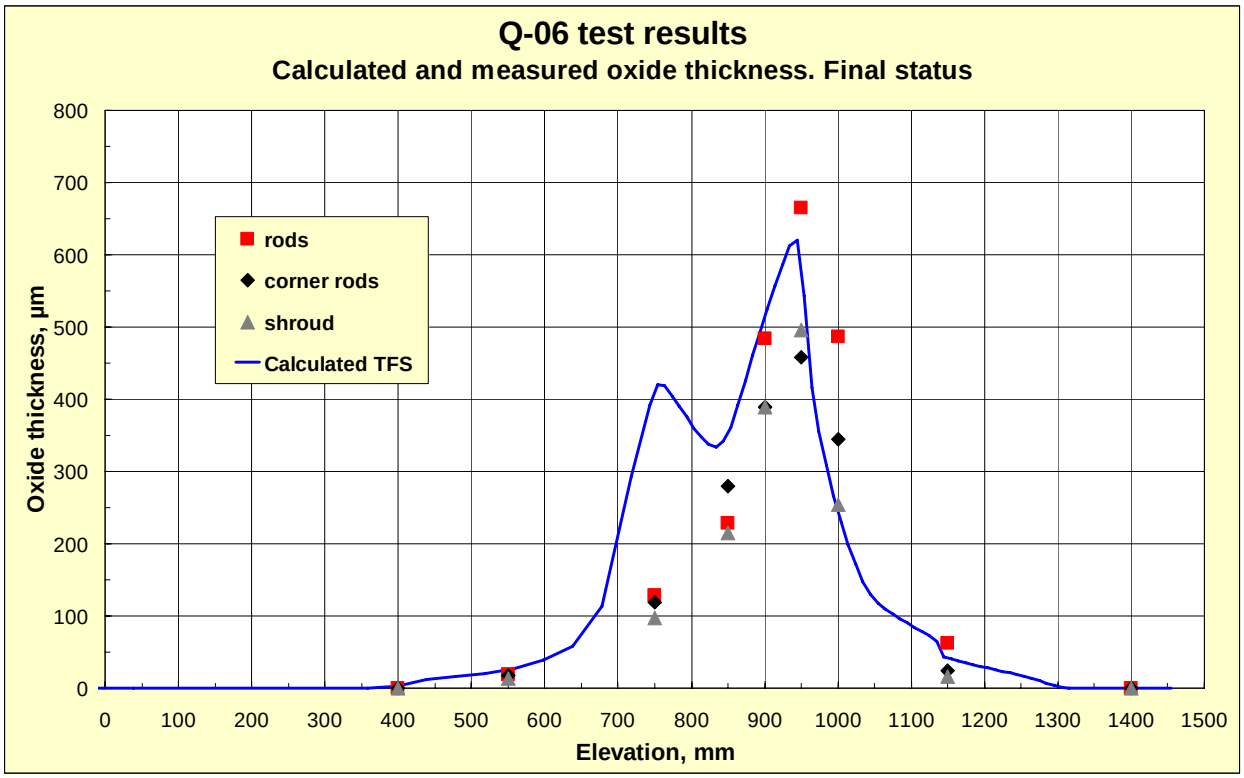

Fig 41. Measured oxide layer thickness axial profiles of heated rods (average), corner rods and shroud at the end of the test compared to the calculated oxide layer profile of the central rod (final state). The rod thermocouples at 750 mm were used as the basis for the average channel temperature

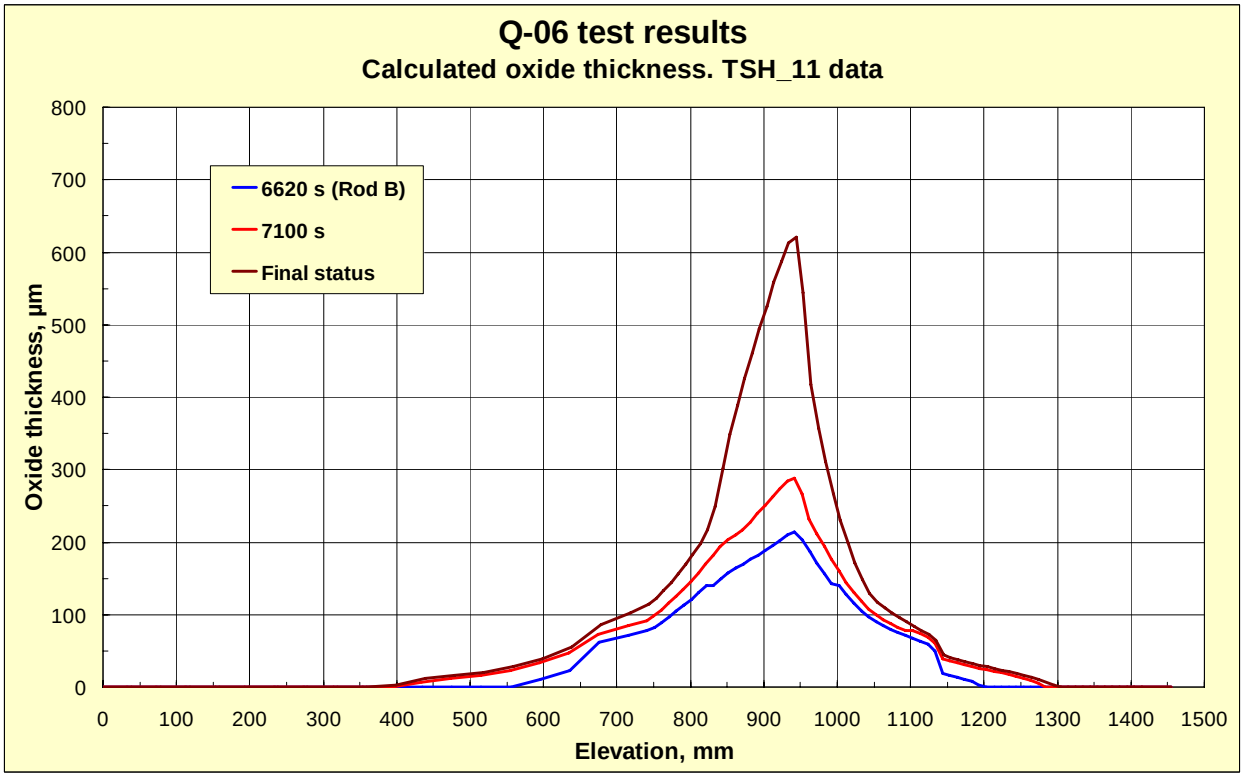

Fig 42. Calculated oxide axial profiles at 6620 s, 7100 s (beginning of temperature escalation) and at the end of the test

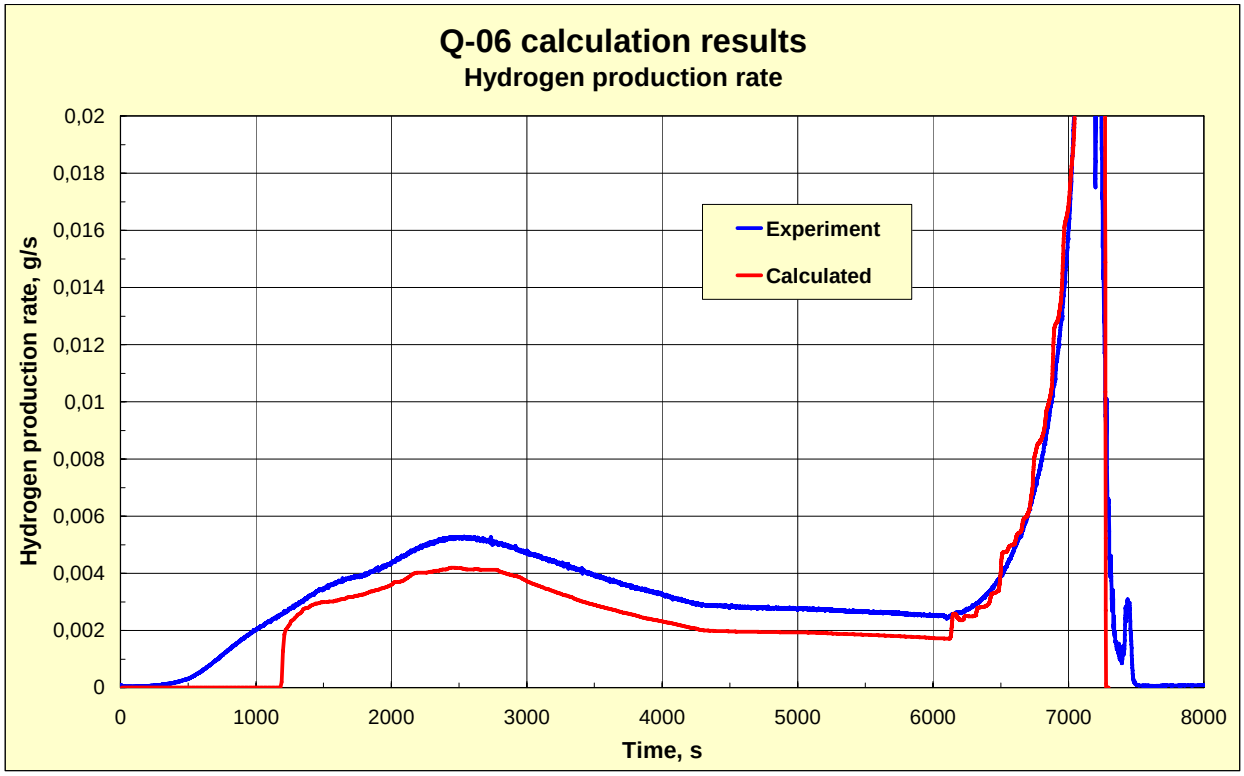

Fig 43. Experimentally measured and calculated hydrogen production rate

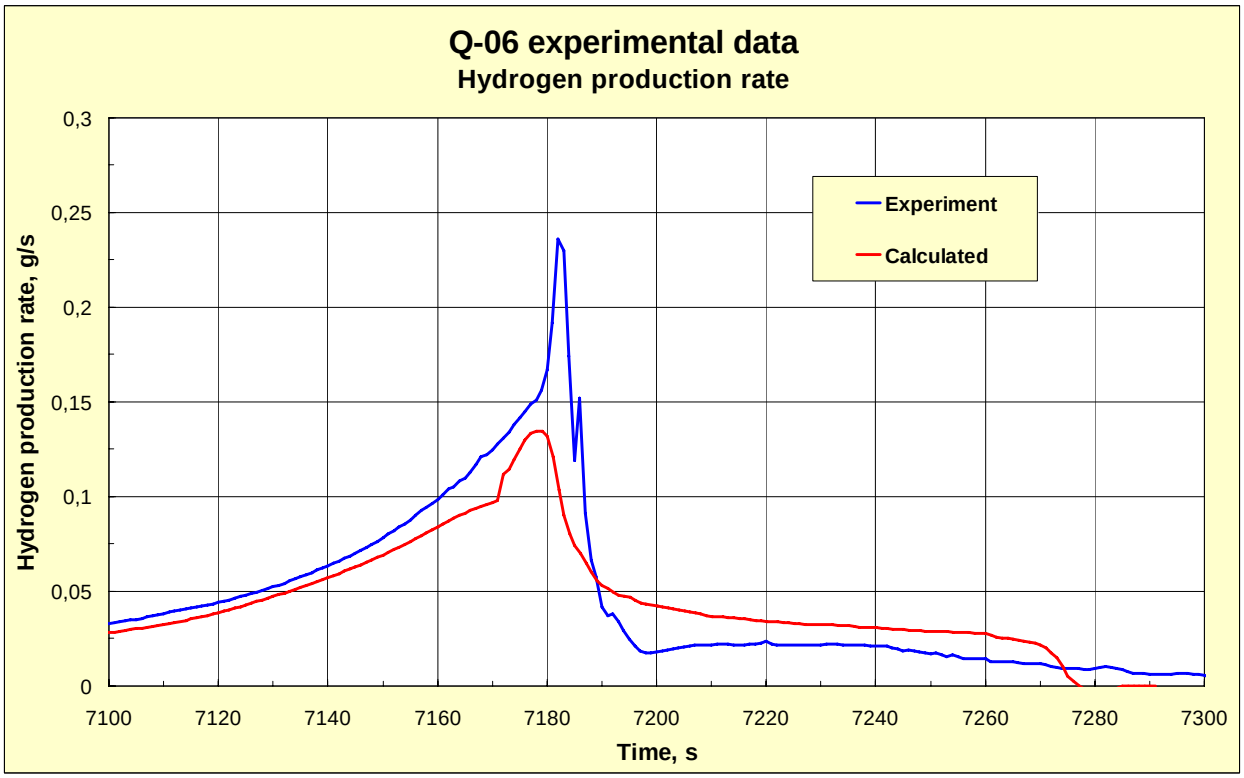

Fig 44. Experimentally measured and calculated hydrogen production rate. Temperature escalation and quenching phases of the test

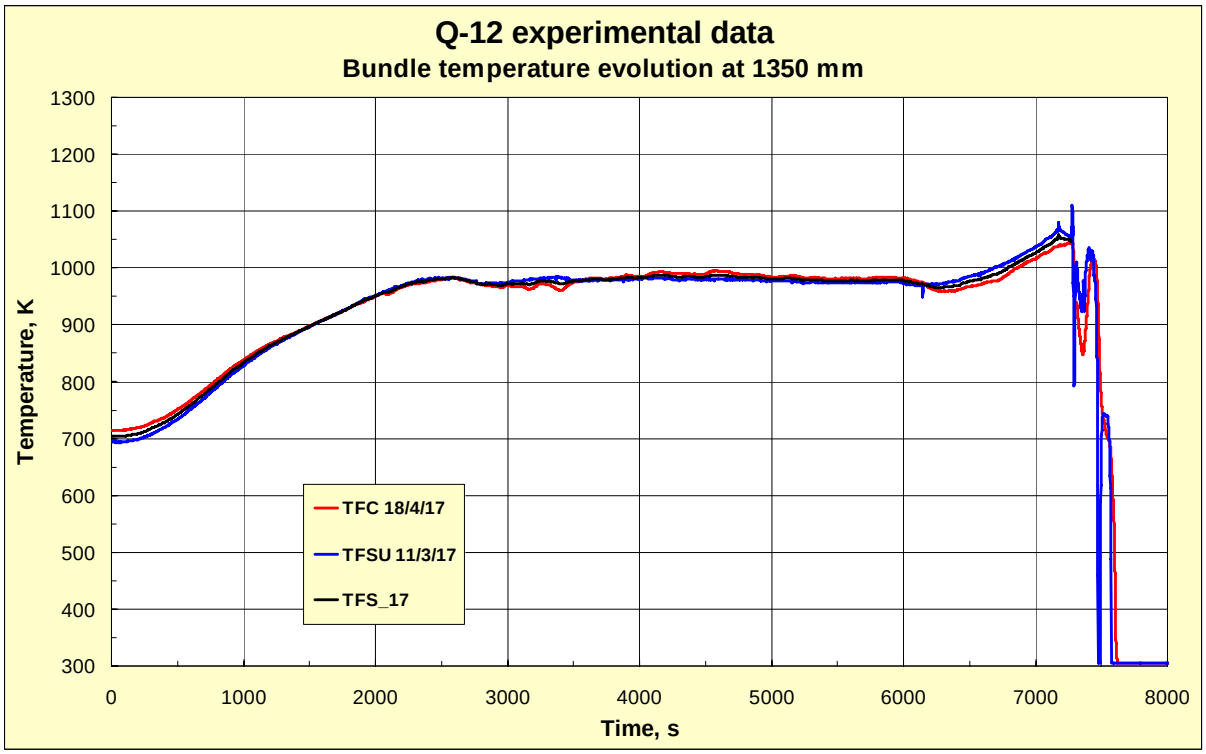

Fig 45. Bundle temperature evolution at the elevation 1350 mm measured by thermocouples TFC 18/4/17 (red line), TFSU 11/3/17 (blue line) and averaged temperature used in the calculations (black line)

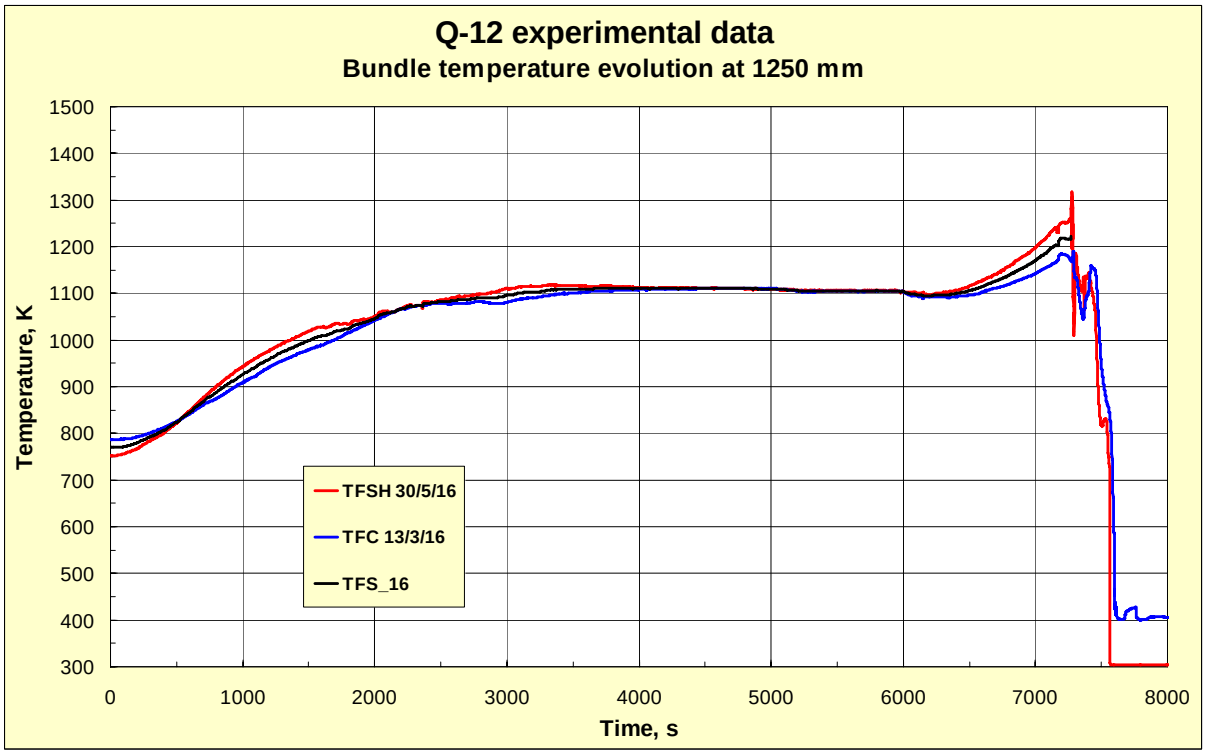

Fig 46. Bundle temperature evolution at the elevation 1250 mm measured by thermocouples TFSH 30/5/16 (red line), TFC 13/3/16 (blue line) and averaged temperature used in the calculations (black line)

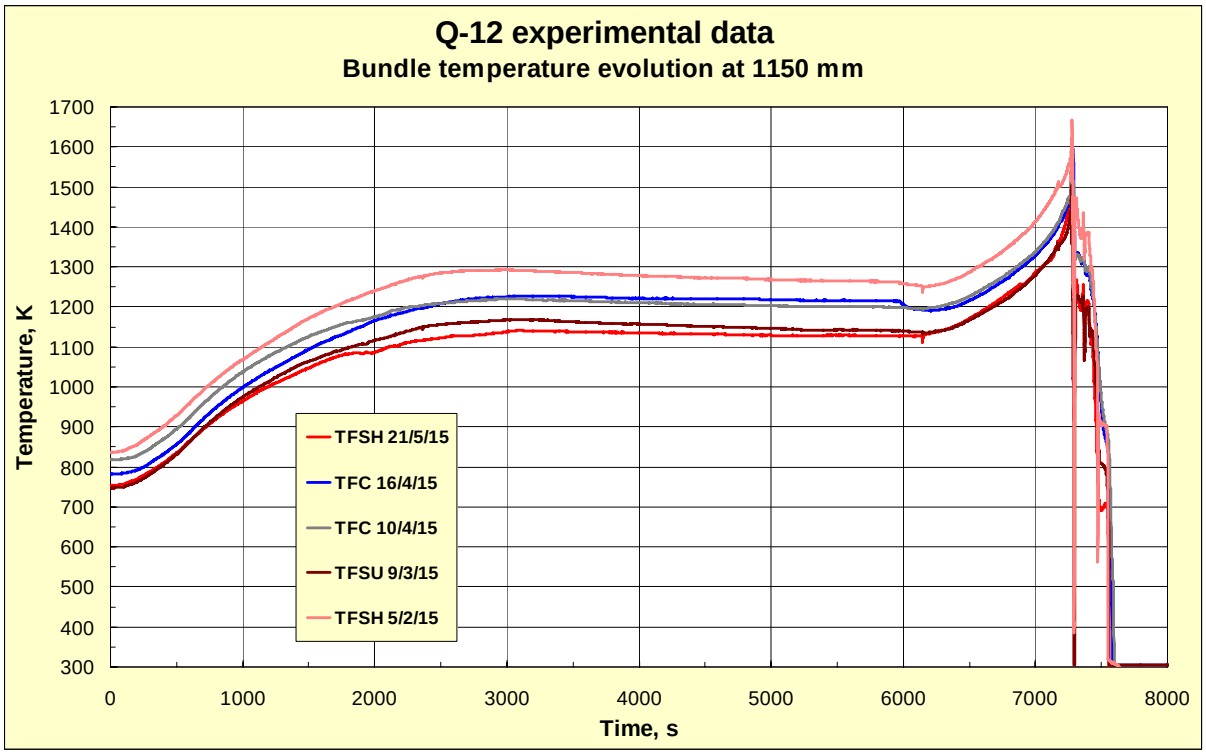

Fig 47. Bundle temperature evolution at the elevation 1150 mm measured by TFSH/TFC/TFSU thermocouples

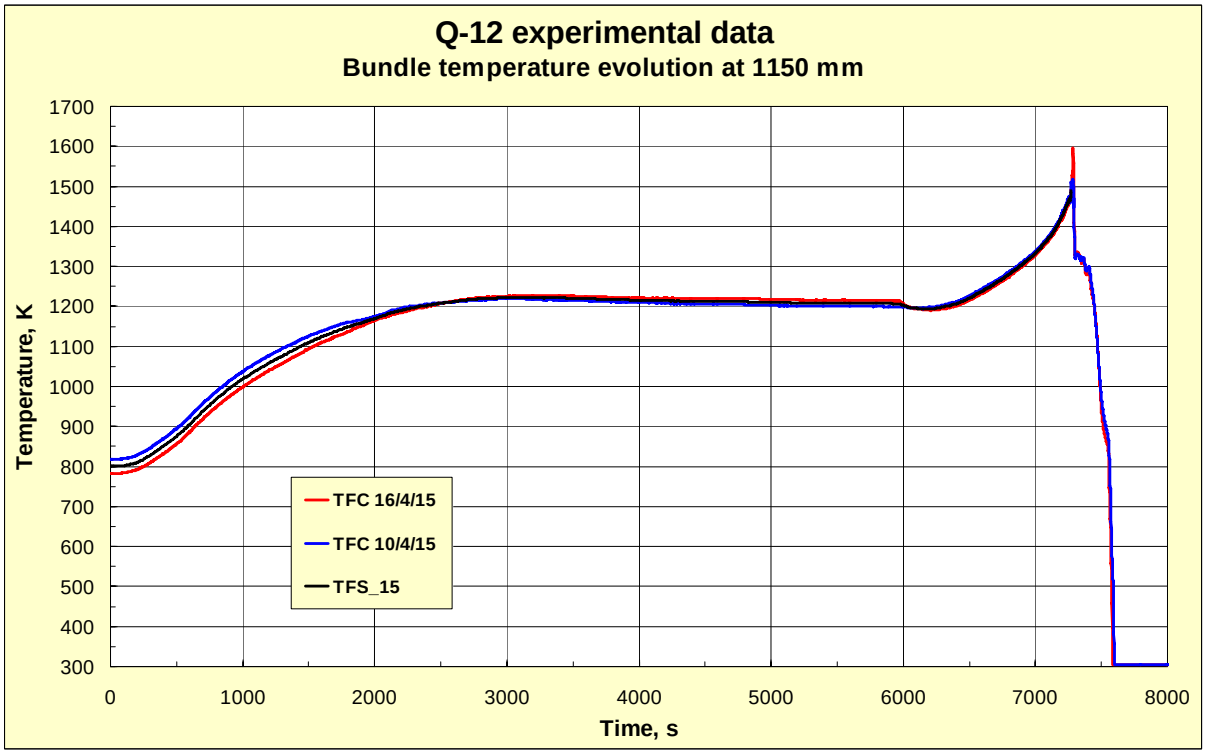

Fig 48. Bundle temperature evolution at the elevation 1150 mm measured by TFC 16/4/15 (red line), TFC 10/4/15 (blue line) and averaged temperature used in the calculations (black line)

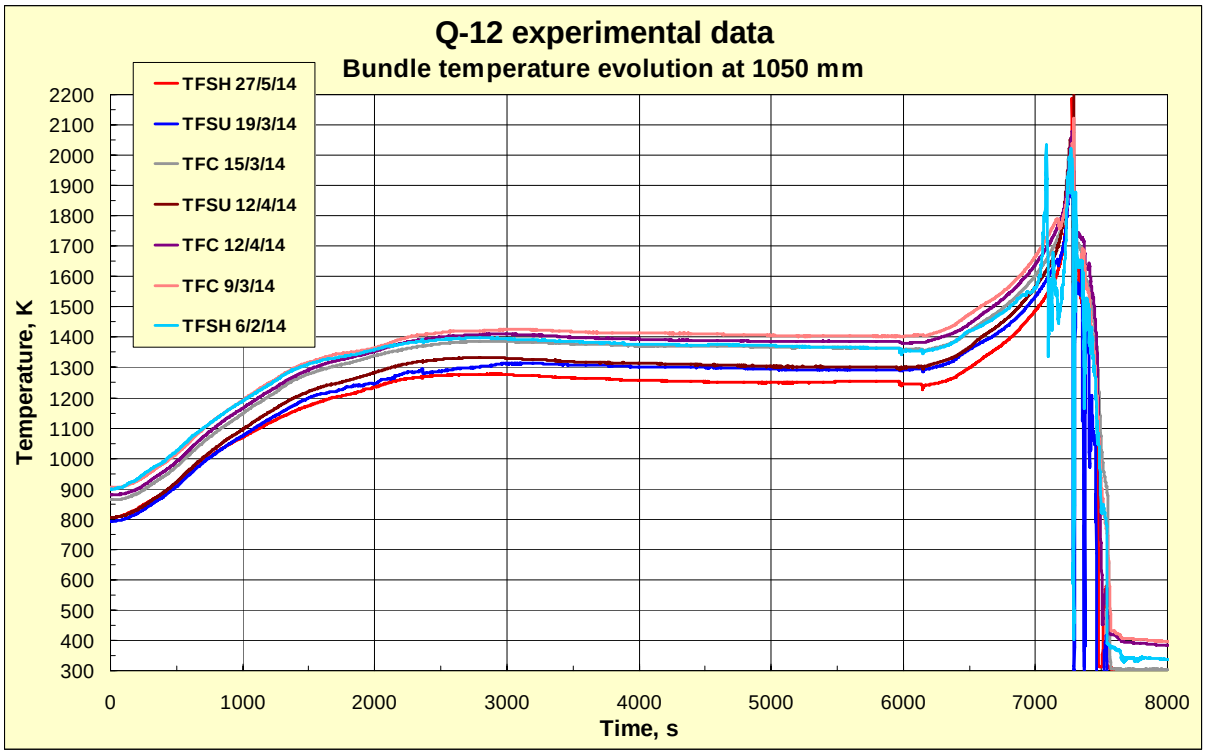

Fig 49. Bundle temperature evolution at the elevation 1050 mm measured by TFSH/TFC/TFSU thermocouples

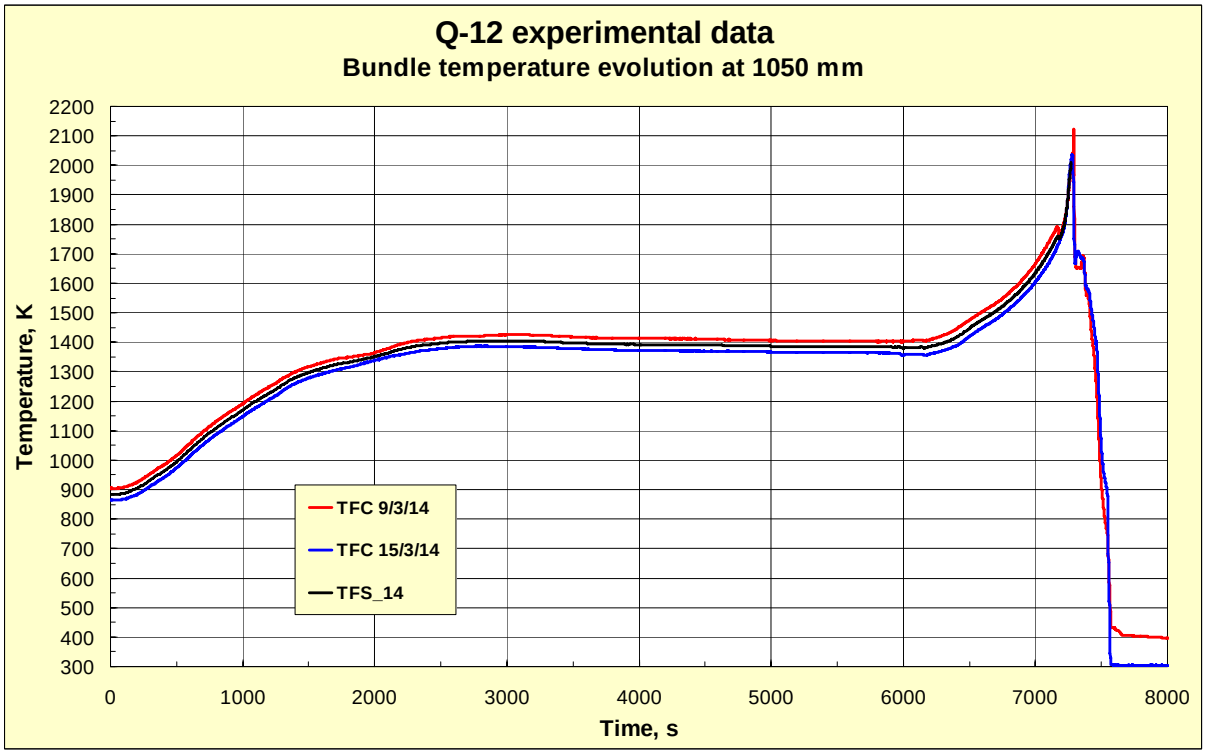

Fig 50. Bundle temperature evolution at the elevation 1050 mm measured by TFC 9/3/14 (red line), TFC 15/3/14 (blue line) and averaged temperature used in the calculations (black line)

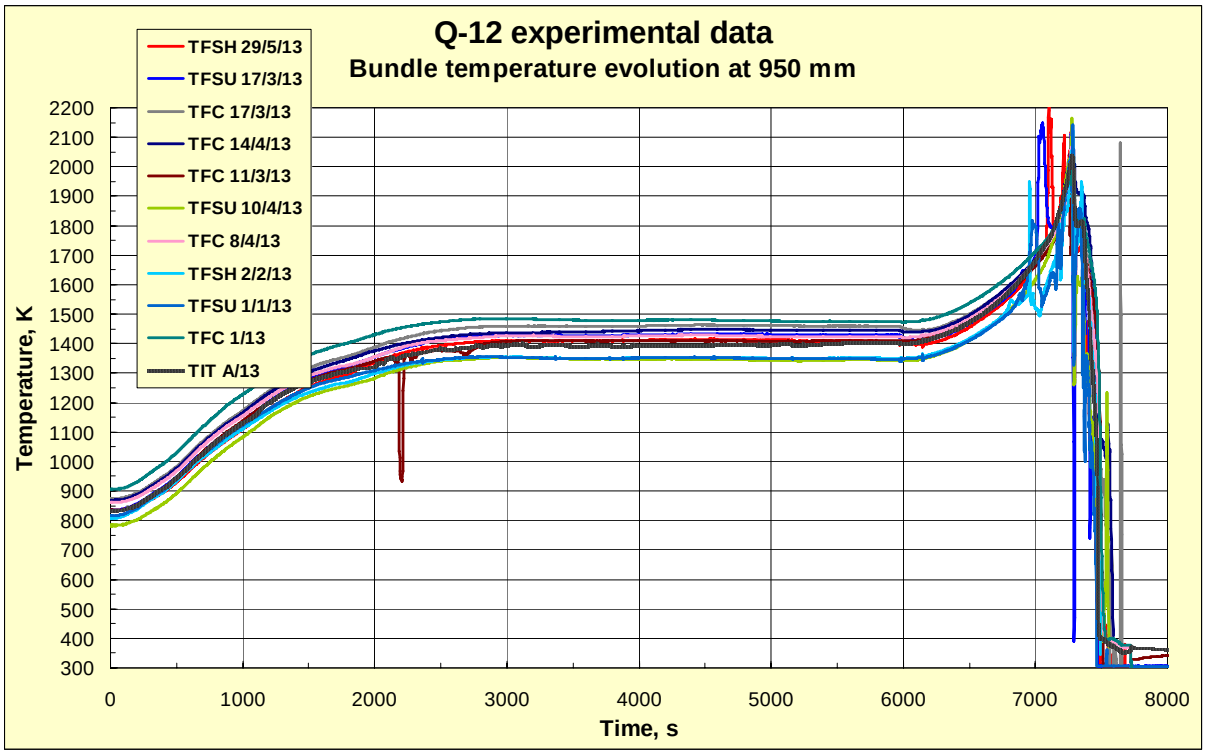

Fig 51. Bundle temperature evolution at the elevation 950 mm measured by TFSH/TFC/TFSU/TIT thermocouples

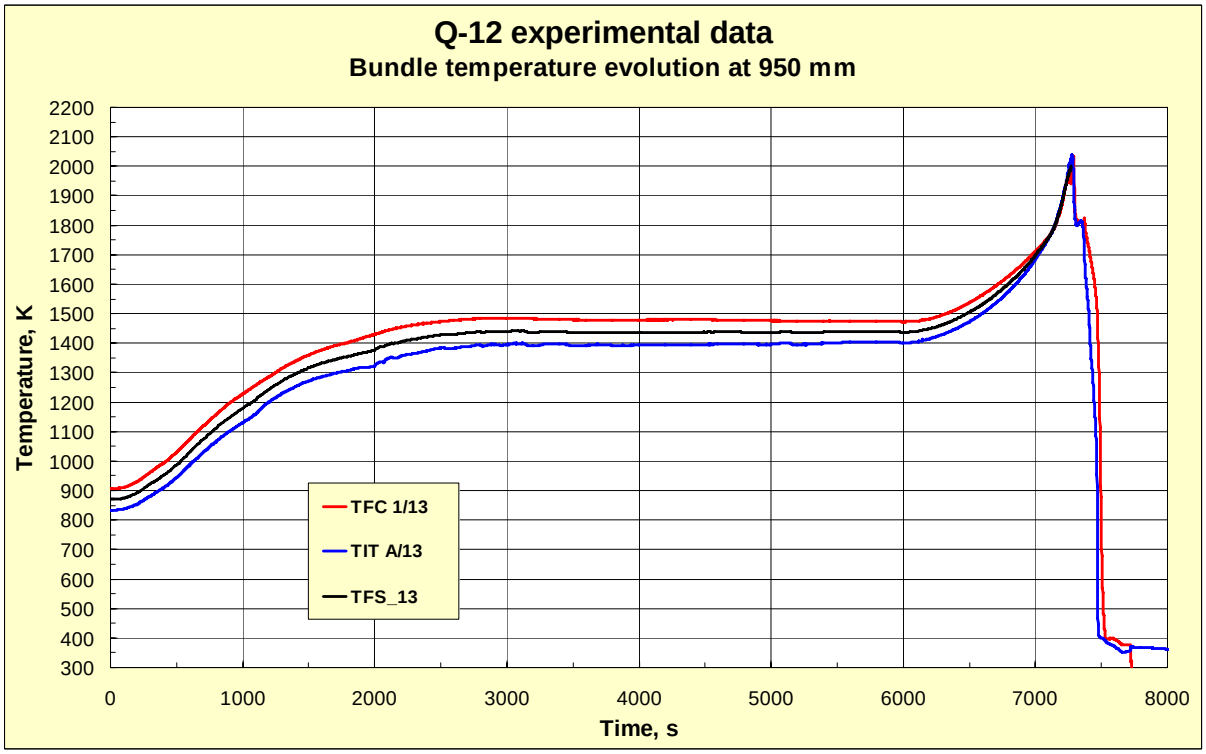

Fig 52. Bundle temperature evolution at the elevation 950 mm measured by TFC 1/13 (red line), TIT A/13 (blue line) and averaged temperature used in the calculations (black line)

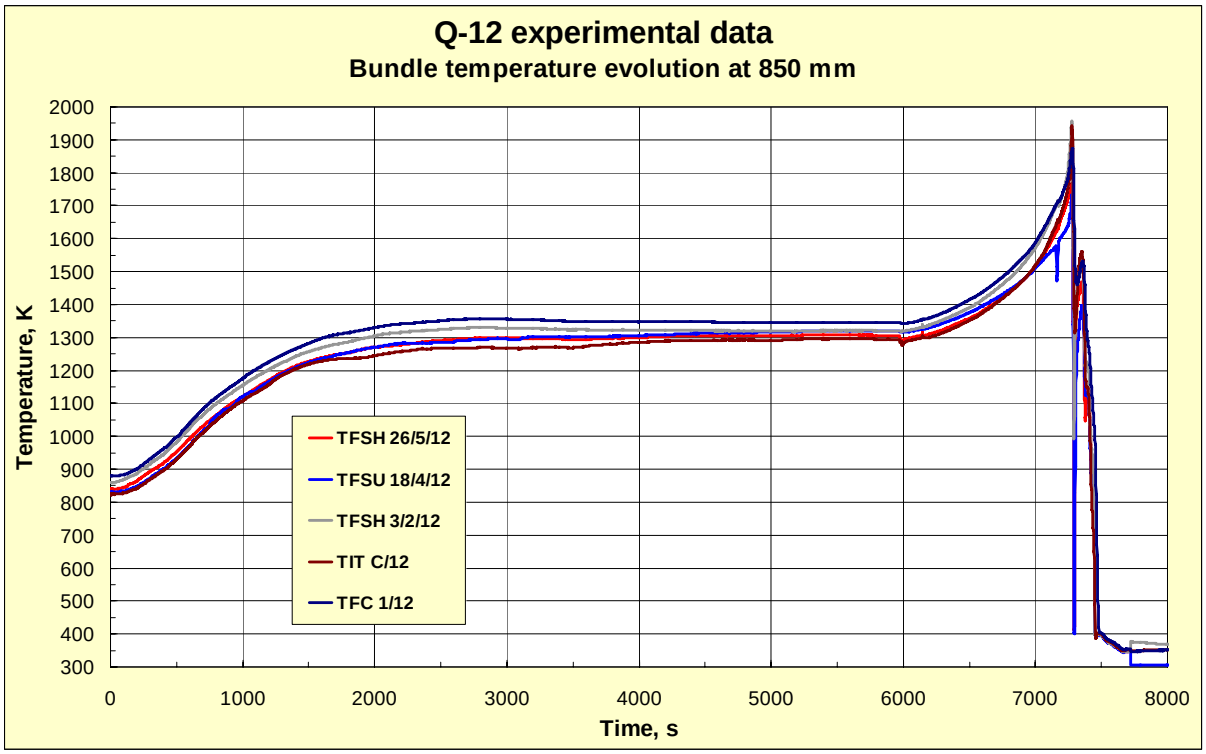

Fig 53. Bundle temperature evolution at the elevation 850 mm measured by TFSH/TFC/TFSU/TIT thermocouples

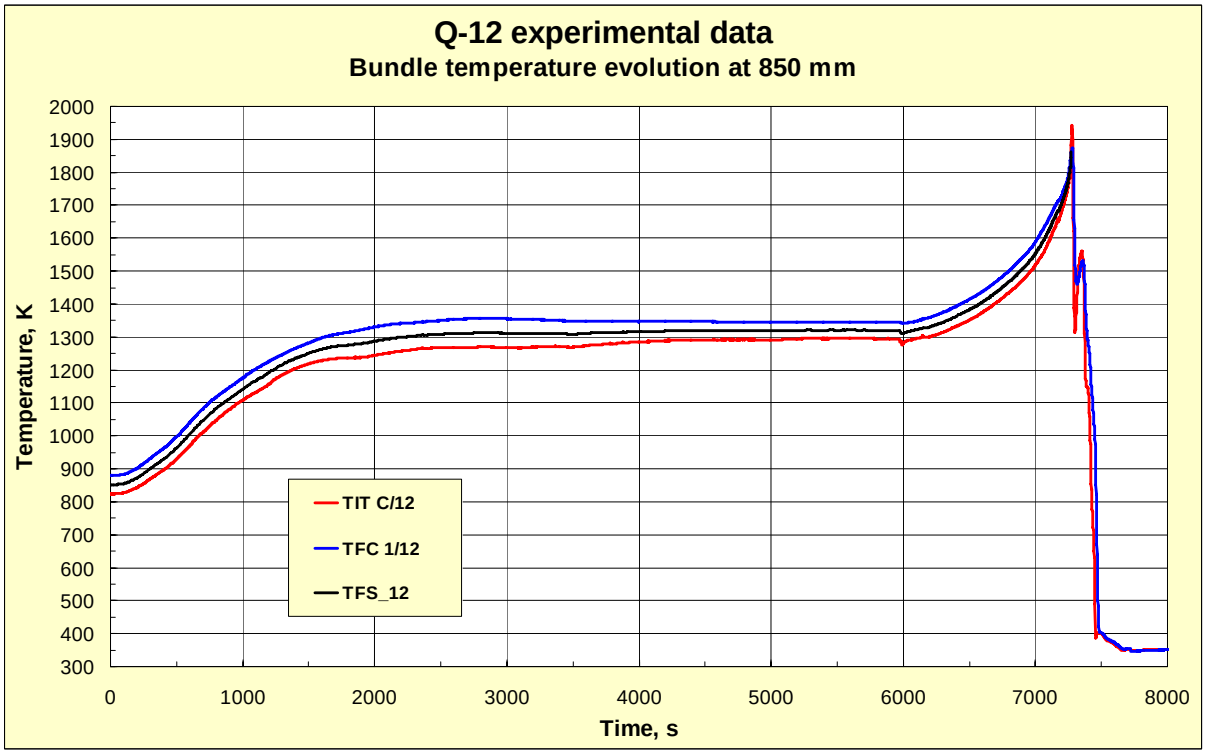

Fig 54. Bundle temperature evolution at the elevation 850 mm measured by TIT C/12 (red line), TFC 1/12 (blue line) and averaged temperature used in the calculations (black line)

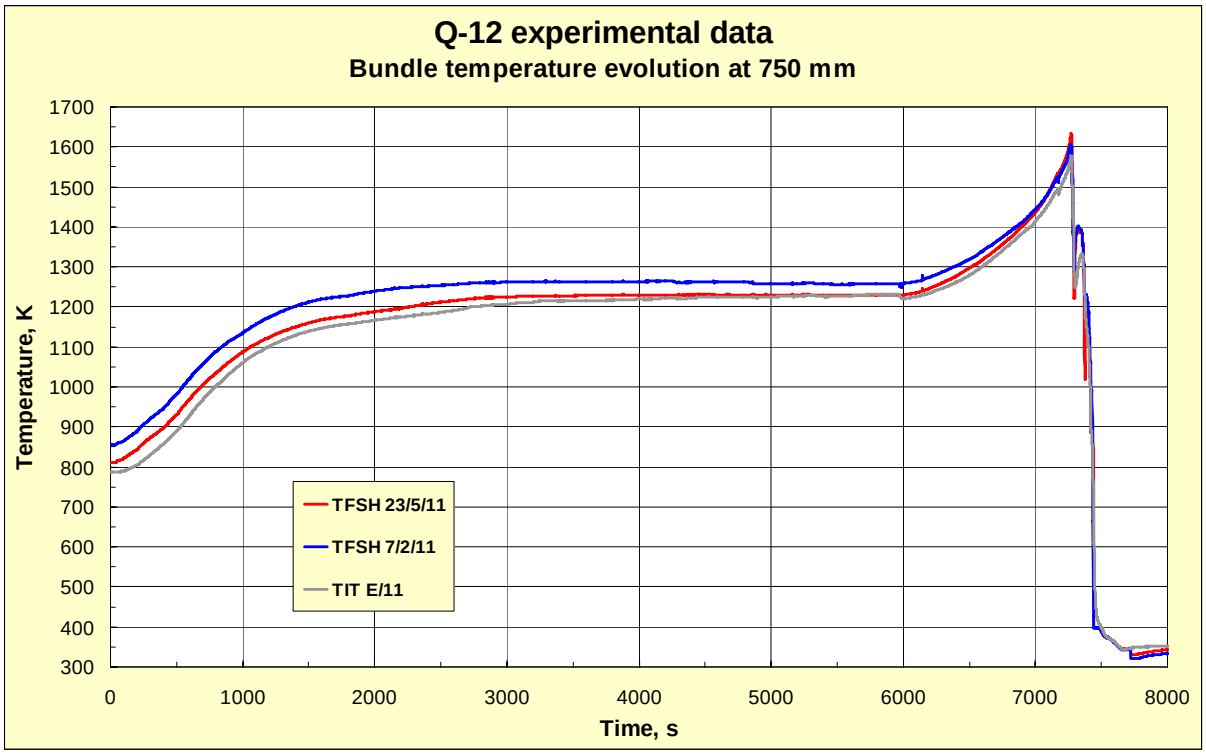

Fig 55. Bundle temperature evolution at the elevation 750 mm measured by TFSH/TIT thermocouples

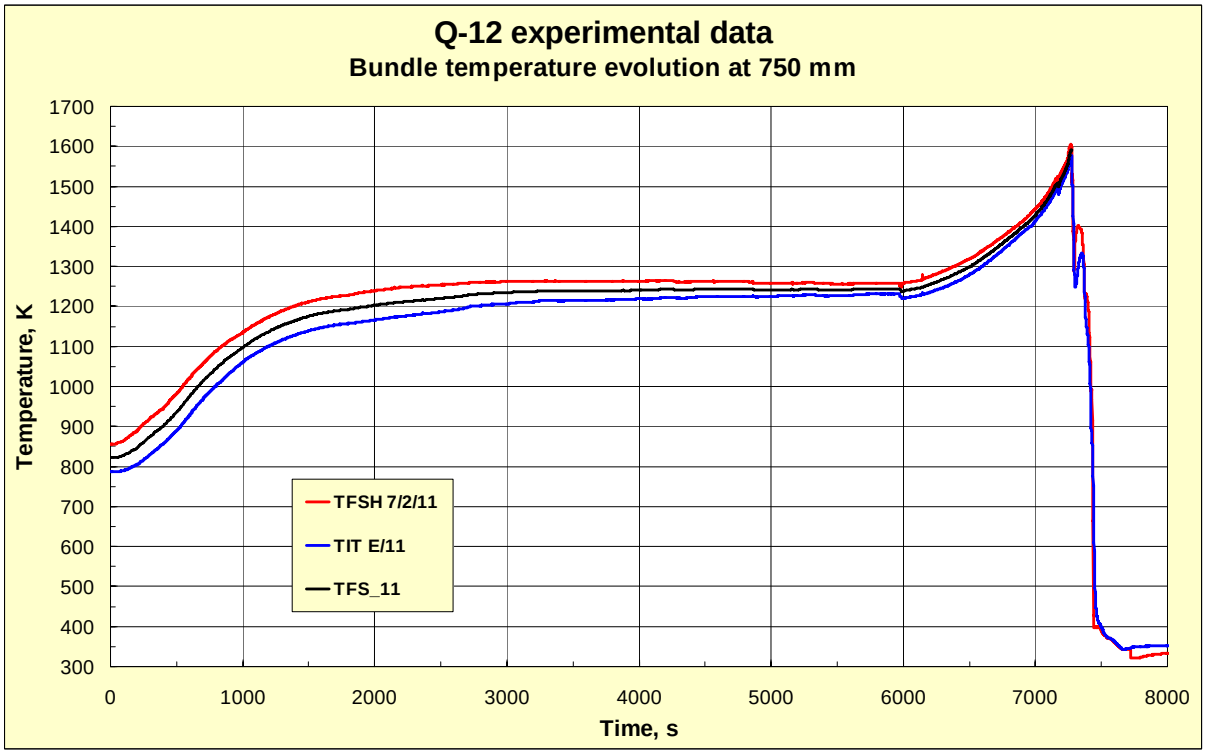

Fig 56. Bundle temperature evolution at the elevation 750 mm measured by TFSH 7/2/11 (red line), TIT E/11 (blue line) and averaged temperature used in the calculations (black line)

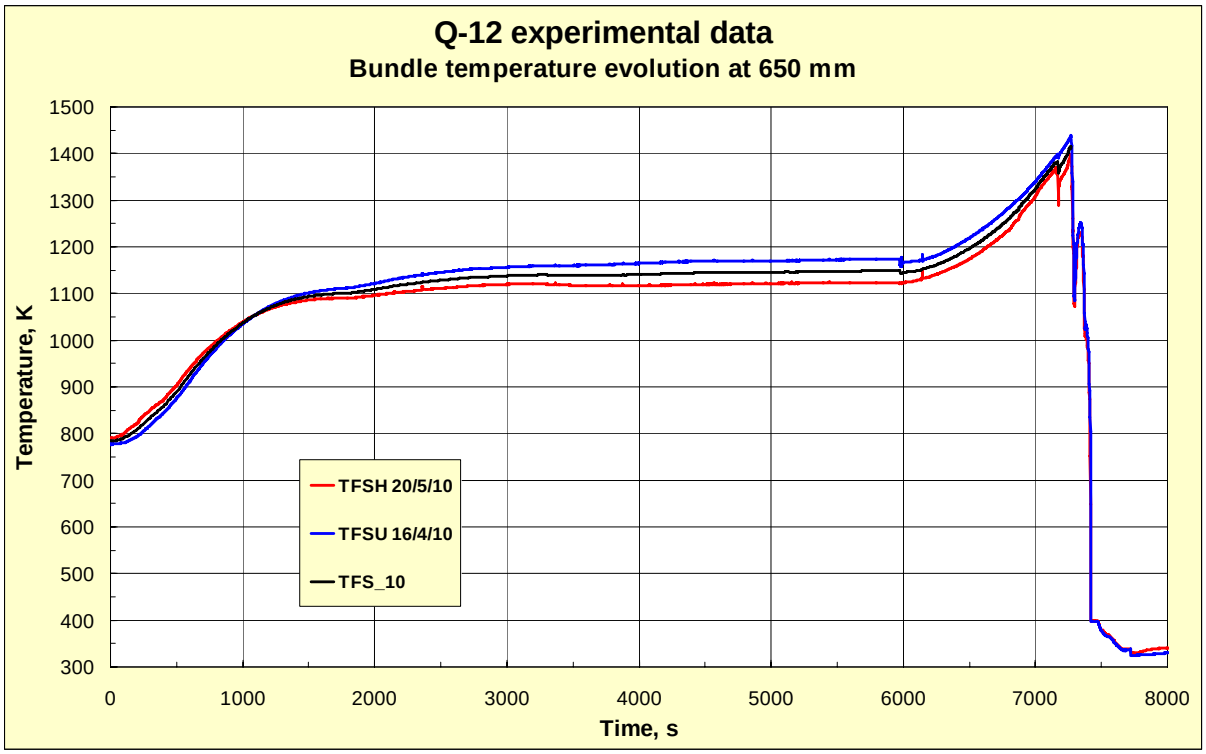

Fig 57. Bundle temperature evolution at the elevation 650 mm measured by TFSH 20/5/10 (red line), TFSU 16/4/10 (blue line) and averaged temperature used in the calculations (black line)

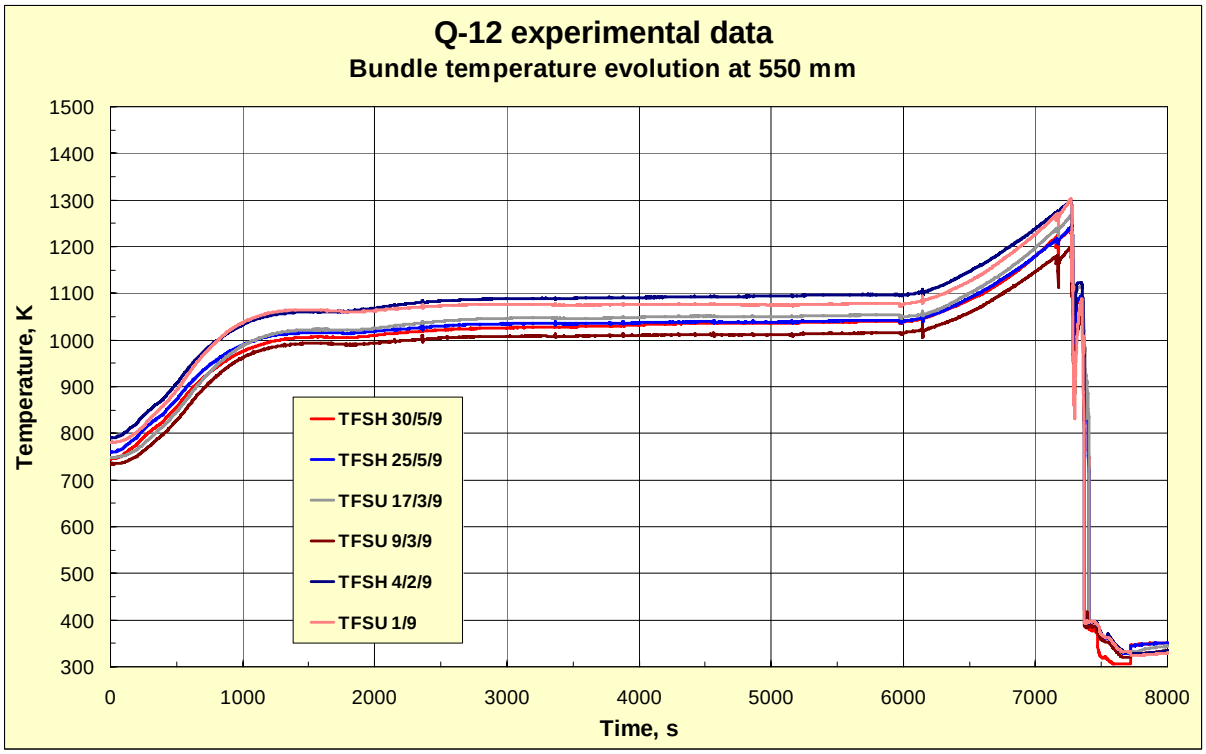

Fig 58. Bundle temperature evolution at the elevation 550 mm measured by TFSH/TFSU thermocouples

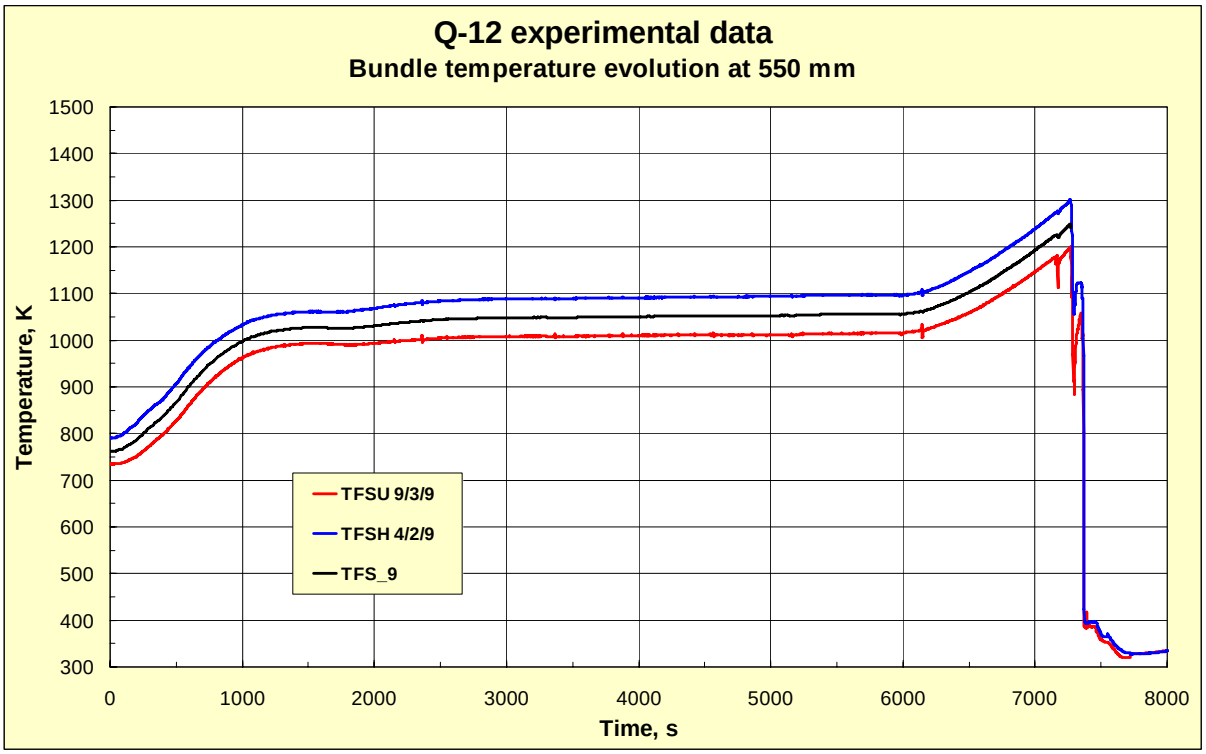

Fig 59. Bundle temperature evolution at the elevation 550 mm measured by TFSU 9/3/9 (red line), TFSH 4/2/9 (blue line) and averaged temperature used in the calculations (black line)

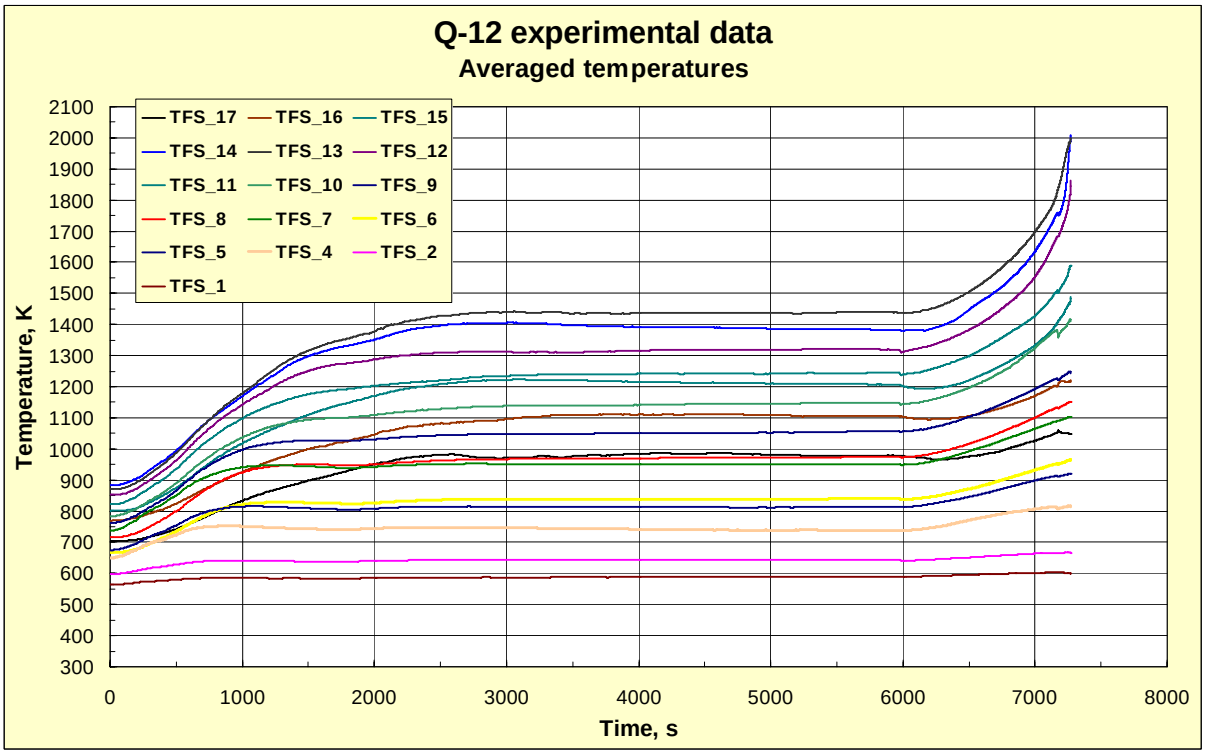

Fig 60. Averaged and smoothed curves representing temperature evolution of the QUENCH-12 bundle at the elevations from 1350 to -250 mm

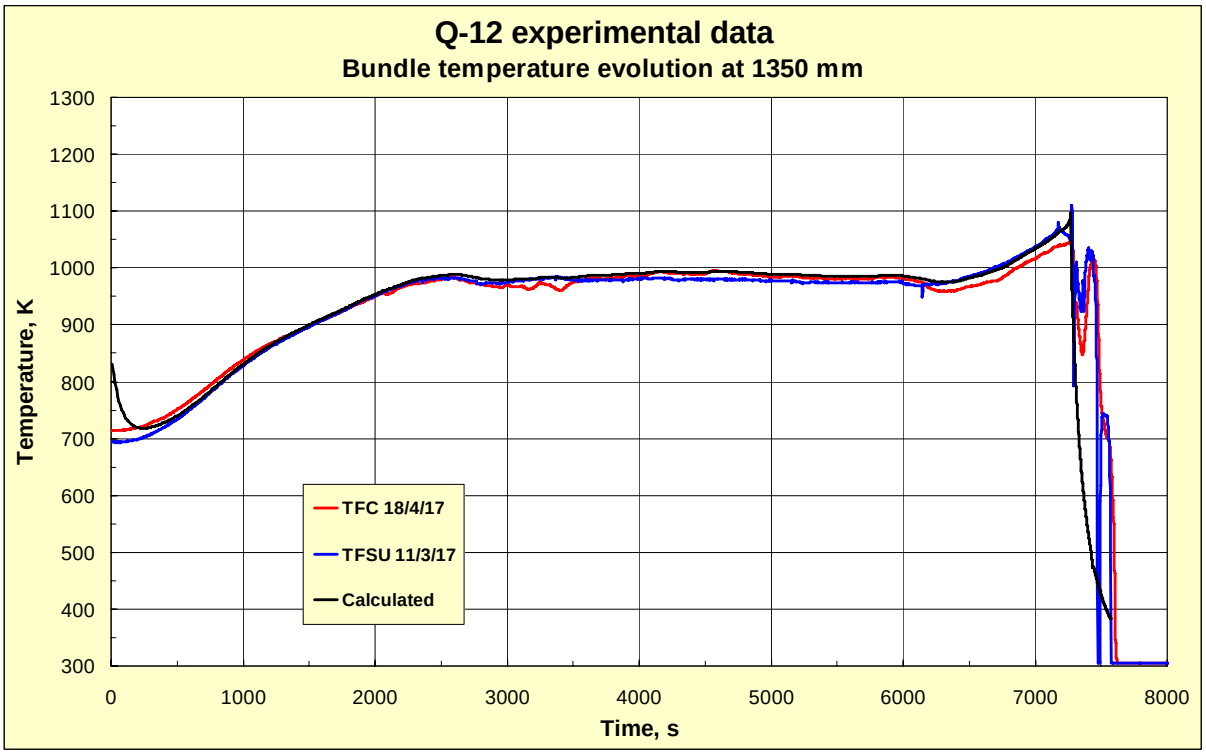

Fig 61. Bundle temperature evolution at the elevation 1350 mm measured by thermocouples TFC 18/4/17 (red line), TFSU 11/3/17 (blue line) and calculated temperature evolution of the central rod outer surface (black line)

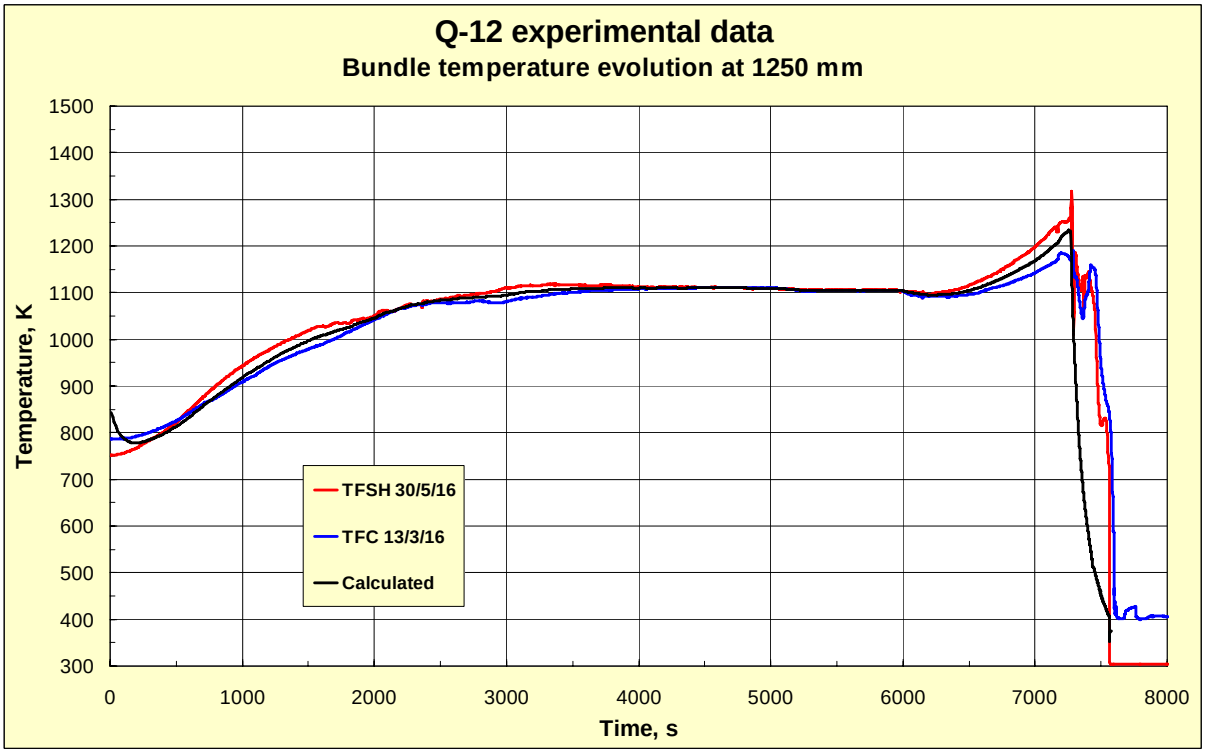

Fig 62. Bundle temperature evolution at the elevation 1250 mm measured by thermocouples TFSH 30/5/16 (red line), TFC 13/3/16 (blue line) and calculated temperature evolution of the central rod outer surface (black line)

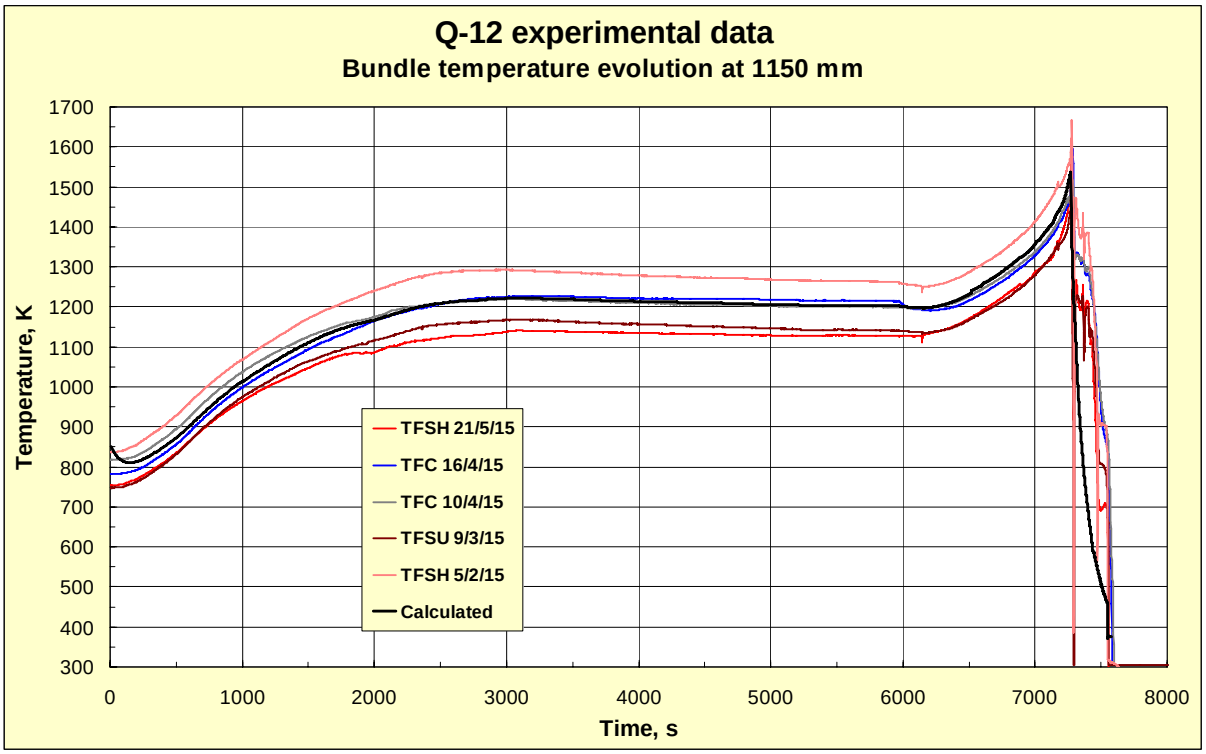

Fig 63. Bundle temperature evolution at the elevation 1150 mm measured by TFSH/TFC/TFSU thermocouples (colored lines) and calculated temperature evolution of the central rod outer surface (black line)

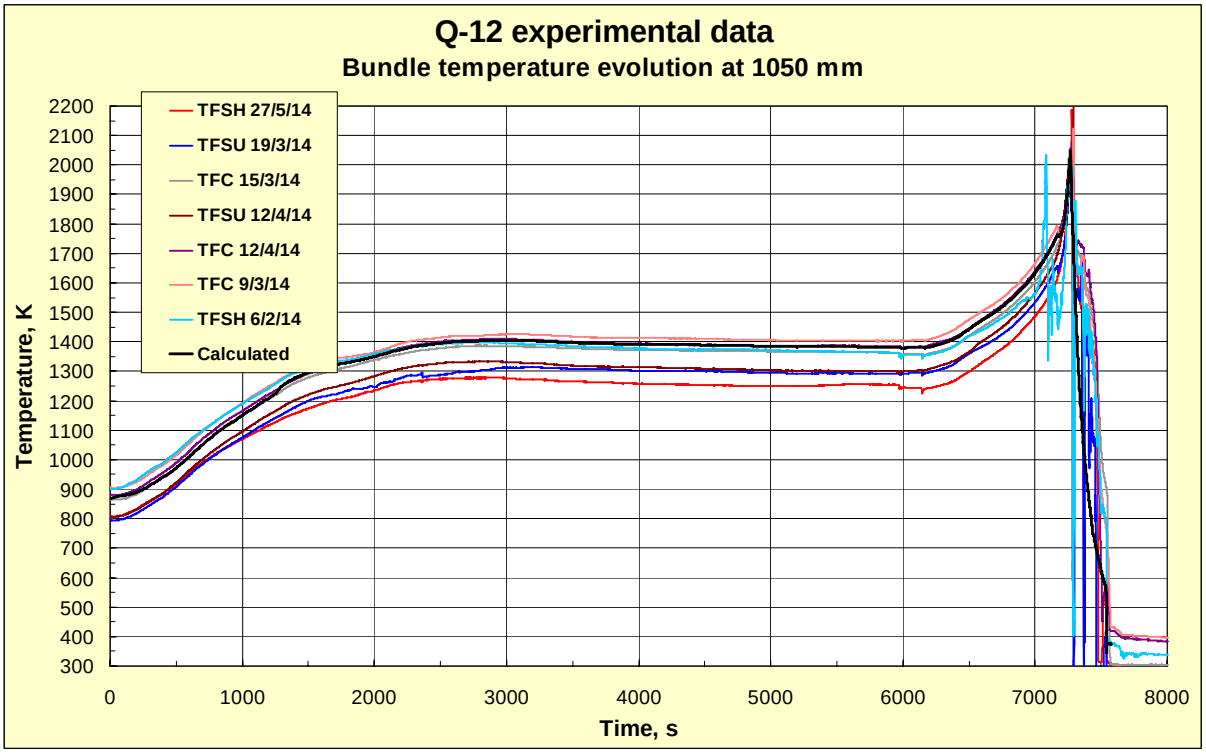

Fig 64. Bundle temperature evolution at the elevation 1050 mm measured by TFSH/TFC/TFSU thermocouples (colored lines) and calculated temperature evolution of the central rod outer surface (black line)

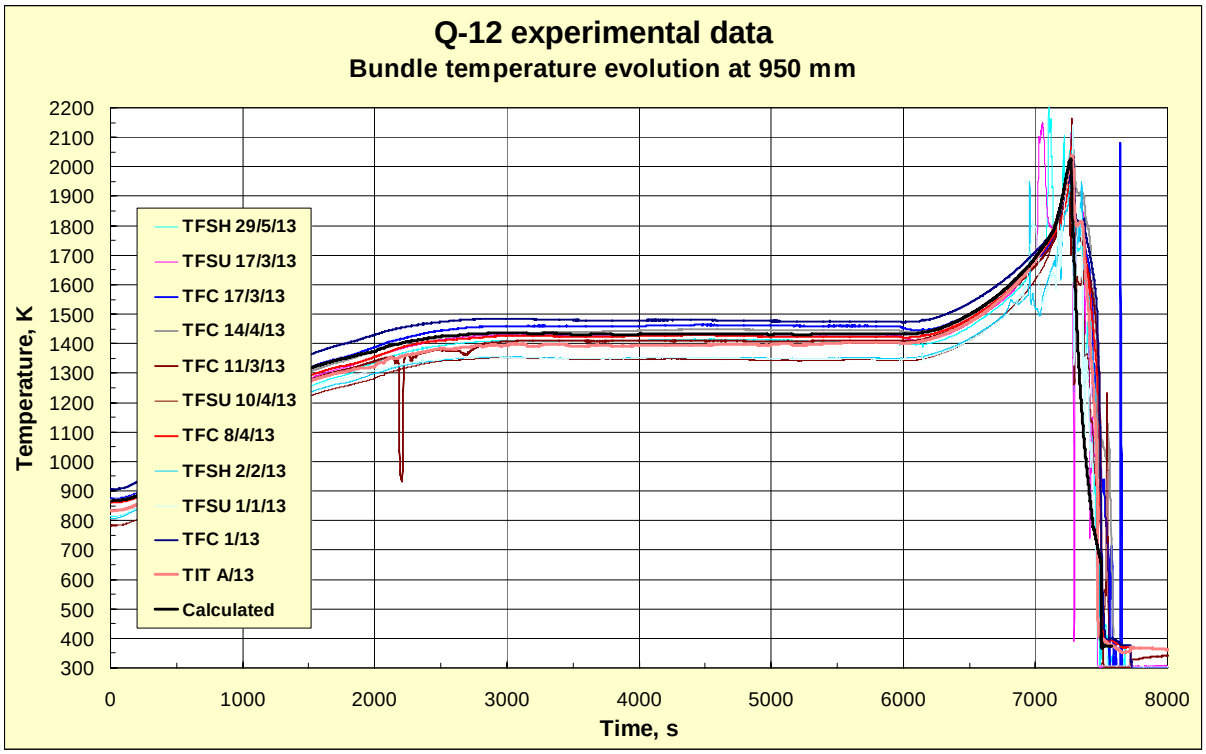

Fig 65. Bundle temperature evolution at the elevation 950 mm measured by TFSH/TFC/TFSU thermocouples (colored lines) and calculated temperature evolution of the central rod outer surface (black line)

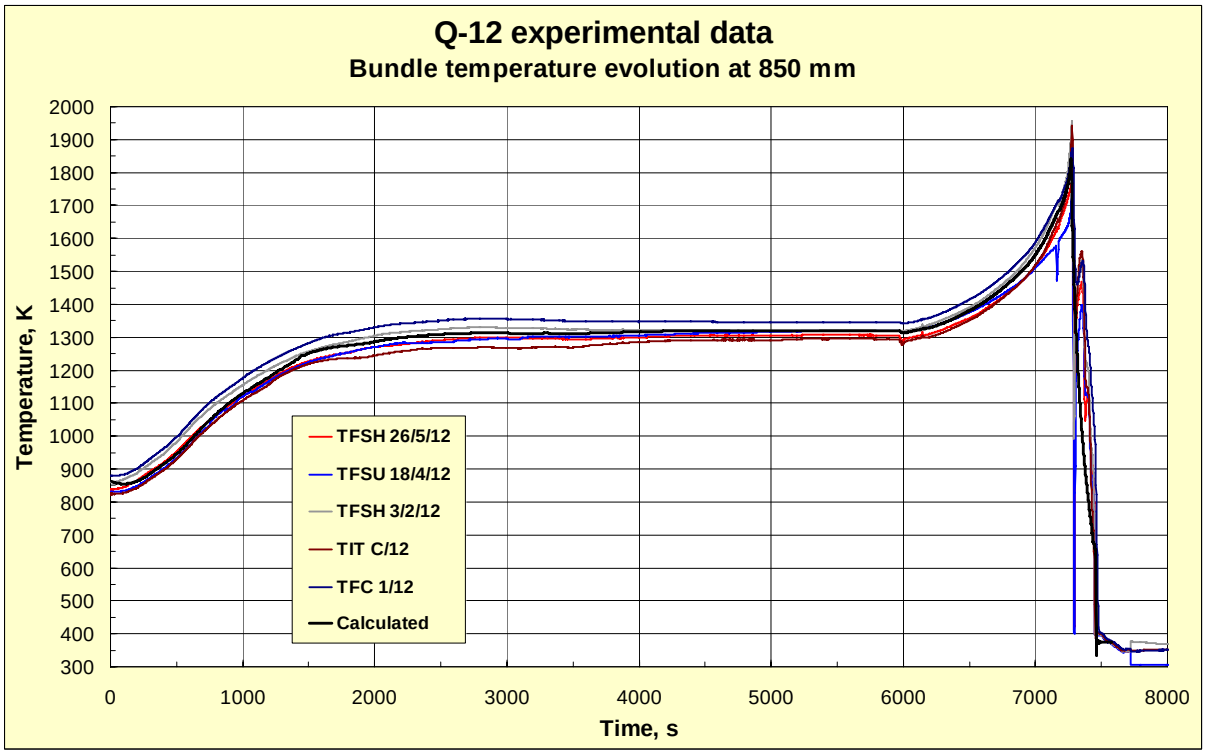

Fig 66. Bundle temperature evolution at the elevation 850 mm measured by TFSH/TFC/TFSU thermocouples (colored lines) and calculated temperature evolution of the central rod outer surface (black line)

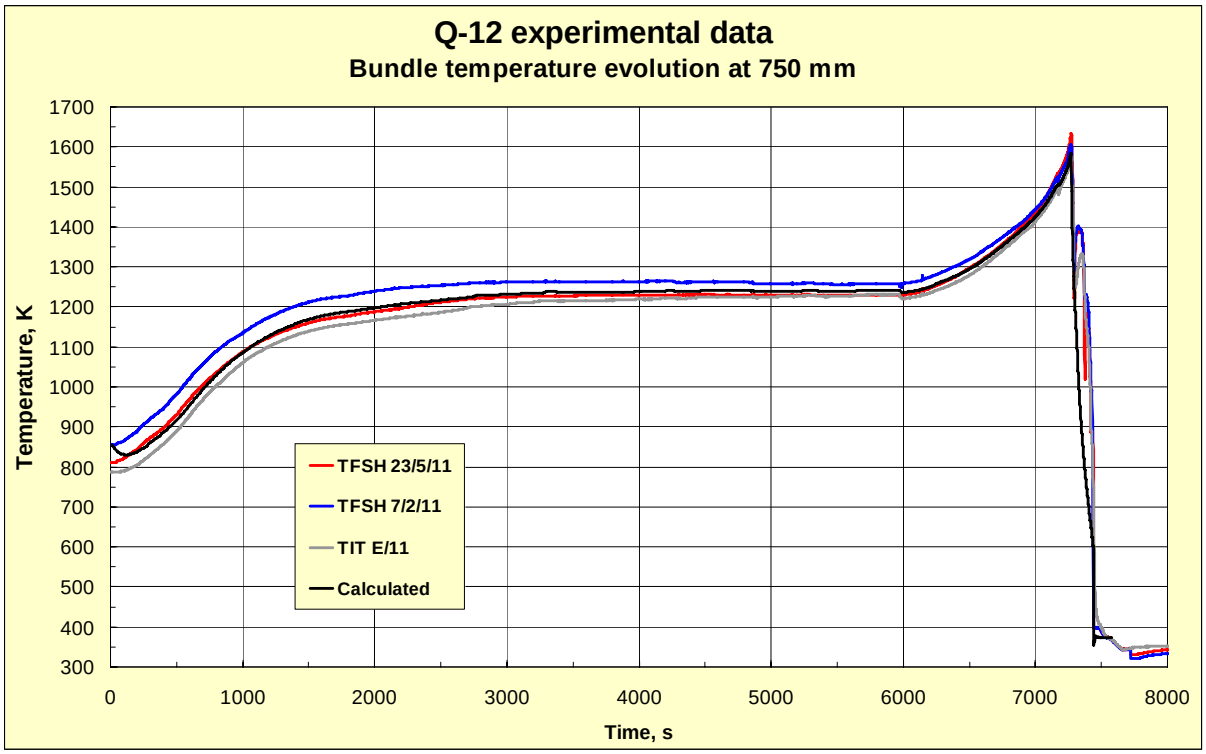

Fig 67. Bundle temperature evolution at the elevation 750 mm measured by thermocouples TFSH 23/5/11 (red line), TFSH 7/2/11 (blue line), TIT E/11 (grey line) and calculated temperature evolution of the central rod outer surface (black line)

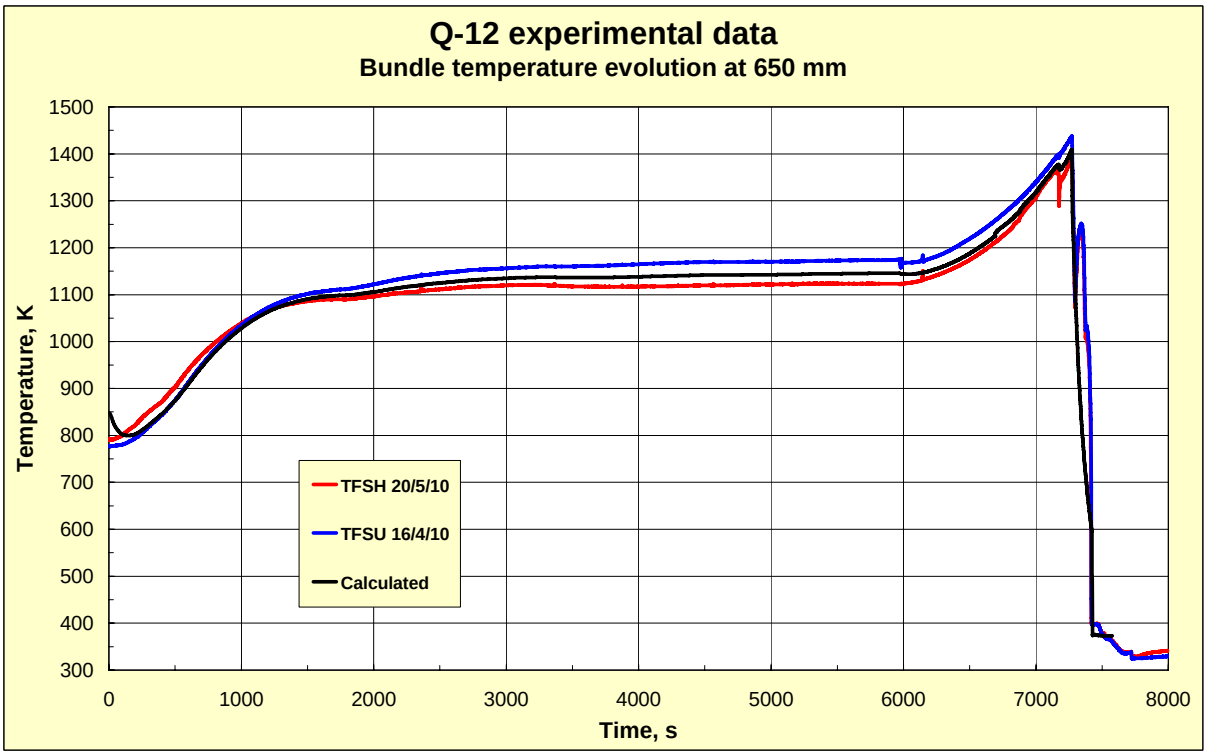

Fig 68. Bundle temperature evolution at the elevation 650 mm measured by thermocouples TFSH 20/5/10 (red line), TFSU 16/4/10 (blue line) and calculated temperature evolution of the central rod outer surface (black line)

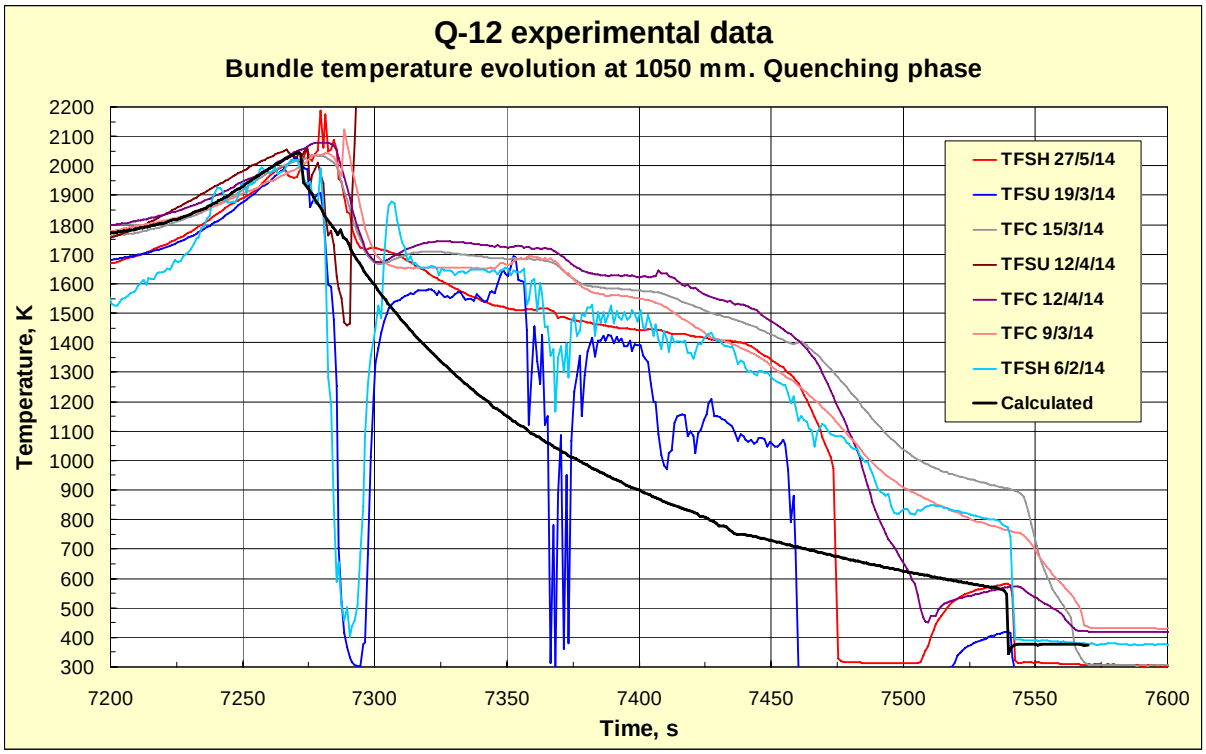

Fig 69. The experimentally measured temperatures at the elevation 1050 mm (colored lines) and calculated temperature evolution of the central rod outer surface (black line). Quenching phase (time period 7200 – 7600 s)

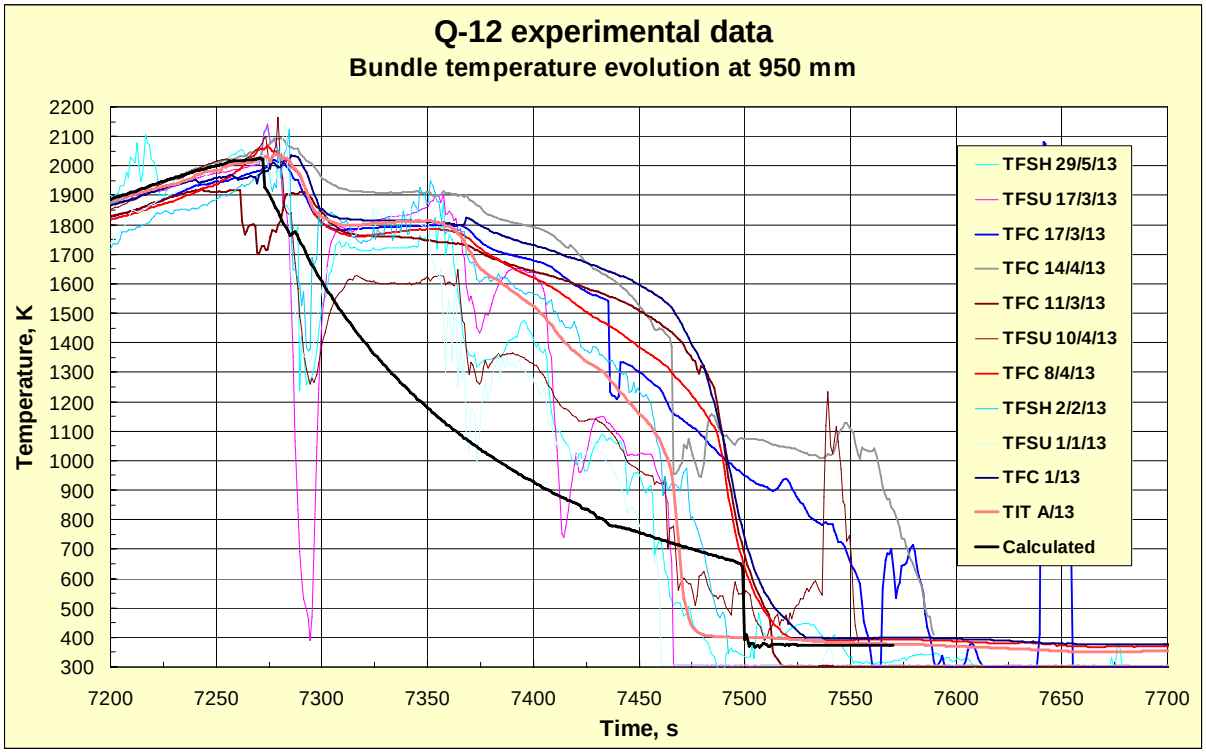

Fig 70. The experimentally measured temperatures at the elevation 950 mm (colored lines) and calculated temperature evolution of the central rod outer surface (black line). Quenching phase (time period 7200 – 7700 s)

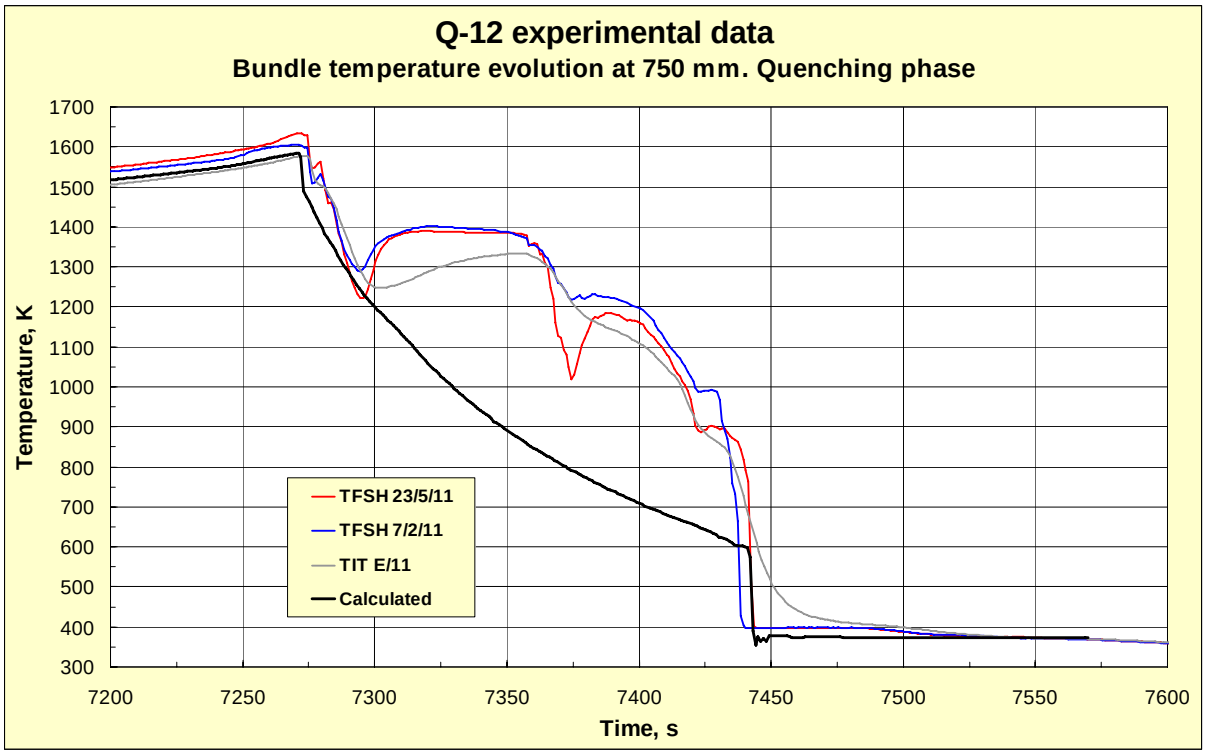

Fig 71. The experimentally measured temperatures at the elevation 750 mm (colored lines) and calculated temperature evolution of the central rod outer surface (black line). Quenching phase (time period 7200 – 7600 s)

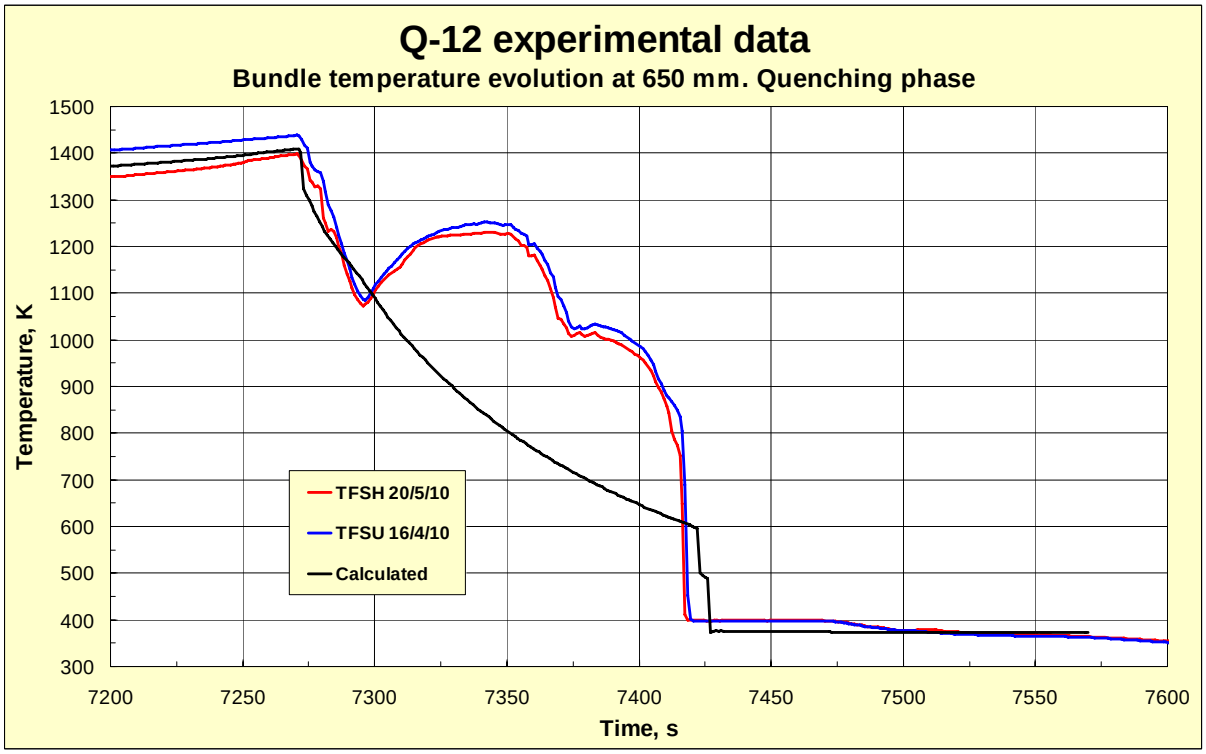

Fig 72. The experimentally measured temperatures at the elevation 650 mm (colored lines) and calculated temperature evolution of the central rod outer surface (black line). Quenching phase (time period 7200 – 7600 s)

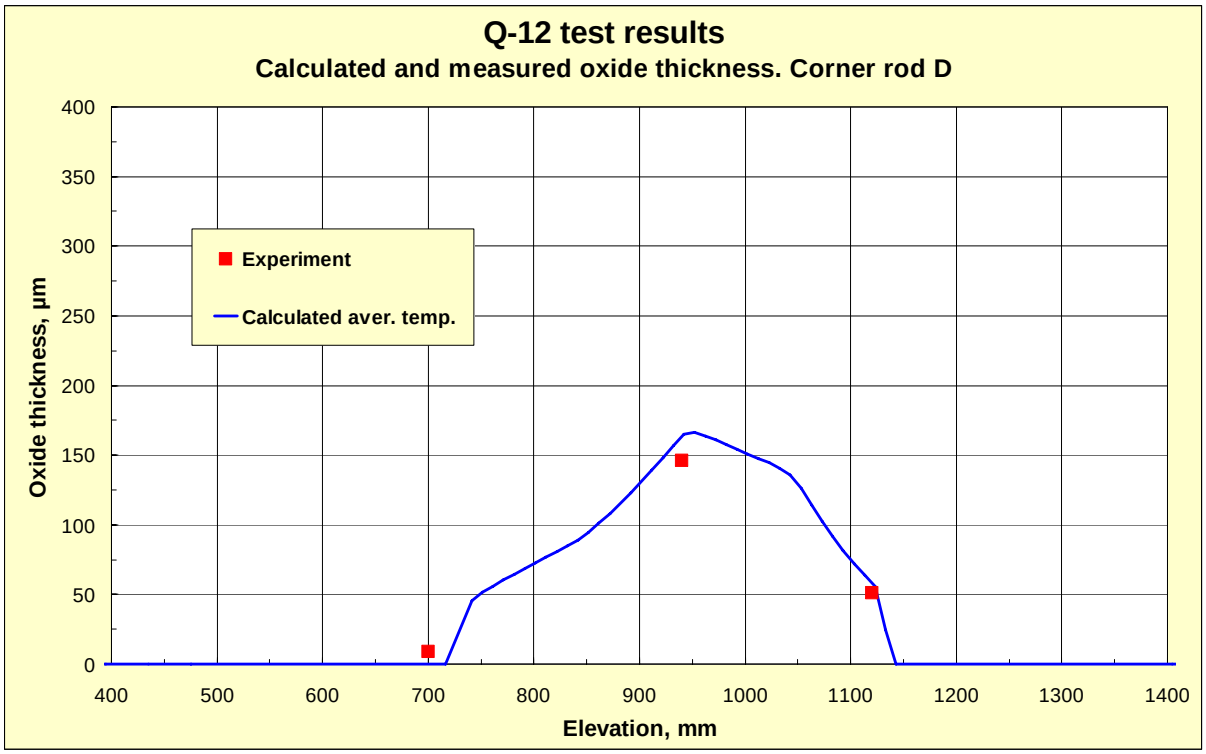

Fig 73. Oxide layer thickness axial profile of corner rod D (withdrawn from the test bundle at 5972 s) compared to the calculated one of the central rod for the same time

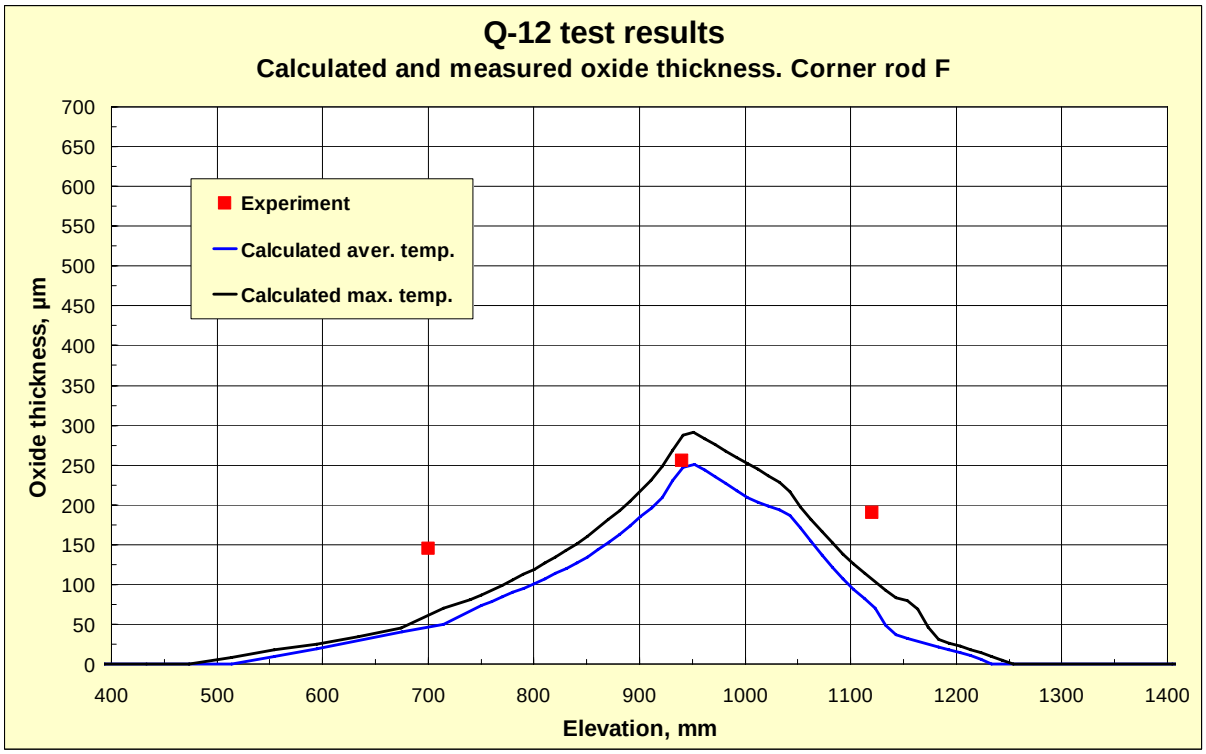

Fig 74. Oxide layer thickness axial profile of corner rod F (withdrawn from the test bundle at 7158 s) compared to the calculated one of the central rod for the same time. Calculation was performed using average temperatures (blue line) and highest temperatures (black line) at each elevation as the basis for the effective channel wall temperature

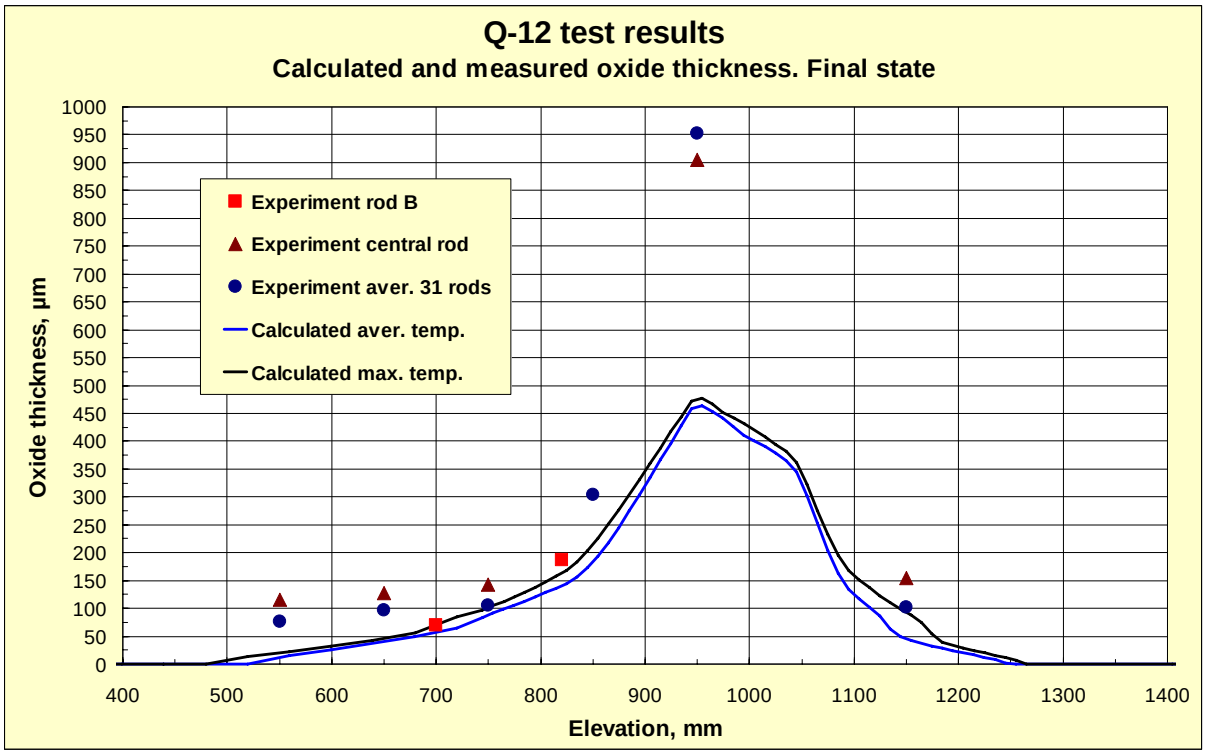

Fig 75. Measured oxide layer thickness axial profiles of corner rod B, central rod, and averaged value for 31 rods at the end of the test compared to the calculated oxide layer profile of the central rod (final state). Calculation was performed using average temperatures (blue line) and highest temperatures (black line) at each elevation as the basis for the effective channel wall temperature

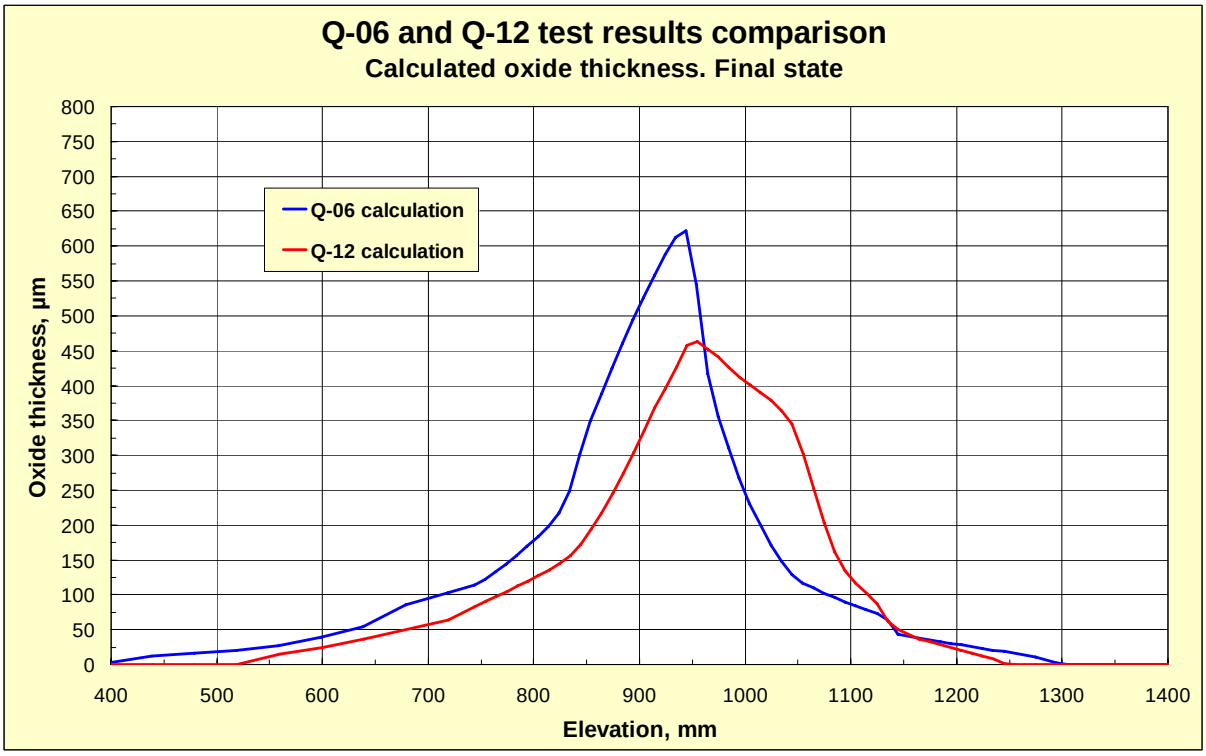

Fig 76. Comparison of the calculated oxide layer thickness axial profiles in Q-06 and Q-12 tests simulation

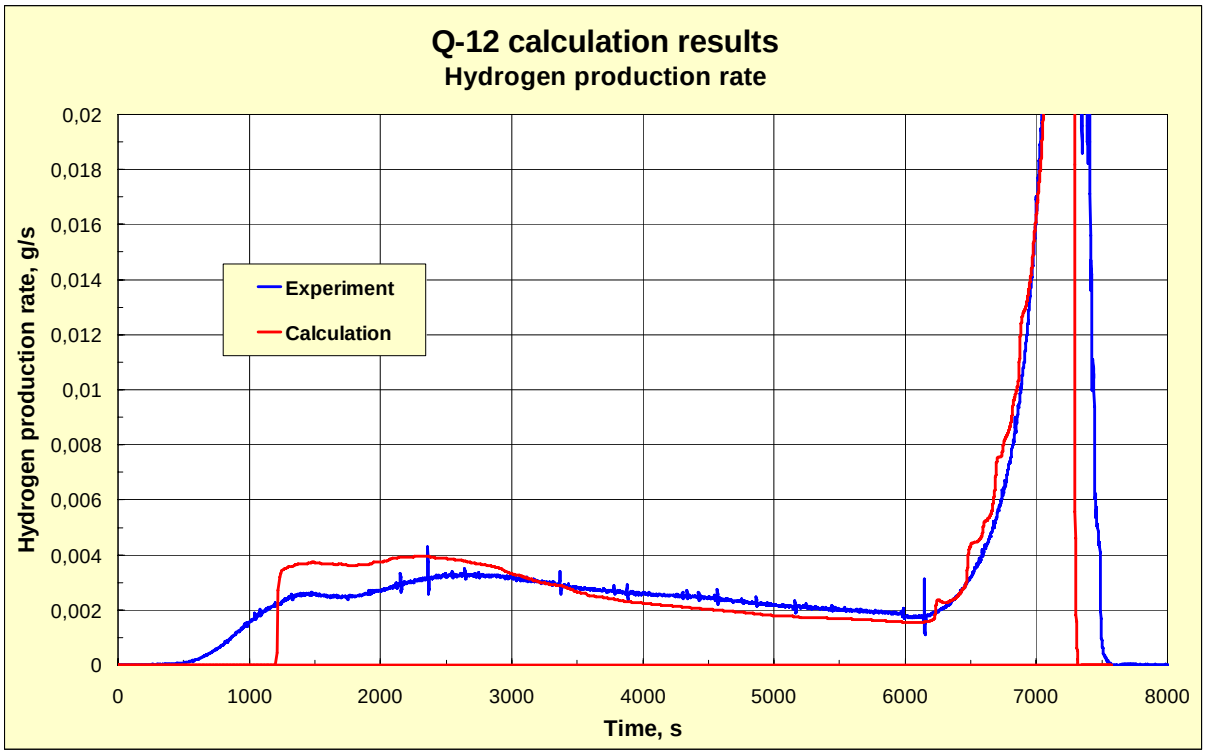

Fig 77. Experimentally measured and calculated hydrogen production rate

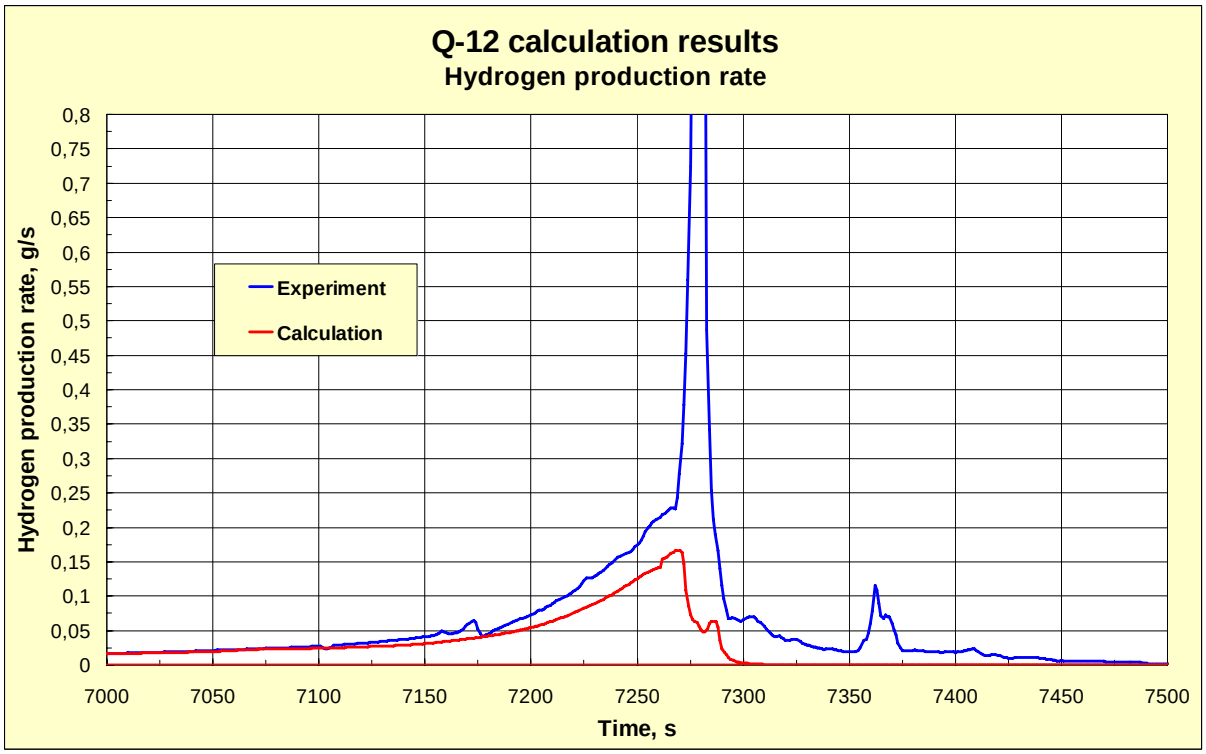

Fig 78. Experimentally measured and calculated hydrogen production rate. Transient and quenching phases of the test

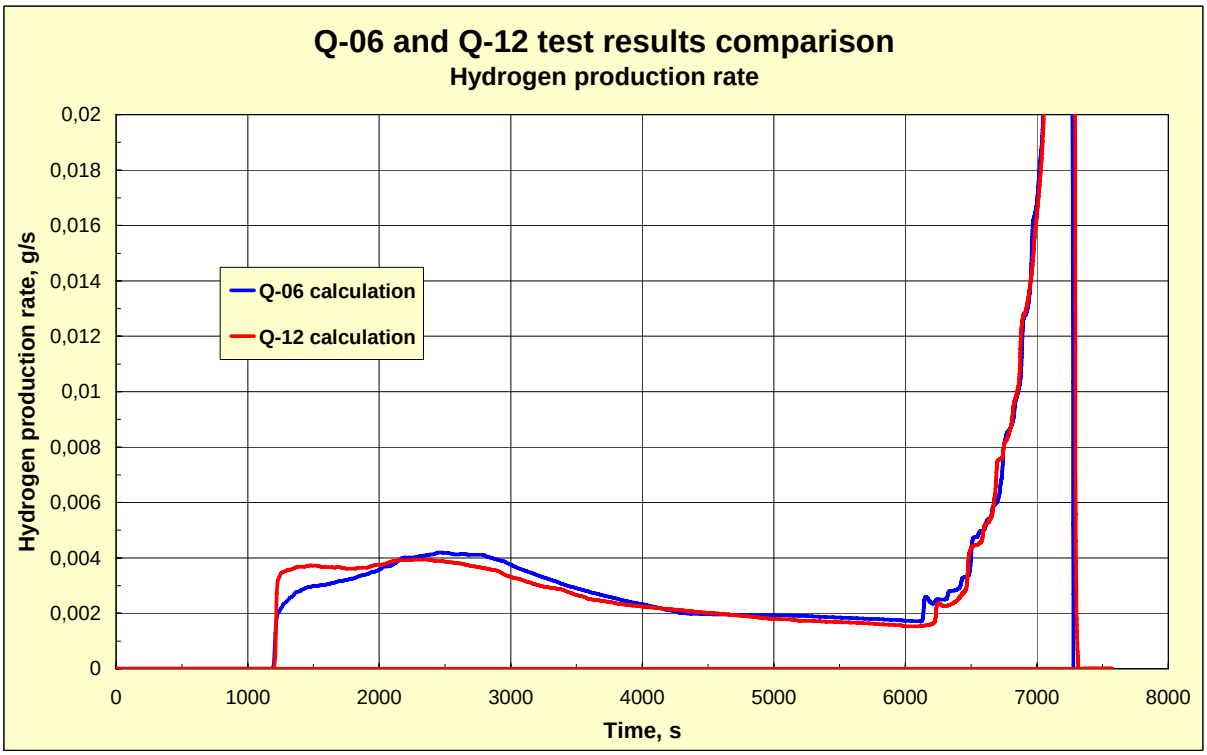

Fig 79. Comparison of the calculated hydrogen production rates in Q-06 and Q-12 tests simulation

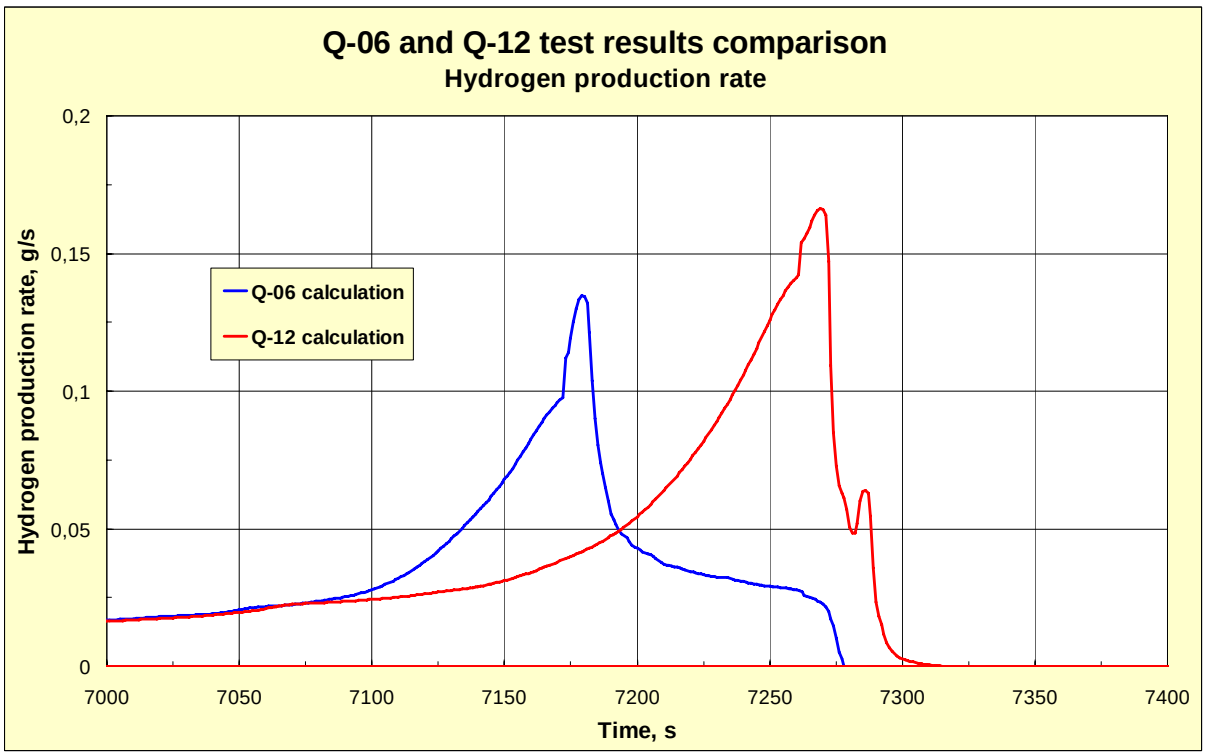

Fig 80. Comparison of the calculated hydrogen production rates in Q-06 and Q-12 tests simulation. Transient and quenching phases of the test